Signal Processing to Overcome Random Vibration Interference in an Oil Debris Monitor (ODM) Sensor

by

Weihong Chen

Supervised by Dr. Martin Bouchard

Co-Supervised by Dr. Ming Liang

A thesis presented to the University of Ottawa
in fulfillment of the thesis requirement for the degree of
Master of Applied Science in Electrical and Computer Engineering

AUTHOR'S DECLARATION

I hereby declare that I am the sole author of this thesis. This is a true copy of the thesis, including any required final revisions, as accepted by my examiners. I understand that my thesis may be made electronically available to the public.

Abstract

Online Oil Debris Monitors (ODM) provide a direct, effective and reliable approach to machinery condition monitoring. ODM can be used to monitor the condition of complex machines, such as airplane engines, electric generators, wind turbines, or other machines with oil circulation systems. The principle of the sensor is to detect the quantity and the size of metal particles in the flowing oil. The current available ODM sensors suffer from sensitivity to vibrations, as their electromagnetic response is largely affected by interfering vibrations. This thesis presents a novel structure and algorithms to separate and eliminate the vibration interference. In the new structure, a dual channel system is designed as opposed to previous single channel systems. Three signal processing algorithms have been developed and tested using experimental data from a prototype. They have shown to be effective, as detailed in the thesis.

Acknowledgements

First and foremost I offer my sincerest gratitude to my supervisor, Dr. Martin Bouchard, and co-supervisor, Dr. Ming Liang, who have supported me throughout my thesis with their patience and knowledge. Dr. Bouchard has offered much advice and insight throughout my work on the ODM system, especially on the algorithm research. Dr. Liang has provided me with complete lab instruments and materials, allowing me the room to work in my own way. In the thesis edition, both of them have patiently and carefully revised my thesis. Without them, this thesis would not have been completed.

At the early stages of laboratory experimentation, I was aided by Dr. Chuan Li, a postdoctoral fellow from ChongQing Technology and Business University, Sichuan, China. He gave me much experience on coil winding in the creation of the prototype.

Dr. Yi Zhang and Dr. Shumin Hou, postdoctoral fellows in the Mechanical Engineering department at the University of Ottawa, have also helped me with the assembly of a prototype in the final demonstration. They have given me some useful improvements on the prototype structure.

Finally, I thank my parents for supporting me throughout all my studies at the University of Ottawa.

Table of Contents

AUTHOR'S DECLARATION ii
Abstract iii
Acknowledgements iv
Table of Contents v
List of Figures vii
List of Symbols, Abbreviations and Nomenclature x
Chapter 1 Introduction 11
1.1 Oil Condition Monitors 11
1.2 GasTop Electromagnetic Oil Debris Monitor 14
Chapter 2 Design of a prototype sensor 19
2.1 Introduction to the Prototype 19
2.2 Common Interference 20
2.3 The Physical Nature of the Proposed Sensors 21
2.4 Solenoid Design 26
2.5 Electronic Design 29
2.5.1 Field Coil Driver 30
2.5.2 Pre-Amplifier 31
2.5.3 Demodulator 34
2.5.4 Analog Filter 37
2.5.5 Post-Amplifiers 46
2.6 Conclusion 47
Chapter 3 The Angle of Arrival Algorithm 48
3.1 Introduction 48
3.2 Signals from the Prototype 48
3.3 Basic Theory of AOA 51
3.3.1 The Model of AOA 51
3.3.2 Correlation Matrix 53
3.3.3 Power Scanning 54
3.4 Algorithm Implementation 55
3.5 Experimental Result Analysis 56

3.6 Conclusion 65
Chapter 4 TDOA Algorithm 66
4.1 Introduction 66
4.2 Cross Correlation 66
4.3 Uni-directional TDOA Measurement. 68
4.3.1 Snapshot Window 68
4.3.2 Cross Correlation and Convolution 69
4.3.3 Two Blocks Cross-Correlation 70
4.4 Bi-directional Cross Correlation 73
4.5 Experimental Results 75
4.5.1 Particle Signal and Background Noise 75
4.5.2 Particle Signal and Vibration Interference 81
4.6 Conclusion 83
Chapter 5 Phase Angle Selective Beamforming and AOA Filtering 84
5.1 Introduction 84
5.2 Single Frequency Beamforming System 84
5.2.1 Uniform Linear Array (ULA) 84
5.2.2 Steering the Beam Pattern. 87
5.2.3 Side Lobe Level 89
5.2.4 Base Beamforming 91
5.2.5 Null Steering and LMS Pattern 92
5.3 Broadband and Narrowband Signals 94
5.4 Virtual Sensor Array 95
5.5 Experimental Results 96
5.6 AOA Filtering 103
5.7 Comparison of the Two Methods 104
5.8 Conclusion 108
Chapter 6 Conclusion 109
6.1 Summary 109
6.2 Future Work 111
Bibliography 112
Appendix A Matlab Code (for reference) 117

List of Figures

Figure 1.2-1 Oil Debris Monitor Internal Structure (1) 15
Figure 1.2-1 Ferromagnetic Particle Signatures (2) 15
Figure 1.2-3 Particle signature immerged by vibration interference (3) 16
Figure 2.1-1 Two-channel ODM structure (4) 20
Figure 2.3-1 Magnetic flux *B* in a solenoid (5) 22
Figure 2.3-2 Magnetic flux *B* at the center of a circular coil (6) 23
Figure 2.3-3 The magnetic flux *B* distribution around the center of a circular coil (7) 24
Figure 2.3-4 The magnetic flux around the center of the two field coil system (8) 25
Figure 2.4-1 The magnetic flux density *B* vs coil counts *n* (9) 28
Figure 2.5-1 Block diagram of the electronic design (10) 30
Figure 2.5-2 Field Coil Driver Design (11) 31
Figure 2.5-3 Pre-Amplifier Design (12) 32
Figure 2.5-5 Rectifier/Demodulator Design (13) 37
Figure 2.5-6 Butterworth Frequency Response Design (14) 39
Figure 2.5-8 First-order Low-Pass Filter Design (15) 43
Figure 2.5-9 Second-order low-pass filter (16) 44
Figure 2.5-10 Two stage inverter amplifier (17) 46
Figure 2.6-1 ODM system prototype (18) 47
Figure 3.1-1 A ferrous particle (500μm) signal in static state (19) 49
Figure 3.1-2 A ferrous particle (500μm) signal in vibration state (20) 50
Figure 3.3-1 Structure of AOA processing (21) 51
Figure 3.3-1 The subsystem structure of AOA Processing (22) 54
Figure 3.5-1 The background noise in both channels (23) 57
Figure 3.5-2 Power, frequency and phase relationship (24) 58
Figure 3.5-3 Power, Frequency and Phase relationship of a particle signal (25) 60
Figure 3.5-4 Power, Frequency and Phase relationship of a vibration signal (26) 62
Figure 3.5-5 Power, frequency and phase relationship of mixed vibration and particle signals (27) 64

Figure 4.3-1 TDOA Window Selection (28) 70
Figure 4.4-1 Window structure for bi-directional algorithm (29)..... 74
Figure 4.5-1 Particle signal with background noise, time waveforms for channel 1 and channel 2 (30)..... 76
Figure 4.5-2 TDOA measurement with the uni-directional biased algorithm (linear scale and dB scale) (31)..... 76
Figure 4.5-4 Zoomed cross correlation function computed from the whole signal (linear scale and dB scale) (33)..... 77
Figure 4.5-5 Cross correlation with the unbiased uni-directional algorithm (linear scale and dB scale) (34)..... 78
Figure 4.5-6 Cross correlation with unbiased bi-directional algorithm (35) 79
Figure 4.5-7 Case with particle signal in Ch2 leading that of Ch1 (36) 80
Figure 4.5-8 Cross correlation result by the bi-directional unbiased algorithm (linear scale and dB scale). (37)..... 80
Figure 4.5-7 Vibration signal and particle signal mixed (38)..... 81
Figure 4.5-8 Cross correlation in uni-directional biased algorithm (linear scale and dB scale) (39) 82
Figure 5.2-1 Uniform linear array (ULA) Sensor (40) 85
Figure 5.2-2 N=6, a= 1/6 ULA Beam Pattern (41)..... 86
Figure 5.2-3 N=20, a= 1/20 ULA Beam Pattern (42)..... 86
Figure 5.2-4 N=20, a= 1/20 Delay and Sum Beam Pattern (43) 88
Figure 5.2-5 N=20, ULA, Cosine, Hanning Beam Pattern (44) 89
Figure 5.2-6 N = 40, ULA, Cosine, Hanning Beam Pattern (45) 91
Figure 5.2-7 N = 40, Hanning beam steering at 0.5π (46) 92
Figure 5.2-8 N = 40, Hanning beam steering at 0.5π with null constraints (47)..... 94
Figure 5.4-1 Virtual Sensor Array Model (48) 95
Figure 5.5-1 Two channel vibrations and particle signals. (49) 97
Figure 5.5-2 Details of the particle signals in the vibration signal sequence. (50)..... 97
Figure 5.5-3 Particle signals after PASB filtering. (51) 99

Figure 5.5-4 Particle signals before PASB filtering. (52)..... 101
Figure 5.5-5 Details of the particle signals for the first four particles (53) 101
Figure 5.5-6 Particle signals after PASB filtering (54)..... 102
Figure 5.6-1 Vibration signals and the corresponding phase pattern (55)..... 103
Figure 5.7-1 Original signals in both channels (56) 104
Figure 5.7-2 Outputs of the AOA filtering (57)..... 105
Figure 5.7-3 Particle signals after multiplied, rectified and low-pass filtered process (58) 106
Figure 5.7-4 Particle signals after PASB filtering (59)..... 107

List of Symbols, Abbreviations and Nomenclature

Abbreviation	Definition
ALE	Adaptive Line Enhancement
AOA	Angle of Arrival
DS	Delay and Sum
EMD	Empirical Mode Decomposition
FFT	Fast Fourier Transform
FPGA	Field-Programmable Gate Array
LMS	Least Mean-Square
LNA	Low Noise Amplifier
MCU	Micro-Control Unit
MFB	Multiple FeedBack
ML	Maximal Likelihood
NRC	National Research Council
ODM	Oil Debris Monitor
OLHP	Open Left Hand Plane
ORHP	Open Right Hand Plane
PASB	Phase Angle Selective Beamforming
RMS	Root Mean Square
SCA	Sensor Coil Assembly
SNIR	Signal to Noise Interference Ratio
SNR	Signal to Noise Ratio
TDOA	Time Difference of Arrival
TF	Transfer Function
ULA	Uniform Linear Array

Chapter 1 Introduction

1.1 Oil Condition Monitors

In order to keep machines in good conditions, the techniques of machine condition monitoring and fault detection play an important role in industry. They can not only preclude disastrous consequences of failure of mission critical mechanical components, but also help to prevent unwanted production delays [1].

Most of machine condition monitoring and fault detection systems are based on vibration analysis [2]. This is probably due to inexpensive vibration sensors and advanced techniques of vibration analysis. Even though there has been considerable research done on condition monitoring and fault detection by using such methods, oil condition monitoring on the other hand provides a direct, effective and reliable approach to machinery condition monitoring, and therefore it has also attracted the attention of researchers and sensor producers [3, 4, 5].

The basic concept of oil condition monitoring is to measure the quantity and size of metallic particles in lubrication oil of the machinery oil return lines. According to the National Research Council of Canada (NRC) technical report [6] on bearing damage research, it is observed that "early damage is a series of particle bursts", and "later damage is more progressive." It is concluded that the "quantity of particles is correlated with damage", and "quantity + rate is correlated with the remaining life of the machine". Therefore, from the particle size and count, the severity of the fault of a machine can be predicted.

On this topic, many research papers [7-14], as well as sensor producers, present different methods of acquisition of metallic particle size and count from the machinery lubrication oil system. The main methods are briefly introduced below.

In 1998, J. E. Tucker, of the Naval Research Laboratory, Washington, designed an apparatus called “LASERNET FINES Optical Oil Debris Monitor”, which provides on-site measurements of particle size distributions and shape characteristics in lubricating, hydraulic and other fluids of machines. The range of particle size measured is around 5-100 micrometers in the report. It allows distinguishing debris particles arising from different types of faults and the progression of different specific faults to be monitored. As well, the specific contamination in lubricating, hydraulic, fuel and other fluid systems is monitored at the same time [15].

In Aug. 2007, M. A. Sarangi, from the University of Akron, presented two methods of using ultrasound and capacitance to detect oil debris in machinery lubricant oil system in his master’s thesis [16]. In the ultrasound measurement structure, an oil tank is placed between an ultrasonic transmitter and receiver. It measures the power change of the ultrasonic wave when it is scattered by the existing debris in the oil tank. The result shows that the ultrasonic method can detect ferrous, non-ferrous and non-conducting particles, but it cannot distinguish them. The minimum resolution of the particle size is about 100 micrometers. In the capacitance measurement structure, two large plates are placed in parallel in a Faraday cage filled with lubrication oil. When debris exists in the oil, the capacitance of the Faraday cage will change. This method is effective to measure metallic particles as small as 63 micrometers, which the ultrasonic method is not capable of.

Previous work is not only from research institutions, but also from sensor industries. Tedeco Inc. (Technical Development Company) founded in 1951 provides an oil debris monitor sensor, called “Duplex Debris Monitor”, which can capture, retain, and remotely indicate magnetic wear debris from surface fatigue failures of oil-wetted components. The product consists of a dual chamber housing, each with its own debris sensor. Typically, only one chamber is working. When the working sensor captures wear debris, a remote signal alerts the operator to switch the flow to the alternative chamber. Without a shut-down of the machine, the isolated debris can be analyzed off-line.

In 1995, GasTop, a sensor manufacturer company in Ottawa, launched an advanced oil debris monitor (ODM) in the market, called MetalScan [17, 18]. This sensor consists of a three coils assembly. Two of them are field coils which generate a balanced and opposite-polarized magnetic field, while the third coil, called the sense coil, is used to detect the disturbance of the magnetic field. The sense coil is between the two field coils and is highly sensitive to the change of magnetic fields. When a ferrous or non-ferrous particle passes through the field coils, a weak field disturbance is induced and captured by the sense coil. After electronic signal processing, the captured disturbance becomes the particle signature. The minimum detectable particle size is dependent on the diameter of the oil flow tube. For example, with a 3/8" oil tube, the resolution for ferrous spherical particle is 100 um, for non-ferrous it is 405 um; with a 1 ¼" oil tube, the minimum detectable particle size is 290 um for ferrous particles, and 850 um for non-ferrous particles [19].

Certainly, there are many other methods [36, 38-40] which are similar to above mentioned methods. In summary, they can be classified in terms of physical parameters such as: optical [26-29, 37], ultrasonic [16], capacitive [16, 30], and electromagnetic methods [41-44]. Each method has its advantages and disadvantages. From a research of the industrial market, the electromagnetic method prevails for oil condition monitoring [20-23, 45-46]. The reason why industries prefer the electromagnetic method to others in oil condition monitoring is because:

1. Sensors are introduced to detect machine faults, but the sensors themselves may become ineffective after operation. This requires sensors to be more reliable than the monitored components of the running machines. The sensors with simple, straight structures are preferred in industry to complex sensors because they are more reliable and more convenient for maintenance. Most of electromagnetic sensors adopt a direct, straight oil path passage scheme instead of a bending, circular, or housing structure, as other sensors normally require. [31]

2. Electromagnetic sensors are mostly sensitive to metallic particles, which carry the information of the fault severity from the surface fatigue gears or bearings. Other methods such as optical

methods are sensitive to not only metallic particles, but also the contaminations in fluids, which are regarded as interference. Distinguishing and eliminating the interference is sometimes very difficult for the oil condition monitors [32].

3. The low cost of electromagnetic-sensors is another advantage over other sensors.

Among electromagnetic ODMs, the GasTop product, MetalScan, is the most attractive to our attention. In fact, there have been considerable research activities based on GasTop ODMs, and several research papers [1-3, 32] and thesis [33] from both GasTop and Dr. Ming Liang's group from the Department of Mechanical Engineering at the University of Ottawa were published in the past few years.

1.2 GasTop Electromagnetic Oil Debris Monitor

In May 1996, Dave Muir, from GasTop Ltd., introduced the structure, the operation principle, and the performance of the MetalScan oil debris monitor, in the Aerospace Atlantic Conference [32]. A simple introduction of the product has been outlined in the previous section. Here a more detailed description of MetalScan is provided. The internal mechanical structure of the product is shown in Figure 1.2-1 in the next page.

This structure was first invented and patented by Robert W. Kempster, and Douglas B. George in Aug. 1995 [34]. The elaborate design has the following characteristics:

1. The whole sensor coil assembly (SCA) is symmetrical to the vertical central line of the sense coil. The left and right field coils are wound in opposite directions such that the magnetic field from each section is cancelled out at the plane of the sense coil.

2. The sense coil is highly sensitive to the disturbance of magnetic field caused by ferromagnetic or conductive particles. When a metallic particle passes through the coiled structure, the coupling

in the sense coil is disturbed as the particle first interacts with the field of the upstream section and then with the field of the downstream section of the field coils. When an oil debris passenger passes by, it stimulates an approximately sine wave impulse which is taken as the signature of the particle. Figure 2.1-2 shows an example of particle signatures for a ferromagnetic particle.

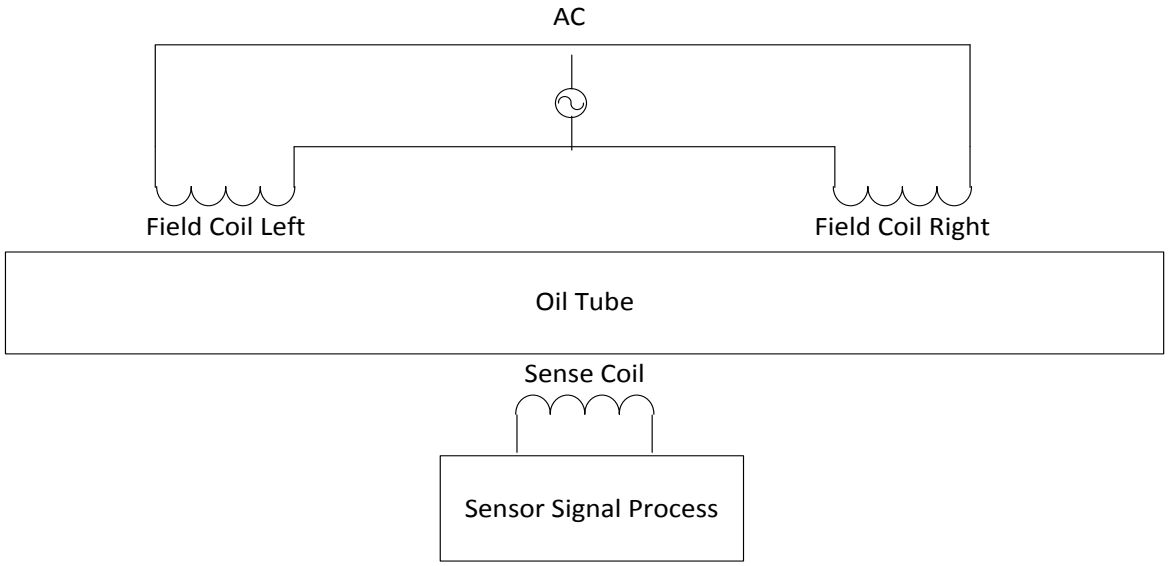

Figure 1.2-1 Oil Debris Monitor Internal Structure (1)

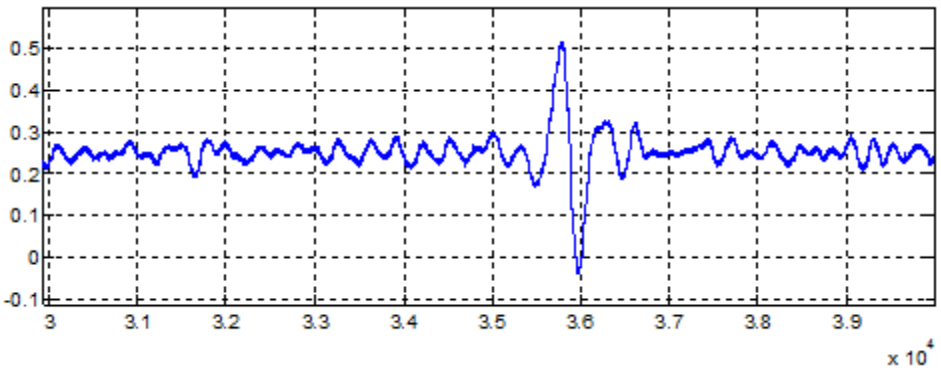

Figure 1.2-1 Ferromagnetic Particle Signatures (2)

3. The excellence of the design is in the separation of the field coil and the sense coil, which is vital for a sensitivity increase. Such a structure allows high currents flowing in the field coil to

increase the intensity of the magnetic field, while the coupling in the sense coil is also boosted. When a metallic particle enters a strong and intense field, the disturbance captured by the sense coil is proportionally increased. This will produce a high sensitivity to particle size comparing with the other methods for the same size of oil tube. From GasTop product specifications [19], the sensitivity of a 3/8" tube ODM can reach 100 um for ferrous particles and 405 um for non-ferrous particles.

4. The oil path of the sensor is simply a direct straight tube with at least 3/8" in diameter, and this will not cause any clog problem.

The MetalScan ODM sensor has shown a superior performance compared to other non-electromagnetic sensors, however the particle measurement suffers from environmental vibration interference. The sensor sensitivity to vibration is so large that the particle signal can be immerged in the vibration signals. This makes it hard to distinguish the particle signal when strong vibration interference happens. Below is a figure showing a particle signal with interference from vibrations.

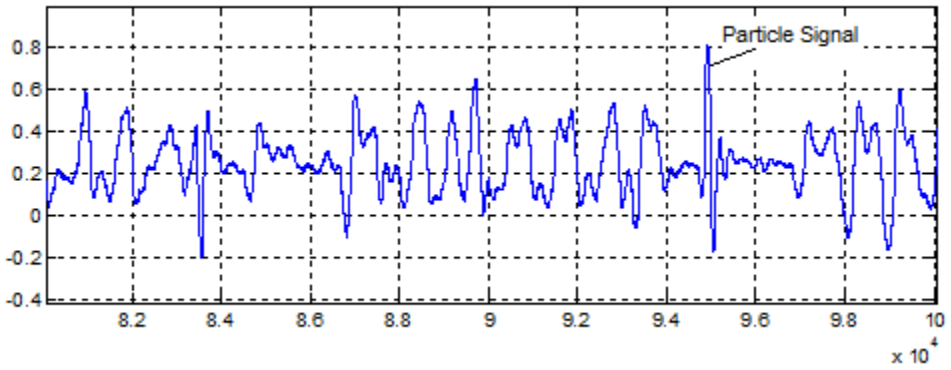

Figure 1.2-3 Particle signature immerged by vibration interference (3)

In order to solve the problem, in June and August 2009 Iman Soltani Bozchalooi and Dr. Ming Liang published two papers [1,2], proposing some new methods: the Empirical Mode

Decomposition (EMD) method, and the Adaptive Line Enhancement (ALE) method. The two papers show that these two methods can extract the particle signals from the mixture of the particle and vibration signals under some conditions. However, there are still some concerns with the proposed methods, as reported in one of the papers: “It is very difficult to guarantee reliable results in all circumstances. In practice, the vibration interferences can be very complicated in nature which can affect the performance of the EMD”.

One of the concerns is that the environmental vibration interference may happen in a random fashion, and it can last a variable duration. It may appear in the form of a constant and single frequency interference (as the papers assume), but it may also appear as a shock impulse. If the vibration is more general or random, such as a simple shock impulse, the previous two methods can't be guaranteed to be effective, because they lack the method to distinguish random vibrations and particle signals. In practice, random vibrations are very common. For example, an automobile riding on a rough road, a vessel boat sailing on an ocean wave, and an airplane flying in storms, will all cause random vibrations. If the sensor is installed on transportation vehicles, random vibrations cannot be avoided.

Random vibration is not a vibration with an inherent natural frequency, but a characteristic of the excitation or input from outside. It is different from the vibration caused by an engine or tires in a regular cycle. It’s a non-deterministic motion, without constant amplitude and frequency, and it is much more complicated than a cyclic vibration.

This thesis is targeted to solve the problem of a particle signal in the presence of random vibration interference. My contributions in the thesis include:

1. The design of a prototype for a novel ODM sensor structure.
2. The development of an algorithm based on angle of arrival (AOA) for the detection of particles in ODM signals under conditions of vibration interference.
3. The development of an algorithm based on time difference of angle of arrival (TDOA) for the detection of particles in ODM signals under conditions of vibration interference.

4. The design of a beamforming method called PASB to reduce the interference from vibrations in a noisy ODM signal and allow a better detection of particles.
5. The adaptation the developed AOA method to perform filtering and reduce the interference from vibrations in a noisy ODM signal.

The material included in this thesis is organized as follows. The hardware design of the prototype sensor is introduced in chapter 2. Three signal processing algorithms are then developed in order to detect the particle signals, and they are presented in chapter 3, 4, and 5. The comparison of the performance of each algorithm is given in chapter 6. A conclusion will follow.

Chapter 2 Design of a prototype sensor

2.1 Introduction to the Prototype

"In nature, purely sinusoidal vibration is a rare phenomenon. A more common phenomenon is random vibration or sinusoidal vibration plus background random vibration with a broadband frequency range" [35]. In line with this statement, we can affirm that laboratory tests based on random vibrations reflect a vibration interference commonly found in real world.

To solve the random vibration problem in ODM sensors, we must deal with a question first. How to distinguish a random vibration and a particle signal to be detected?

Based on the MetalScan ODM structure, it is impossible to directly solve it. Random vibrations caused by an external excitation are completely unpredictable, and the vibration waveform may be very close to a particle signal. There isn't any special character to differ vibration noise from a particle signal.

The concept of differential amplifiers commonly used in electronics can give us a very good hint on a possible solution. When a signal is sent from a remote transmitter through a pair of wires, the signal is interfered by environmental electromagnetic noise. If a single transistor amplifier is used, the signal will suffer from 3 kinds of noise: ground and power-supply noise, input common-drift noise, and internal bias drift noise. Directly restoring the signal from those noises would be very costly. A good solution to the problem is to represent the signal to be transmitted by two floating differential voltages. A differential amplifier boosts the difference between the two voltages and rejects the common noise components. It performs well for the transmission of signals from a remote site. The famous digital data transmission interface standard, RS422, has adopted the method of differential signaling, with the concept of a differential amplifier.

Similar to this differential signaling, a novel structure for an ODM sensor is created in this thesis:

1. On the same oil path, create two channels instead of one channel as in current designs, where a channel means a complete sensor unit including two field coils and one sense coil (more details to follow).
2. Both channels must have approximately equivalent sensitivity to particles and to vibrations.
3. Both channels must be fixed to a rigid tube, apart with a moderate distance, and ensuring that the whole structure can be approximately taken as an ideal rigid body.

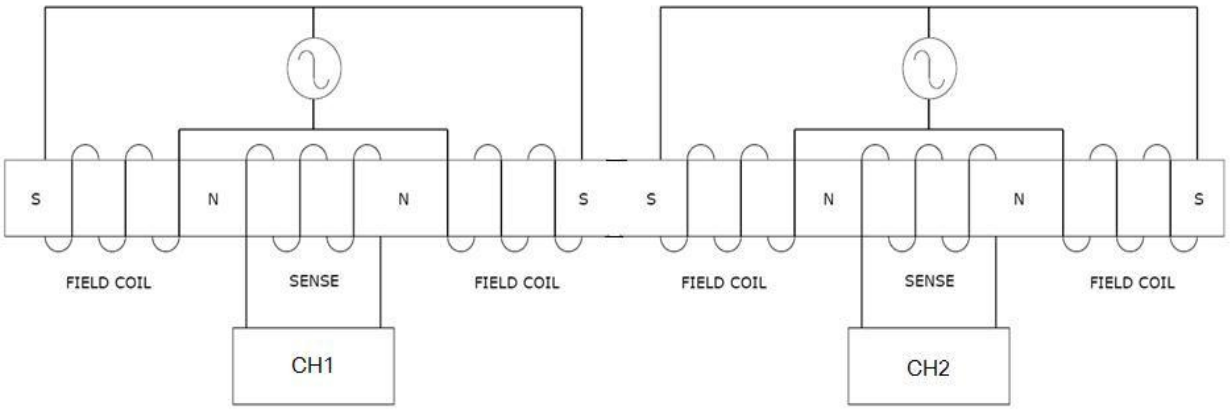

Figure 2.1-1 Two-channel ODM structure (4)

The reason why the system with two channels instead of previous one-channel designs is effective is because it allows a way to distinguish vibration and particle signals. Vibration is a "common" interference appearing almost simultaneously on both channels, while a particle signal is a "delayed" signal between the two sensors, comparing the downstream channel to the upstream channel. This is the core idea of the prototype design.

2.2 Common Interference

The declaration that "vibration is a common interference on both channels" is true if the assumption of the whole sensor structure being a rigid body is valid, and if the sensor responses are nearly identical.

A rigid body means a solid body in which deformation is neglected. As a result, the distance between any given points in the body is constant in time regardless of the external force, and the force on either point is equally translated on the other point.

Vibration is a mechanical oscillation around an equilibrium point, which may be a periodic motion or a random motion. Any point in the rigid body has the same displacement when a translation is applied and the same angular displacement when a rotation is applied (except the axis points). When a rigid body vibrates, no matter whether it is a translation or rotation or mixed motion, all points except the axis points will have the same oscillation frequency and the same phase because of the same displacement or the same angular displacement. As the two- channel structure is a rigid body, vibration causes the same oscillation frequency and the same phase on both channels. It is taken as a "common interference" on the two channels.

2.3 The Physical Nature of the Proposed Sensors

In the previous chapter, the advantages of the MetalScan sensor structure have been outlined. Here the physical nature of the sensor is further explored to better understand the reason why a tiny metallic particle can be detected by such a sensor.

The magnetic field distribution of the sensor is our main interest. According to the Biot-Savart law [47], a wire with steady electric current will generate a net magnetic field (or magnetic flux density) *B*:

$$\boldsymbol{B} = \frac{\mu I}{4\pi} \int \frac{d\boldsymbol{l} \times \hat{\boldsymbol{r}}}{r^2} \qquad (2\text{-}3\text{-}1)$$

where μ is the magnetic constant $4\pi\times10-7$ V·s/(A·m), I is the current, $d\boldsymbol{l}$ is a vector representing a differential length element of the wire, $\hat{r}$ is a displacement unit vector in the direction from the wire to the location of the field, and r is the distance between the wire element and the location of the field.

For a solenoid, as in Figure 2.3-1, the magnetic flux density *B* at the center of the solenoid can be deducted as:

$$\boldsymbol{B} = \frac{\mu n I}{l}\hat{\boldsymbol{x}} \qquad (2\text{-}3\text{-}2)$$

where *n* is the number of coil turns in the solenoid, *l* is the length of the solenoid, and $\hat{\boldsymbol{x}}$ is a unit vector in the direction of the axis at the center of the solenoid.

For the same solenoid, the magnetic flux density *B* at the end of the solenoid can be written as:

$$\boldsymbol{B} = \frac{\mu n I}{2l}\hat{\boldsymbol{x}} \qquad (2\text{-}3\text{-}3)$$

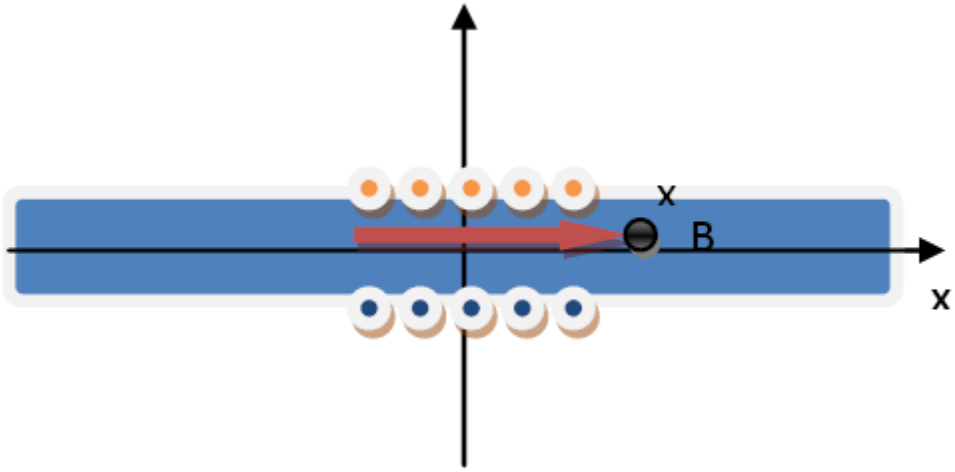

Figure 2.3-1 Magnetic flux *B* in a solenoid (5)

Suppose that the solenoid coil is very narrow, such that it can be taken as one circle coil with current *nI*, as shown in the Figure 2.3-2:

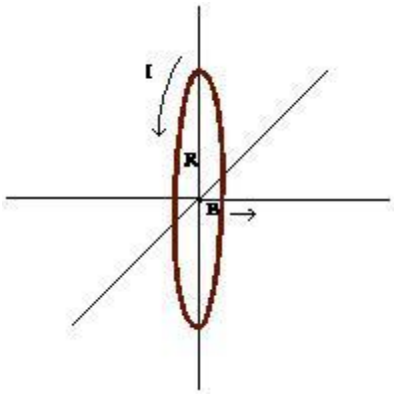

Figure 2.3-2 Magnetic flux *B* at the center of a circular coil (6)

Then the magnetic flux density ***B*** at position *x* will be:

$$\boldsymbol{B} = \frac{\mu n I R^2}{2(x^2 + R^2)^{\frac{3}{2}}}\hat{\boldsymbol{x}} \qquad (2\text{-}3\text{-}4)$$

where R is the radius of the solenoid and x is a position along the axis at the center of the solenoid. The formula 2-3-4 clarifies the fact that the magnetic flux density ***B*** dramatically decreases with the distance x away from the coil center. The Figure 2.2-3 shows the fast attenuation under the conditions $\mu = 4\pi \times 10^{-7}, n = 60, I = 2mA,\ R = 1cm. x = -5 \ldots 5\ cm.$

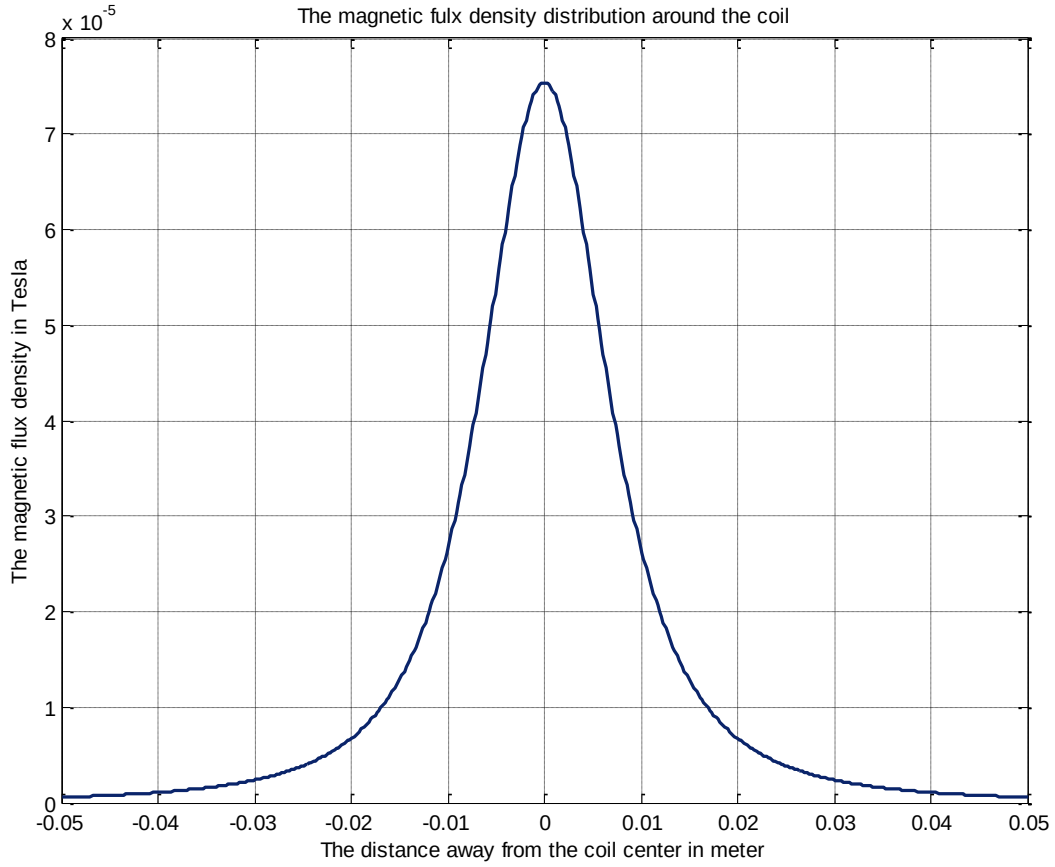

Figure 2.3-3 The magnetic flux *B* distribution around the center of a circular coil (7)

When two field coils with opposite current direction are closely placed in the MetalScan sensor system, the magnetic flux density distribution is as follows:

$$\boldsymbol{B} = \frac{\mu n I R^2}{2((x+x_0)^2+R^2)^{\frac{3}{2}}}\hat{\boldsymbol{x}} - \frac{\mu n I R^2}{2((x-x_0)^2+R^2)^{\frac{3}{2}}}\hat{\boldsymbol{x}} \qquad (2\text{-}3\text{-}5)$$

where x_0 is the distance between the two sensors. Figure 2.3-4 shows the magnetic flux density distribution of the MetalScan sensor system, with two field coils inside. The origin of the coordinates is selected at the center between the two field coils.

If the current flowing in the coils is a high frequency alternative current instead of a steady or constant DC current, then the line shape in Figure 2.3-4 represents the envelope of the magnetic flux density.

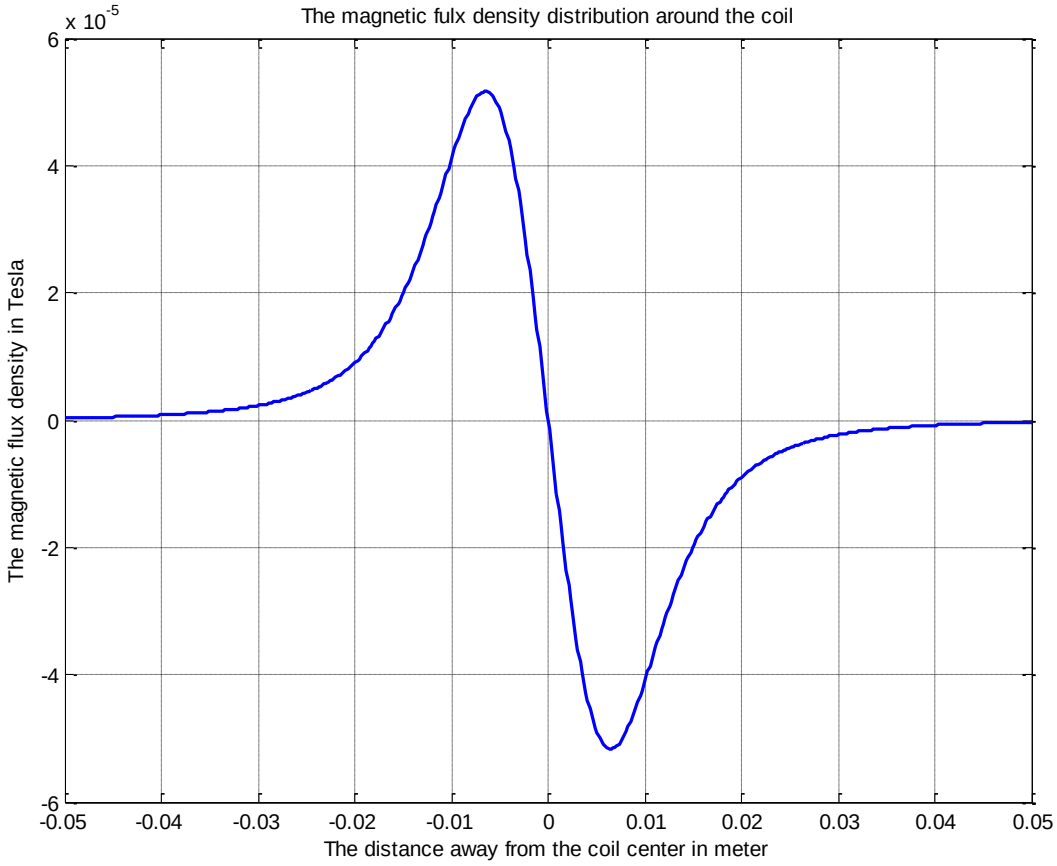

Figure 2.3-4 The magnetic flux around the center of the two field coil system (8)

In Figure 2.3-4, the magnetic flux density at the center between the two field coils is zero, if they are perfectly balanced. In practice, it is impossible to make field coils perfectly balanced and the flux density found there would not be zero.

The reason why the sense coil is placed at the center instead of other locations is because it is the steepest slope at the center in the figure, which means that any disturbance there will cause large changes. The center is thus the most sensitive point to capture a particle trace.

2.4 Solenoid Design

In order to reach the best performance, it is necessary to determine the optimal parameters of the coils under some boundary conditions. Usually, boundary conditions are from practical limitations when a system is designed. In our solenoid coil design, how many turns of the coil will be optimal under the following limitations if a maximal magnetic flux density at the center of the solenoid is desired ?

Given the following practical limitations:

Source supply voltage	V = 10 V,
Frequency	f = 100 kHz,
Solenoid radius	R = 1cm,
Coil DC resistance	r = 10 Ω,
Solenoid length	l = 1 cm
Coil wire diameter	d = 0.4 mm
Permeability of the solenoid	$\mu = 4\pi \times 10^{-7}$ H/m

A design procedure was established:

Step1: Find a normalized *B* as a function of *n*, where *n* is the number of coil turns.
From formula 2-3-2, and just considering the magnitude, we have:

$$B = \frac{\mu n I}{l} \qquad (2\text{-}4\text{-}1)$$

This expression means that the magnetic flux density is proportional with *nI*, when other parameters are constant. If *I* is the current flowing in the coil, it depends on the source voltage and the coil impedance by Ohm's Law.

$$I = V/Z \qquad (2\text{-}4\text{-}2)$$

The impedance of the coil is expressed as:

$$\hat{Z} = r + j\omega L \tag{2-4-3}$$

where L is the inductance of the coil, r is the resistance of the coil, and ω is the angular frequency of the external excitation. The difference between Z and $\hat{Z}$ is that the former represents the magnitude only, while the latter is a complex impedance.

The inductance of a solenoid is expressed as [16]:

$$L = \frac{\mu n^2 A}{l} \tag{2-4-4}$$

where A is the cross-section area of the solenoid, and l is the length of the coil.

Inserting 2-4-3 in 2-4-2, we have:

$$\hat{Z} = r + j\omega \frac{\mu n^2 A}{l} \tag{2-4-5}$$

and since Z is the magnitude of the complex $\hat{Z}$ we obtain:

$$Z = \left|\hat{Z}\right| = (r^2 + c^2 n^4)^{\frac{1}{2}} \tag{2-4-6}$$

where c is a constant representing :

$$c = \omega \frac{\mu A}{l} \tag{2-4-7}$$

Now, inserting 2-4-6 in 2-4-2, and then in 2-4-1, we have:

$$B = \frac{\mu n V}{l Z} \tag{2-4-8}$$

$$B = \frac{\mu n V}{l(r^2 + c^2 n^4)^{\frac{1}{2}}} \tag{2-4-9}$$

Step 2: Plot the figure of *B* vs *n* and then find the optimal *n* such that *B* is maximum.

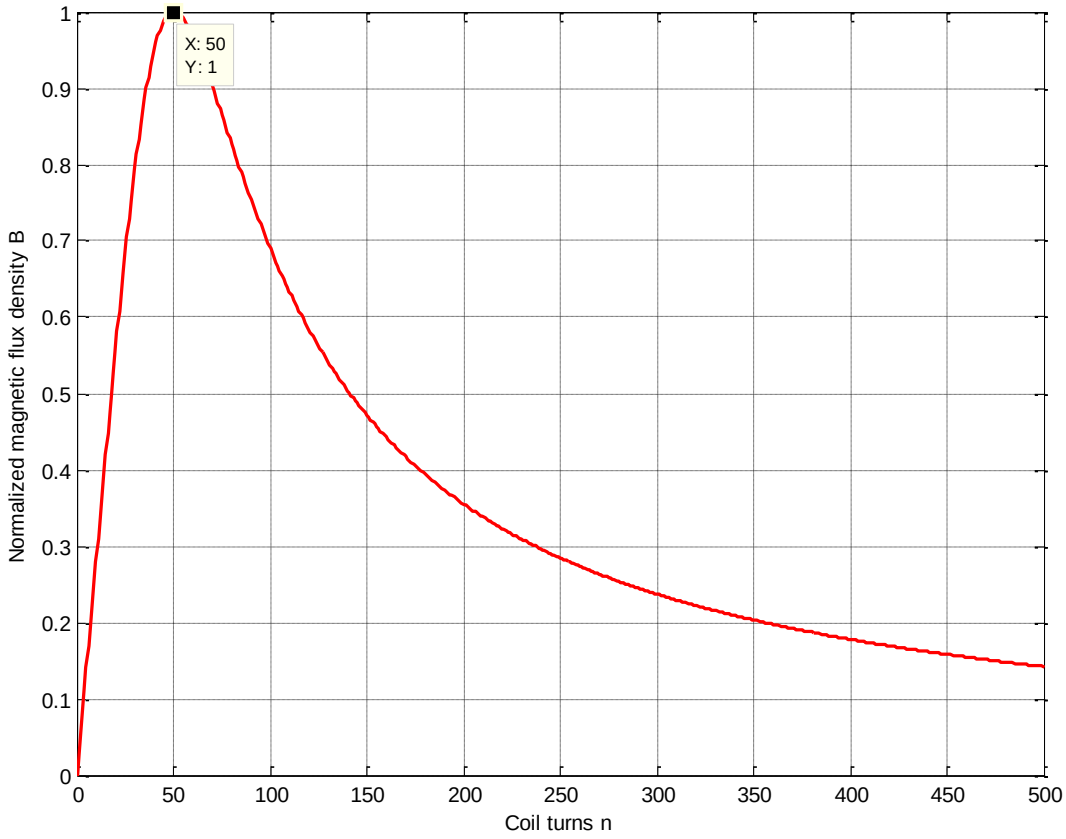

Figure 2.4-1 The magnetic flux density *B* vs coil counts *n* (9)

From Figure 2.4-1, there exists a unique optimal value of coil turns $n = 50$ which makes the normalized magnetic flux density *B* maximal, and this *n* is the desired value.

Step 3: Verify that the calculated optimal coil turns *n* can be reached in practice.

The designed solenoid is 1 cm long, $l = 1$cm. The coil wire diameter is $d = 0.4$ mm. Consequently, one layer of wiring will have 25 turns. 50 turns will thus occupy two layers.

In practice, there are some air gaps between the coil turns. So three layers may be required to wrap 50 turns. With the optimal number of coil turns, the magnetic field in the center of the solenoid is maximal, and the sensibility of the system will also be largest.

2.5 Electronic Design

The purpose of the electronic design is to acquire the particle signal from the sense coil when the field coils are driven by a high frequency excitation signal. This process is implemented by an analog circuit in our design.

When designing an electronic system, there are many ways to achieve a result: analog processing, digital processing, or mixed processing, where analog processing means that signals are processed by analog circuits, while digital processing means that signals are processed by digital circuits, such as MCUs, FGPAs or computers. The selection of the processing methods is based on capability, simplicity, and cost to realize the functions of the system. Even though digital processing has great advantages over analog processing with today's digitization technology in the aspects of accuracy, reliability, and controllability, some analog processing is necessary and cannot be replaced in our design. This is because:

1. Digital signal processing is suitable for analog signals which can be quantized to digital codes. For analog signals which are too small compared to the quantization step size, analog processing is inevitable. In the case of our design, a particle signal caused by the disturbance of the magnetic field is so weak that it is smaller (or of the same order) as the quantization resolution of typical A/D converters. Thus the use of an analog filter and amplifier is necessary.

2. Driving the field coils needs a large current, and this cannot easily be achieved with digital circuits.

3. Before sampling with an A/D converter, an anti-aliasing filter is essential if the signal to be sampled has components higher than half the sampling rate. This filter has to be an analog filter.

Therefore, the electronic design of an analog circuit will be described in this section. The block diagram of the electronic design is shown as follows:

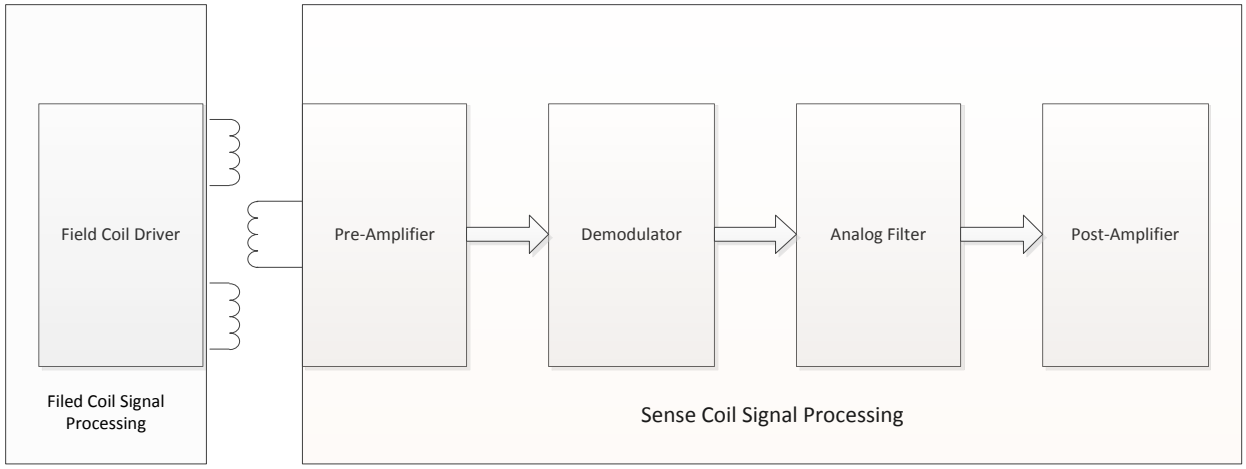

Figure 2.5-1 Block diagram of the electronic design (10)

2.5.1 Field Coil Driver

The function of the Field Coil Driver is to provide high-frequency intensive alternative current for the field coils. The current frequency is selected above 100 kHz. This is because of the Eddy current effect which happens in high-frequency electromagnetic fields, and conductive particle detection is based on the Eddy current effect.

The source of the Field Coil Driver is from an adjustable function generator, which provides 100 kHz – 1 MHz sinusoidal signals. But this signal cannot directly drive the field coil, because its power output is not sufficient. A power amplifier IC is needed to realize the requirement. The schematic design is shown in Figure 2.5-2.

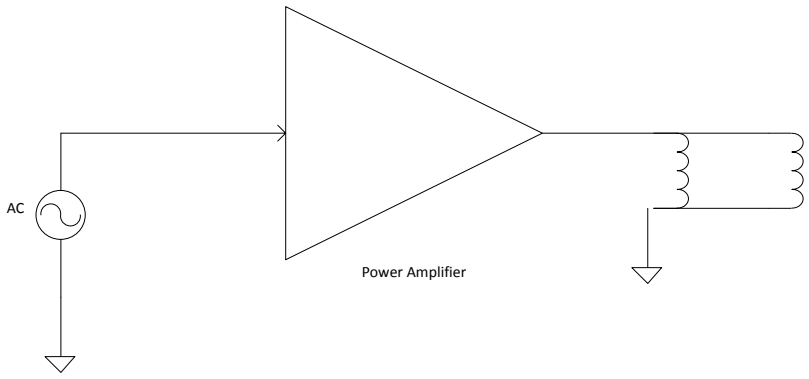

Figure 2.5-2 Field Coil Driver Design (11)

The LT1210 is a high-performance power amplifier IC, whose maximal current can reach 1 A, which is enough to drive the field coils.

2.5.2 Pre-Amplifier

The function of the Pre-Amplifier is to amplify a low-level signal up to line-level. Usually the signal coming from a sensor is a small electronic signal with weak power, easily disturbed by external interference. A pre-amplifier is placed close to the sensor to boost the signal strength for further processing. The noise performance of the pre-amplifier is critical. The final signal to noise ratio (SNR) is dependent on the input SNR and the pre-amplifier's noise figure.

The TL072 is a JFET-input operational amplifier, with low-noise, low input bias, and fast slew rate, suited for high-fidelity and pre-amplifier applications. In the pre-amplifier design of the prototype, the TL072 is adopted to amplify the sensor signal. The requirements of the design are as follows:

1. The input resistance is above 1M Ω.
2. The amplifier gain is at least 30dB.
3. The output RMS noise voltage is no more than 10mV.

The schematic design of the Pre-Amplifier is as shown in Figure 2.5-3.

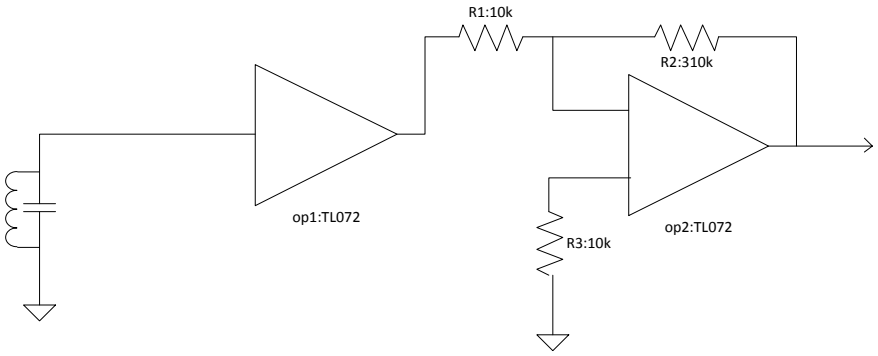

Figure 2.5-3 Pre-Amplifier Design (12)

Description:

1. The operational amplifier *op1* is a follower configuration with unit gain and high input resistance (greater than 10MΩ). It absorbs little power from the sense coil.

2. The operational amplifier *op2* is an inverting amplifier with voltage gain 30 dB. The function of the amplifier is to boost the signal strength in the previous stage. Usually the signal coming from the sense coil is a 10 mV to 100 mV modulated carrier signal. After 30 dB boosting, the signal is amplified to about 1V to 5V, strong enough for further processing.

3. The datasheet of the TL072 does not state the noise figure, instead it gives the equivalent input noise voltage 18 nV/Hz$^{1/2}$, to describe the noise effect under a work frequency 100 kHz and a normal temperature of T=25^{o}C. From this value, the thermal noise at the output would be estimated with the following method when the voltage gain is 30dB, and the bandwidth is 100Hz. According to the datasheet of the TL072, the equivalent input noise voltage of the circuit is:

$$V_n = \sqrt{e^2 + i^2 R_g + 4KTR_g} \qquad (2\text{-}5\text{-}1)$$

where e is the input noise voltage of the amplifier, i is the input noise current of the amplifier, R_g is the external input resistance, T is the temperature in Kelvins, and K is the Boltzmann constant (1.38×10^{-23}).

We assume that the noise figure of the amplifier *op1* is 0 dB, which means that the noise introduced by the amplifier *op1* itself can be neglected. The assumption can be regarded as true because the first stage amplifier is a follower with unit gain, and the amplifier is low-noise. So the SNR at the input and output is almost the same.

In the second stage, R_g can be found as:

$$R_g = \frac{R_1 R_2}{R_1 + R_2} + R_3 \tag{2-5-2}$$

$$R_g = \frac{10k\Omega \times 100k\Omega}{10k\Omega + 100k\Omega} + 10k\Omega = 19.9k\Omega \tag{2-5-3}$$

From the datasheet of the TL072, it is found that $e = 18nV/\sqrt{Hz}$, $i = 0.01pA/\sqrt{Hz}$, K= $1.38 \times 10^{-23} J/\text{degree Kelvin}$, $T = 300$ degrees Kelvin, from which we have:

$$V_n = \sqrt{18nV^2 + 0.01pA^2 \times 19.9k\Omega + 4 \times 1.38 \times 10^{-23} J/\text{deg.} \times 300 \text{ deg.}} \tag{2-5-4}$$

$$V_n^2 = 324nV^2/Hz \tag{2-5-5}$$

As the bandwidth is 100Hz:

$$E_n^2 = 324nV^2/Hz \times 100Hz = 32400nV^2$$

where E_n^2 is the RMS noise voltage at the input. Then the RMS noise voltage at the output will be:

$$\mathcal{E}_n^2 = 32400nV^2 \times 31.3(30dB) = 1.014 \times 10^6 nV^2 \tag{2-5-6}$$

So the average noise voltage at the output becomes:

$$\mathcal{E}_n = 1.01mV \quad (2\text{-}5\text{-}7)$$

In summary, the amplified signal is about 1V after the pre-amplifier, while the thermal noise caused by the amplifier itself at the output is 1.01mV. The noise introduced by the amplifier can be neglected compared to the useful output signal.

2.5.3 Demodulator

The excitation signal on the field coils is a high-frequency AC signal and the output of the sense coil is a modulated high-frequency AC signal when particles pass through the ODM sensor. The demodulator is designed for extracting the modulating signal, i.e. the particle signal.

There are two reasons why the excitation signal of the field coil won't use a DC current:

1. A steady DC current would cause the sensor to become a magnetic bar; this would stick passing small ferrous particles on the internal wall of the solenoid tube, losing the function of detection.

2. The detection using a sensor excited with DC current won't be efficient to detect metallic particles, because the Eddy current effect won't be applied to the metallic particles under a low frequency magnetic field.

Without any doubt, the excitation signal of the field coils must be a high frequency alternating current (usually the frequency is greater than 100 kHz), and this signal is the carrying signal. A sensor signal model is described below.

By observation, the signal coming from the sense coil is a mixture of the excitation signal and the disturbance induced from a particle. Without a particle signal, the sensor output signal is the excitation carrying signal from the field coils only:

$$S_{out} = x_c(t) \tag{2-5-8}$$

With a particle disturbance, the sensor output signal is the superposition of the carrying signal plus a small change induced by the particle:

$$S_{out} = x_c(t) + x_{ch}(t) \tag{2-5-9}$$

This small change signal completely depends on the influence of the particle and the intensity of the carrying signal:

$$x_{ch}(t) = Ax_c(t)x_p(t) \tag{2-5-10}$$

This expression shows that the change is the common influence of the magnetic field from the field coils and the particle inducing ability. Here *A* is a small constant reflecting the sensitivity.

If formula 2-5-10 is a good assumption reflecting the real world, the modulated signal from the sense coil will be:

$$S_{out} = x_c(t) + Ax_c(t)x_p(t) \tag{2-5-11}$$

$$S_{out} = x_c(t)(1 + Ax_p(t)) \tag{2-5-12}$$

Based on the model, some analysis is made as follows:

1. Usually $x_c(t)$ is a strong intensive signal excited by the field coils with high frequency f_c, while x_p is a weak signal induced by passing particles with low frequency f_p. The modulated signal S_{out} is the carrying signal with a small disturbance.

2. To extract x_p from the modulated signal, the simplest way is to use a demodulator, which can be a mixer or a rectifier. The following describes the demodulation process in a mathematical way. In the frequency domain, 2-5-12 becomes:

$$S_{out}(\omega) = \frac{1}{2\pi} X_c(\omega) \otimes \left(1 + AX_p(\omega)\right) \tag{2-5-13}$$

where $\otimes$ means a linear convolution operation. The function of a mixer is a multiplication. If $S_{out}(t)$ mixes with $x_c(t)$ in the time domain, then in the frequency domain, this becomes:

$$S_{mix}(\omega) = X_c(\omega) \otimes \left(1 + AX_p(\omega)\right) \otimes X_c(\omega) \tag{2-5-14}$$

$$S_{\mathrm{mix}}(\omega) = \left(1 + AX_{\mathrm{p}}(\omega)\right) \otimes \left(X_{\mathrm{c}}(\omega) \otimes X_c(\omega)\right) \tag{2-5-15}$$

If $x_c(t)$ is a sinusoidal signal with single frequency ω_0, then $X_c(\omega)$ will be:

$$X_c(\omega) = \delta(\omega + \omega_0) + \delta(\omega - \omega_0) \tag{2-5-16}$$

$$\mathrm{X_c}(\omega) \otimes \mathrm{X_c}(\omega) = \delta(\omega + 2\omega_0) + \delta(\omega - 2\omega_0) + 2\delta(\omega) \tag{2-5-17}$$

Inserting 2-5-17 in 2-5-15, the three terms of the expression become:

$$\left(1 + AX_p(\omega)\right) \otimes \delta(\omega + 2\omega_0) = 1 + AX_p(\omega + 2\omega_0) \tag{2-5-18}$$

$$\left(1 + AX_p(\omega)\right) \otimes \delta(\omega - 2\omega_0) = 1 + AX_p(\omega - 2\omega_0) \tag{2-5-19}$$

$$\left(1 + AX_p(\omega)\right) \otimes 2\delta(\omega) = 2 + 2AX_p(\omega) \tag{2-5-20}$$

The final expression becomes:

$$S_{mix}(\omega) = 4 + AX_p(\omega + 2\omega_0) + AX_p(\omega - 2\omega_0) + 2AX_p(\omega) \tag{2-5-21}$$

After filtering out the high frequency components and the DC component in 2-5-21, the processed signal will only leave the particle disturbance component $AX_p(\omega)$. It is the wanted signal after amplification.

A rectifier can also perform the same function as a mixer. It is the simplest way for the detection of an amplitude modulated signal. It is adopted in our design because of the resulting low cost. The schematic design is as follows:

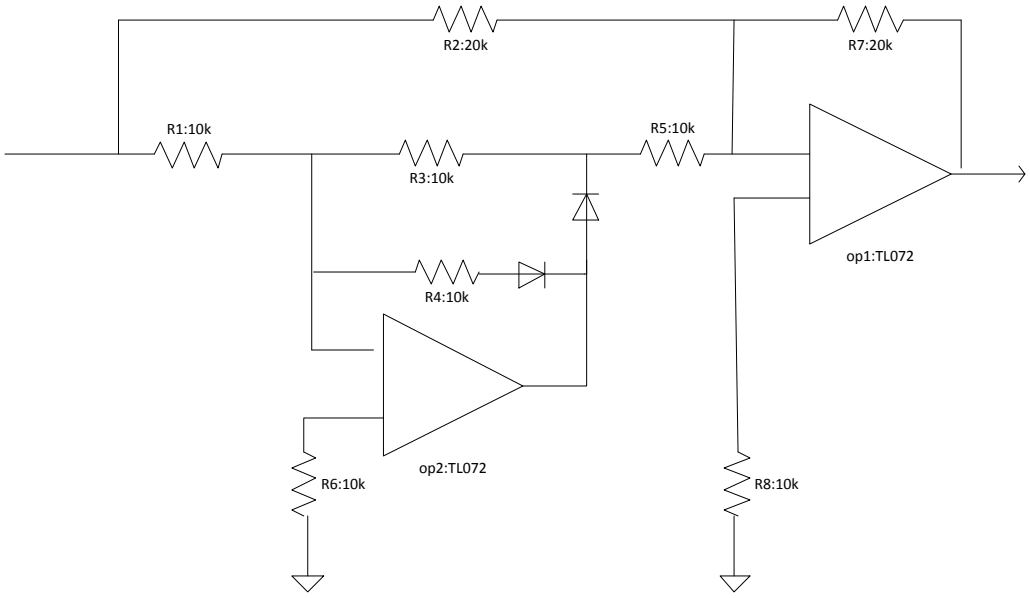

Figure 2.5-5 Rectifier/Demodulator Design (13)

2.5.4 Analog Filter

In the previous section, the demodulator performs the separation of the low-frequency modulating signal from the high-frequency carrying signal. In this section, a low-pass filter is designed, filtering out the unnecessary high-frequency signal.

Even though there are many kinds of CAD software to help designing analog filters quickly, it is still necessary to understand the theorem of the analog design behind them. In the following, the details of how to design a low-pass filter for the ODM prototype are described.

1. To design a low-pass analog filter, the first step is to specify the requirements of the filter. By estimation of the bandwidth of the particle signal, the parameters of our low-pass filter are specified as follows:

1. Cut-off frequency, f_c: 100 Hz
2. Pass-band frequency, f_p: 80 Hz
3. Stop-band frequency, f_s: 200 Hz
4. Minimal gain in pass-band, A_p: $-0.5\ dB$
5. Maximal gain in stop-band, As: $-40\ dB$

2. The second step is selecting a suitable low-pass filter type and normalizing the filter parameters.

The major filter types used in analog filter design are Butterworth, Tchebychev, Inverse Tchebychev, Elliptic, and Bessel. Each type has its advantages and disadvantages. As our requirements of the low-pass filter are not very constraining, any type can be used. Since the Butterworth filter is the simplest in its theoretical design, and it also provides the maximum passband flatness, the following design is based on the Butterworth filter.

The low-pass Butterworth filter is defined with the following frequency response [20]:

$$|H(j\Omega)|^2 = \frac{1}{1+\Omega^{2N}} \qquad (2\text{-}5\text{-}22)$$

where Ω is the angular frequency and N is the filter order. As N becomes higher, the filter becomes closer to an ideal low-pass filter. The squared magnitude frequency response is as shown below:

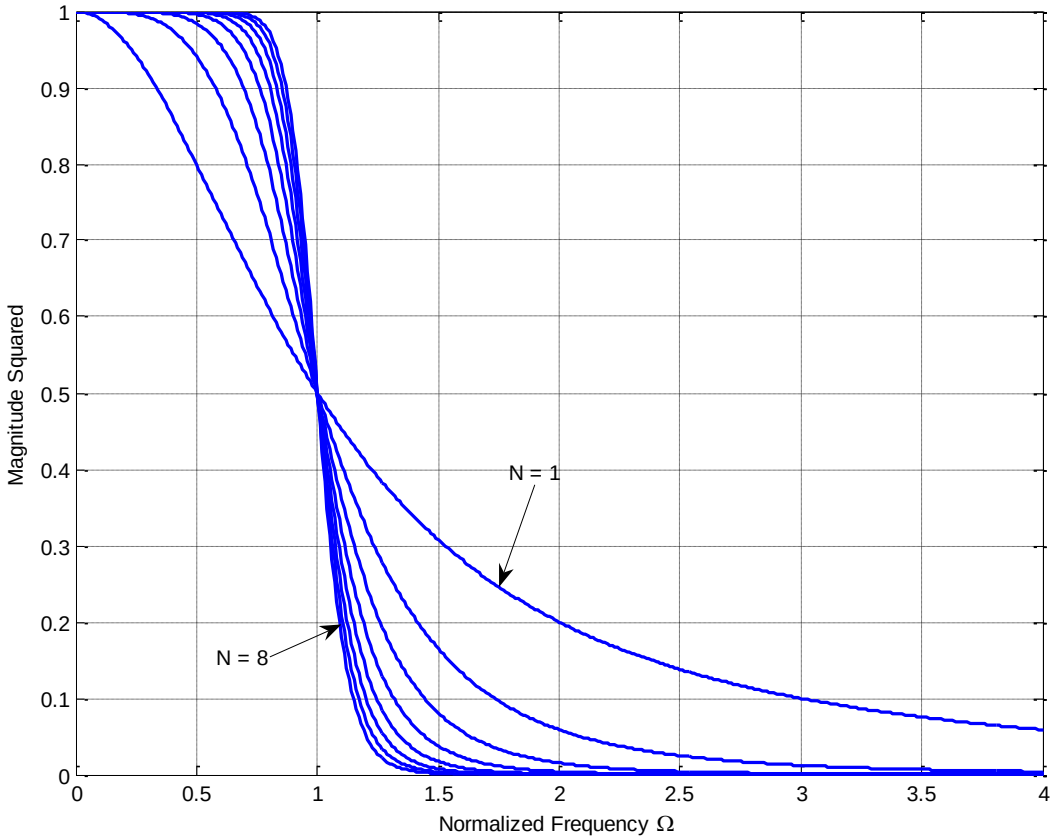

Figure 2.5-6 Butterworth Frequency Response Design (14)

Regardless of the order, all the responses have a cut-off frequency of 1, and a magnitude squared of 0.5 at the cutoff frequency. This is the most apparent characteristic of a Butterworth filter. The responses in Figure 2.5-6 are normalized frequency responses, with a cutoff frequency of 1.0. If a desired frequency response can be normalized this way, the required order can quickly be found by calculation or by comparing with the figure.

The normalized frequencies for the prototype low-pass filter are as follows:

a. Pass band frequency F_p: 0.8
b. Cutoff frequency F_c: 1

c. Stop band frequency F_s: 2

3. The third step is to calculate the required order *N*

From 2.5-22, let $M = |\frac{H(j\Omega)}{H(j0)}| = |H(j\Omega)|$, then find *N*:

$$|M|^2 = \frac{1}{1 + \Omega^{2N}} \quad (2\text{-}5\text{-}23)$$

$$N = \frac{\log_{10}\left(\frac{1}{M^2} - 1\right)}{2\log_{10}\Omega} \quad (2\text{-}5\text{-}24)$$

At the pass band frequency $F_p = 0.8$, the gain is *M* = -0.5 dB = 0.944. At the stop band frequency $F_s = 2.0$, the gain is *M* = -40 dB = 0.01. Inserting these in expression 2-5-23, we find orders *N1*, *N2:*

$$N_1 = \frac{\log_{10}\left(\frac{1}{0.944^2} - 1\right)}{2\log_{10} 0.8} = 4.7 \quad (2\text{-}5\text{-}25)$$

$$N_2 = \frac{\log_{10}\left(\frac{1}{0.01^2} - 1\right)}{2\log_{10} 2.0} = 6.6 \quad (2\text{-}5\text{-}26)$$

N should be the maximum next integer of N_1, N_2, which is 7.

4. The fourth step is to find the transfer function of the filter.

In the previous step, the order of the frequency response is found to be 7, and the squared magnitude frequency response can be expressed as:

$$|H(j\Omega)|^2 = \frac{1}{1 + \Omega^{14}} \quad (2\text{-}5\text{-}27)$$

It is possible to link $H(s)$ with $|H(j\Omega)|^2$. If we use the following form:

$$|H(j\Omega)|^2 = H(j\Omega) * H(j\Omega)^* = H(j\Omega) * H(-j\Omega) \quad (2\text{-}5\text{-}28)$$

and with $s = j\Omega$, we have:

$$|H(j\Omega)|^2 = H(s) * H(-s) \quad (2\text{-}5\text{-}29)$$

If $H(s)$ is expressed as the product of L zeros and N poles:

$$H(s) = \frac{k(s - z_1)(s - z_2) \dots (s - z_L)}{(s - p_1)(s - p_2) \dots (s - p_N)} \quad (2\text{-}5\text{-}30)$$

$H(-s)$ will have the symmetrical zeros and poles of $H(s)$, mirrored relative to Im{s}:

$$H(-s) = \frac{k(-s - z_1)(-s - z_2) \dots (-s - z_L)}{(-s - p_1)(-s - p_2) \dots (-s - p_N)} \quad (2\text{-}5\text{-}31)$$

Therefore $H(s) * H(-s)$ has $2L$ zeros and $2N$ poles. But which poles and zeros should belong to $H(s)$, and which should belong to $H(-s)$? From the theory of stable systems, all poles of causal stable systems must be in the Open Left Hand Plane (OLHP) but the zeros can be anywhere for such systems. Without a doubt, all the poles in OLHP are the ones from $H(s)$, and the others in the ORHP belong to $H(-s)$.

But, how to choose zeros? Can zeros be arbitrarily chosen? For a given magnitude response, yes they could. If only zeros in the OLHP are chosen for $H(s)$, the system will have minimum phase [48]. In our case, Butterworth filters have no zeros by definition, and $H(s)$ is found as:

$$H(s) = \frac{1}{1 + 4.4940s + 10.0978s^2 + 14.5918s^3 + 14.5918s^4 + 10.0978s^5 + 4.4940s^6 + s^7} \quad (2\text{-}5\text{-}32)$$

But this is the normalized transfer function. The unnormalized transfer function should be:

$$H\left(\frac{s}{\omega_c}\right) = \frac{1}{1 + 4.49\left(\frac{s}{\omega_c}\right) + 10.1\left(\frac{s}{\omega_c}\right)^2 + 14.6\left(\frac{s}{\omega_c}\right)^3 + 14.6\left(\frac{s}{\omega_c}\right)^4 + 10.1\left(\frac{s}{\omega_c}\right)^5 + 4.49\left(\frac{s}{\omega_c}\right)^6 + \left(\frac{s}{\omega_c}\right)^7}$$

(2-5-33)

where ω_c is 100Hz.

$$h(s) = \frac{10^{14}}{10^{14} + 4.49E12s + 10.1E10s^2 + 14.6E8s^3 + 14.6E6s^4 + 10.1E4s^5 + 4.49E2s^6 + s^7}$$

(2-5-34)

5. Cascaded expression of the transfer function

In practice, we rarely design a filter from a high order transfer function directly, but instead from a cascade of 1st order and/or 2nd order sections.

The denominator of the normalized transfer function in expression 2-5-32 is:

$$Den = 1 + 4.4940s + 10.0978s^2 + 14.5918s^3 + 14.5918s^4 + 10.0978s^5 + 4.4940s^6 + s^7$$

(2-5-35)

Considering pairs of complex conjugate poles, this can be written as:

$$Den = (s - p_0)(s - p_1)(s - p_1^*)(s - p_2)(s - p_2^*)(s - p_3)(s - p_3^*) \quad (2\text{-}5\text{-}36)$$

where

$p_0 = -1;\ p_1 = -0.2225 + 0.9749i;\ p_2 = -0.6233 + 0.7820i;\ p_3 = -0.9011 + 0.4335i;$

Let

$$Den1 = (s - p_0) = s + 1 \quad (2\text{-}5\text{-}37)$$

$$Den2 = (s - p_1)(s - p_1^*) = s^2 + 0.4451s + 1 \quad (2\text{-}5\text{-}38)$$

$$Den3 = (s - p_2)(s - p_2^*) = s^2 + 1.2466s + 1 \quad (2\text{-}5\text{-}39)$$

$$Den4 = (s - p_3)(s - p_3^*) = s^2 + 1.8023s + 1 \quad (2\text{-}5\text{-}40)$$

Then we have:

$$H(s) = \frac{1}{s+1} \times \frac{1}{s^2 + 0.445s + 1} \times \frac{1}{s^2 + 1.247s + 1} \times \frac{1}{s^2 + 1.802s + 1} \quad (2\text{-}5\text{-}41)$$

Finally the cascaded normalized transfer function with 1st order and 2nd order sections is found from 2-5-41, and it is the schematic source for the circuits of the low-pass filter design.

6. Circuit topology to implement the transfer function (TF)

In the last section, the cascaded normalized transfer function form is found in expression 2-5-41, with a 1st order and three 2nd order TFs. In this section, special circuits are designed to implement the low-order TFs.

Let's consider the first-order TF, the first term in 2-5-41. The following is a simple first order low-pass filter topology to realize the TF.

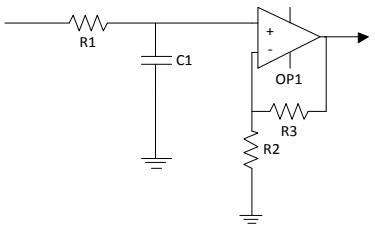

Figure 2.5-8 First-order Low-Pass Filter Design (15)

By using operational amplifier fundamental theory, it can be found that the circuit transfer function is:

$$h_1(s) = \frac{1 + \frac{R_3}{R_2}}{1 + R_1 C_1 s} \quad (2\text{-}5\text{-}42)$$

If R_2 is far greater than R_3, then $h_1(s)$ can be simplified as:

$$h_1(s) = \frac{1}{1 + R_1 C_1 s} \quad (2\text{-}5\text{-}43)$$

But $h_1(s)$ is unnormalized. To normalize $h_1(s)$, we set $s' = \frac{s}{\omega_c}$, then $s = \omega_c s'$,

$$H_1(s') = \frac{1}{1 + \omega_c R_1 C_1 s'} \quad (2\text{-}5\text{-}44)$$

where ω_c is the cut-off frequency, which is $2\pi \times 100$ Hz in our case.

By comparing 2-5-44 with the first term in 2-5-41, we have $\omega_c R_1 C_1$ =1. We select $R_1 = 10\ k\Omega$, and $C_1 = 1\ \mu F$.

Of course, there is not only one circuit topology possible to realize the 1st order TF, but their design methods are similar.

To realize the 2nd order low-pass TF, there are two main topologies commonly used, the Sallen-Key and the Multiple Feedback (MFB). Let's focus on the unit gain Sallen-Key.

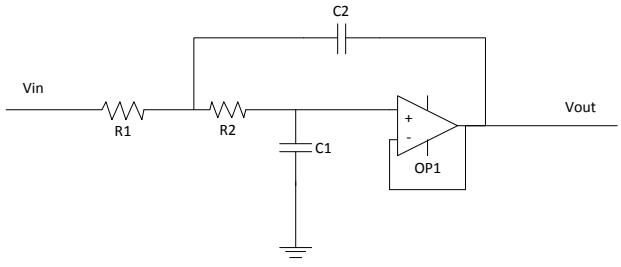

Figure 2.5-9 Second-order low-pass filter (16)

The transfer function of the Figure 2.5-9 can be written as:

$$H_2(s) = \frac{1}{1 + (R_1+R_2)C_1 s + R_1 R_2 C_1 C_2 s^2} \quad (2\text{-}5\text{-}45)$$

The normalized expression will be:

$$H_2(s) = \frac{1}{1 + \omega_c(R_1+R_2)C_1 s + \omega_c^2 R_1 R_2 C_1 C_2 s^2} \quad (2\text{-}5\text{-}46)$$

By comparing 2-5-46 with the second term of 2-5-41, the following expression must be satisfied.

$$\omega_c(R_1+R_2)C_1 = 0.445, \omega_c^2 R_1 R_2 C_1 C_2 = 1 \quad (2\text{-}5\text{-}47)$$

We select $R_1 = R2 = 100\ k\Omega, C_1 = 22.3\ nF, C_2 = \ 0.448\ \mu F$

The same approach is applied for the other terms. It is found that the third term and fourth term parameters are:

$$\omega_c(R_1+R_2)C_1 = 1.247, \omega_c^2 R_1 R_2 C_1 C_2 = 1 \quad (2\text{-}5\text{-}48)$$

where we select: $R_1 = R2 = 100\ k\Omega, C_1 = 62.5\ nF, C_2 = \ 0.160\ \mu F$

$$\omega_c(R_1+R_2)C_1 = 1.802, \omega_c^2 R_1 R_2 C_1 C_2 = 1 \quad (2\text{-}5\text{-}49)$$

where we select: $R_1 = R2 = 100\ k\Omega, C_1 = 90.3\ nF, C_2 = \ 0.111\ \mu F$

Of course there are again many solutions to realize the same transfer function, but the resistance and capacitance values should remain in the range of commonly available components.

We can also note that with the filter design CAD software such as FilterPro of Texas Instrument, the design of the analog filter can completed in a few minutes.

2.5.5 Post-Amplifiers

The signal after the processing with the low-pass filter is still very weak, and it is necessary to boost the signal strength at this stage, before it can be sampled by an A/D device for further processing in the digital domain.

The amplifier gain is required to be 60 dB minimum, boosting the signal from the mV range to the V range. The signal bandwidth is within 100 Hz, and the DC component should also be filtered out during the amplification.

The design is realized by two stages of inverting amplifiers:

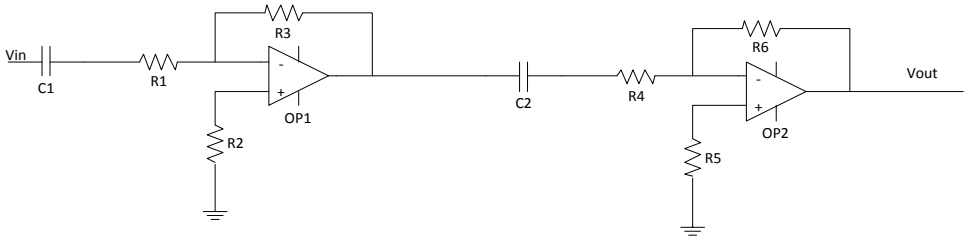

Figure 2.5-10 Two stage inverter amplifier (17)

Let $C_1 = C_2 = 100\ \mu F,\ R_1 = R_4 = 3\ k\Omega, R_3 = R_6 = 100\ k\Omega, R_2 = R_5 = 3\ k\Omega$

The gain in the first stage will be:

$$G1 = -\frac{R_3}{R_1} = -33 \quad (2\text{-}5\text{-}50)$$

$$G2 = -\frac{R_6}{R_4} = -33 \quad (2\text{-}5\text{-}51)$$

$$G = G1 \times G2 = 1089 = 60.7\text{dB} \quad (2\text{-}5\text{-}52)$$

C_1 and C_2 are also filtering the DC component as well.

2.6 Conclusion

The prototype ODM sensor built for our experiments consists of two sensor units, each containing three coils i.e., two field coils and one sense coil. For each sensor unit, an independent electronic circuit is used to process the particle modulated signal. Those two electronic units are theoretically identical. The purpose of the electronic circuit is to detect the particle signal in both sensor units and to prepare the signal for further digital processing afterwards.

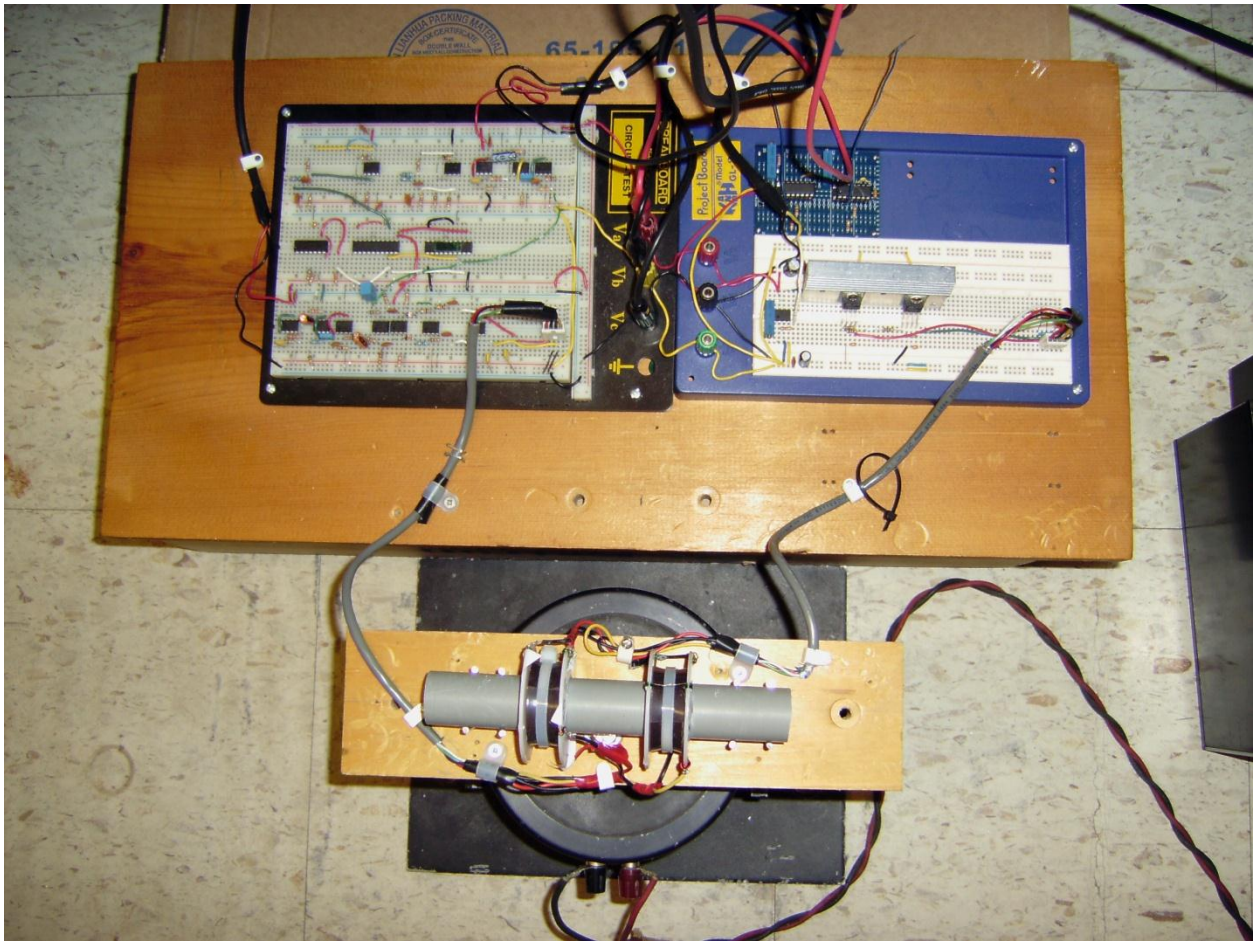

Figure 2.6-1 ODM system prototype (18)

Chapter 3 The Angle of Arrival Algorithm

3.1 Introduction

The Angle of Arrival (AOA) algorithm [49] is a method originally proposed to determine the direction of wireless radio propagation. It has been applied in radar, sonar, and wireless communications. Though AOA is a well-known technique and has been thoroughly described in the open literature [24, 25], there is no report on AOA application to ODM signal analysis in the literature. In fact, AOA can be revised and improved to detect a particle signal mixed with a vibration signal. This chapter will clarify the theory of the algorithm and present the experimental results to show how to solve the ODM random vibration problem.

3.2 Signals from the Prototype

After the prototype has been built, the particle signal can be displayed on an oscilloscope, and in our experiments it was be sampled by a National Instruments© (NI) Data Acquisition (DAQ) box. With the prototype, the particle signal displayed is in pairs corresponding to the two channels, which is different from the previous single-channel signal of the Gastop Metalscan sensor.

The characters of the signals from the prototype in a static state as shown in Figure 3.1-1 are as follows:

1. The particle signature is similar to a one-period sinusoidal signal.
2. The signatures in both channels are different. Comparing to the particle signature in the top part of Figure 3.1-1, the bottom one has an opposite phase with a time delay. It can be described as a “phase delay” between the two particle signals.
3. The background noise signal in one channel drifts irregularly in a small scale. The noises in the two channels are closely correlated. Because of this, the background noise can be filtered out.
4. The two channels have different voltage gains, and the signals have different amplitudes.

5. Since the background noises in the two channels are correlated, they are not thermal noises from the electrical circuits. They come from a common source, which is the carrier signal from the field coils, driven by the output of the signal generator. When the carrier signal is drifting irregularly, the circuits will amplify it and show such correlated background noises.

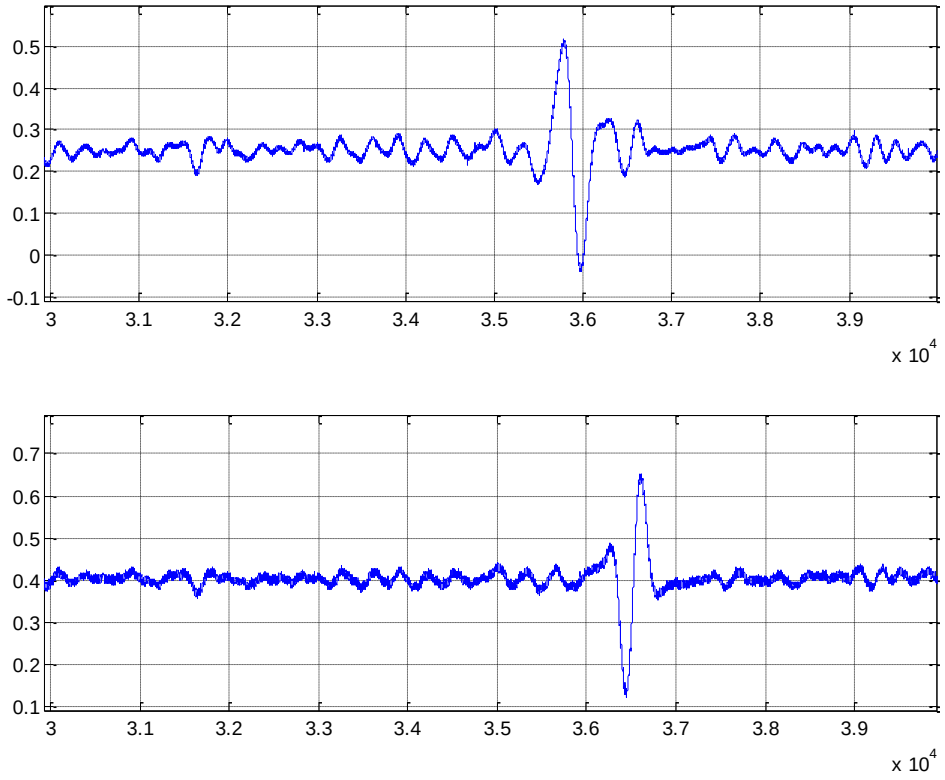

Figure 3.1-1 A ferrous particle (500μm) signal in static state (19)

When the prototype device is shaken by an external force of random vibrations, the particle signal is mixed with the vibration signals. Those vibration signals may not be continuous, and they cannot be predicted. Consider the mixture of vibration and a particle signal as shown Figure 3.1-2.

If only one channel signal is observed, it is difficult to distinguish a particle signal from the vibration signals. However, by comparing the phases of the signals in both channels, it can be found that:

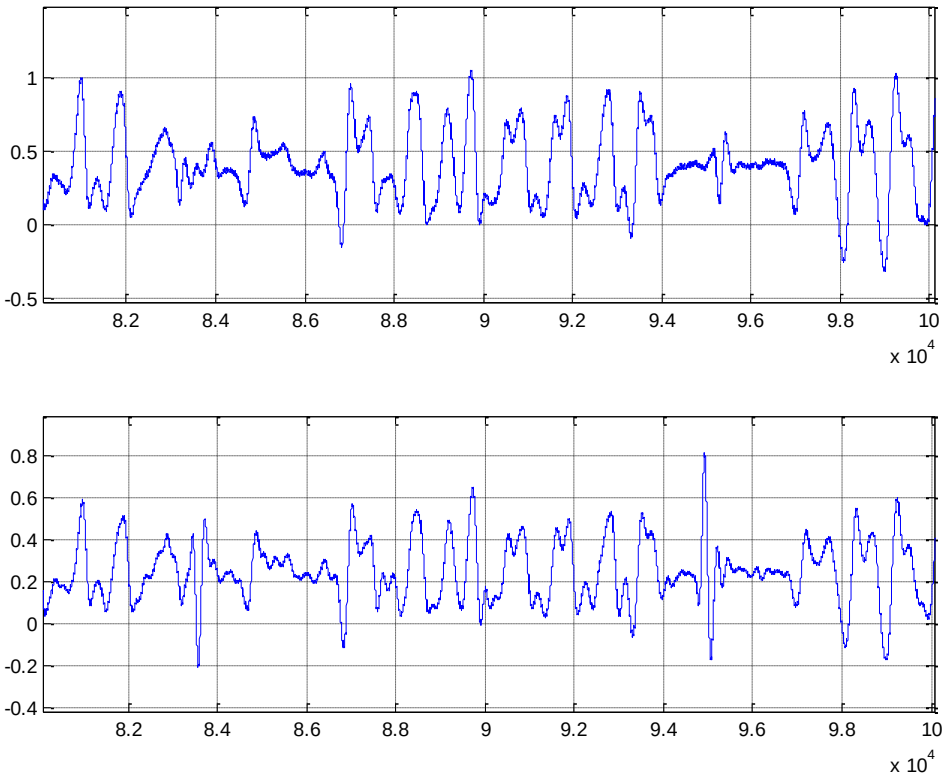

Figure 3.1-2 A ferrous particle (500μm) signal in vibration state (20)

1. Vibration signals in both channels are similar. They have the same frequency and phase, but different amplitudes.
2. Particle signals in both channels look like sinusoidal signals. One is roughly a delayed version of the other.

In summary, the vibration signals have the same frequency and phase, but particle signals have a phase delay. According to this character, an AOA algorithm is proposed to provide an effective method to indicate a particle signal in the presence of interfering vibrations.

3.3 Basic Theory of AOA

Generally the AOA algorithm is designed to measure the phase difference at each element of several sensors, no matter whether those sensors are in an array or in random locations, and no matter whether the phase difference is caused by RF wave propagation or by metal particle signal. The objective of an AOA algorithm is to find the optimal phase difference between two sensor elements under a specific frequency.

3.3.1 The Model of AOA

Consider a simple sensor array with two elements.

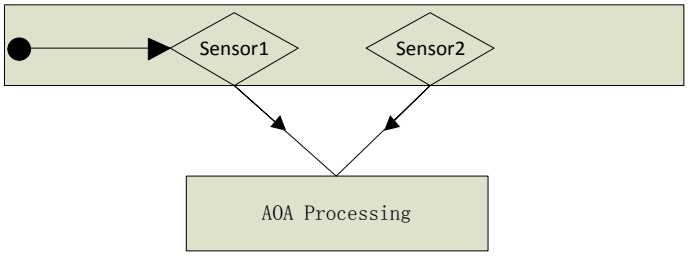

Figure 3.3-1 Structure of AOA processing (21)

Suppose that sensor 1 and sensor 2 are two elements ready to detect a particle signal at the same time. The received signal at each element can be expressed as:

$$x_i(t) = x(t - \tau_i) \qquad i = 1,2 \tag{3-3-1}$$

As different signal receivers have different signal sensitivity, their voltage gains may not be identical, then expression 3-3-1 can be revised as

$$x_i(t) = a_i x(t - \tau_i) \qquad i = 1,2 \tag{3-3-2}$$

where the element amplitude gain a_i is constant depending on the elements nature, and does not change with time.

According to the Fourier Transform (FT) theory, each snapshot (i.e., window) of signal duration is composed of an infinite number of continuous frequency components:

$$x(t) = \int_{-\pi}^{\pi} A(\omega) e^{j\omega t} d\omega \qquad (3\text{-}3\text{-}3)$$

where $A(\omega)$ is a complex number with amplitude and phase. Note that when FFT components are used to approximate the FT in practice, each frequency is discrete and corresponds to a sampling of the FT of the signal.

Suppose that ω_c is an arbitrary frequency in the frequency domain. The ω_c component of the source signal is $x(\omega_c, t) = A(\omega_c)e^{j\omega_c t}$, and then 3-3-2 can be expressed as

$$x_i(\omega_c, t) = a_i A(\omega_c) e^{j\omega_c t} e^{-j\omega_c \tau_i} \qquad i = 1,2 \qquad (3\text{-}3\text{-}4)$$

and furthermore, it can be expressed as:

$$x_i(\omega_c, t) = a_i x(\omega_c, t)\, e^{-j\omega_c \tau_i} \qquad i = 1,2 \qquad (3\text{-}3\text{-}5)$$

Denoting $\phi_i = \omega_c \tau_i$ the phase delay introduced by the time delay for some specific frequency, 3-3-5 becomes

$$x_i(\omega_c, t) = a_i x(\omega_c, t)\, e^{-j\phi_i} \qquad i = 1,2 \qquad (3\text{-}3\text{-}6)$$

In the following discussions, ω_c will be omitted because the developments are valid for any frequency ω_c . Equation 3-3-6 can also be expressed in vector expression:

$$\boldsymbol{x}(t) = x(t)\boldsymbol{A}\boldsymbol{v}(\boldsymbol{\phi}) \qquad (3\text{-}3\text{-}7)$$

where $x(t)$ is $x(\omega_c, t)$, $\boldsymbol{A} = \begin{bmatrix} a_1 & 0 \\ 0 & a_2 \end{bmatrix}$, $\boldsymbol{v}(\boldsymbol{\phi}) = \begin{bmatrix} e^{-j\phi_1} \\ e^{-j\phi_2} \end{bmatrix}$.

Usually ϕ_1 is the reference phase, and it can be arbitrarily set to any value. Here we choose $\phi_1 = 0$, and define $\phi = \phi_2 - \phi_1$. Then we have $\boldsymbol{v}(\boldsymbol{\phi}) = \begin{bmatrix} 1 \\ e^{-j\phi} \end{bmatrix}$.

Equation 3-3-7 is important because it reveals that a signal depends on three multiplicative factors, namely, the common source signal $x(t)$, the voltage gain of the receiver $\boldsymbol{A}$, and the

manifold vector $\boldsymbol{v}(\boldsymbol{\phi})$, in product form. It should be noted that expression 3-3-7 is only for a specific frequency component. The manifold vector $\boldsymbol{v}(\boldsymbol{\phi})$ is dependent on the frequency.

For a specific frequency component, the manifold vector $\boldsymbol{v}(\boldsymbol{\phi})$ is no longer a function of time. It thus has nothing to do with the source signal or its statistics, but it is dependent on whatever causes a phase difference at each sensor elements, e.g., the positions of the sensors and the speed of the particles flowing through the sensors. The manifold vector $\boldsymbol{v}(\boldsymbol{\phi})$ is important because it will be used to distinguish the particle signal and the vibration signal from the phase delay they contain.

3.3.2 Correlation Matrix

In order to estimate the manifold vector, the first thing is to estimate the correlation matrix in the power spectrum domain. When the expression 3-3-7 is transformed to the frequency domain, we obtain

$$\boldsymbol{x}(\omega) = x(\omega)\boldsymbol{A}\boldsymbol{v}(\boldsymbol{\phi}) \tag{3-3-8}$$

As stated before, ω can be omitted if we consider only a specific frequency component. Hence 3-3-8 reduces to

$$\boldsymbol{x} = x\boldsymbol{A}\boldsymbol{v}(\boldsymbol{\phi}) \tag{3-3-9}$$

Accordingly, the correlation matrix in the frequency domain is

$$\boldsymbol{S} = E[\,\boldsymbol{x}\boldsymbol{x}^{+}] = E[x\boldsymbol{A}\boldsymbol{v}(\boldsymbol{\phi})\big(x\boldsymbol{A}\boldsymbol{v}(\boldsymbol{\phi})\big)^{+}] \tag{3-3-10}$$

For simplicity, we replace $\boldsymbol{v}(\boldsymbol{\phi})$by $\boldsymbol{v}$ and obtain:

$$\boldsymbol{S} = E[xx^{+}]\boldsymbol{A}\boldsymbol{v}\boldsymbol{v}^{+}\boldsymbol{A}^{+} \tag{3-3-11}$$

In practice, $\boldsymbol{S}$ is estimated from the incoming signal $\boldsymbol{x}$. If there is a sequence of input vectors $\boldsymbol{x_1}, \boldsymbol{x_2}, \ldots, \boldsymbol{x_k}$, from 1 to *K*, then the following estimate is obtained

$$\widehat{\boldsymbol{S}}_{\boldsymbol{x}} = \frac{1}{K}\sum_{i=1}^{K} \boldsymbol{x_i}\boldsymbol{x_i}^{+} \qquad (3\text{-}3\text{-}12)$$

The following should be noted:

1. $\boldsymbol{x_i}$ is a complex vector in the frequency domain at a specific frequency, coming from one of the *K* snapshots of the incoming signal.
2. $\widehat{\boldsymbol{S}}_{\boldsymbol{x}}$ is the correlation matrix estimation for a specific frequency based on *K* snapshots of the incoming signal.
3. If $\boldsymbol{x_i}$ is from an iid (independent and identically distributed) complex Gaussian vector process, $\widehat{\boldsymbol{S}}_{\boldsymbol{x}}$ is the optimal estimation of $\boldsymbol{S}$ in the ML (Maximal Likelihood) sense. Even if $\boldsymbol{x_i}$ is not iid, it can still be a good estimation of $\boldsymbol{S}$ when *K* is large enough.

Once the correlation matrix has been obtained, the next task is to scan the beam power.

3.3.3 Power Scanning

After receiving the sensor signal, the output signal is the sum of the products of the received signal and the controlled complex coefficients in the frequency domain, i.e.

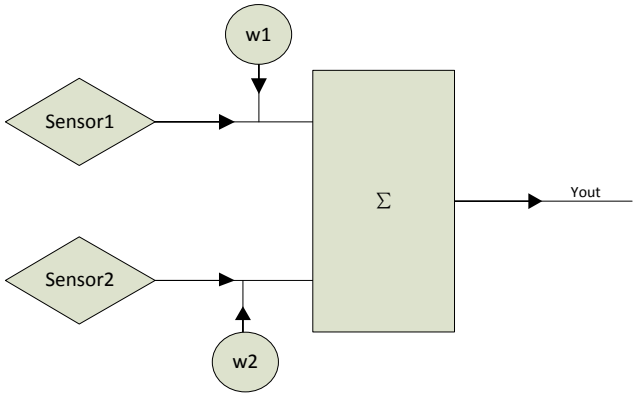

Figure 3.3-1 The subsystem structure of AOA Processing (22)

$$Y_{out} = \boldsymbol{w}^{+}\boldsymbol{x} \tag{3-3-13}$$

The output power will be:

$$P_{out} = |\boldsymbol{w}^{+}\boldsymbol{x}|^{2} = \boldsymbol{w}^{+}\boldsymbol{x}\boldsymbol{x}^{+}\boldsymbol{w} = \boldsymbol{w}^{+}\boldsymbol{S}\boldsymbol{w} \tag{3-3-14}$$

Select $\boldsymbol{w} = \begin{bmatrix} 1 \\ e^{-j\psi} \end{bmatrix}$, the phase scanning vector, where ψ is the scanning phase.

$$P_{out} = xx^{+}\boldsymbol{w}^{+}\boldsymbol{A}\boldsymbol{v}\boldsymbol{v}^{+}\boldsymbol{A}^{+}\boldsymbol{w} \tag{3-3-15}$$

Substituting $\boldsymbol{w}, \boldsymbol{A},$ and $\boldsymbol{v}$ with their expanded forms gives

$$P_{out} = E[xx^{+}]\begin{bmatrix} 1 \\ e^{-j\psi} \end{bmatrix}^{+}\begin{bmatrix} a_1 & 0 \\ 0 & a_2 \end{bmatrix}\begin{bmatrix} 1 \\ e^{-j\phi} \end{bmatrix}\begin{bmatrix} 1 \\ e^{-j\phi} \end{bmatrix}^{+}\begin{bmatrix} a_1 & 0 \\ 0 & a_2 \end{bmatrix}^{+}\begin{bmatrix} 1 \\ e^{-j\psi} \end{bmatrix} \tag{3-3-16}$$

The P_{out} can be simplified as:

$$P_{out} = E[xx^{+}](a_1^2 + a_2^2 + 2a_1a_2\cos(\psi - \phi)) \tag{3-3-17}$$

where a_1, a_2 are positive voltage gains.

When the scanning phase $\psi = \phi, P_{out}$ is maximal, or alternatively, when P_{out} is maximal, the scanning phase ψ is the optimal estimation of the phase ϕ.

Once the phase difference has been determined for each frequency, the particle signal or vibration signal can be estimated. When the phase difference is zero, it is a vibration; otherwise it is a particle signal.

3.4 Algorithm Implementation

The AOA algorithm implementation procedure is as follows:

1. Sample the sensor signals with appropriate sampling frequency and convert the signal from the analog domain to the digital domain.
2. Select an appropriate snapshot window size and a shifting step. The snapshot window should cover the length of the particle signal. In our case, by observation, the particle signal is about 0.2-0.4 second long depending on the particle speed. With 1 kHz sampling rate, the window hence contains 500 samples, which is 0.5 second. The shifting step is

half of the window, i.e., 250 samples. If the shifting step is too small, the process will require a significant computational power, and it will generate too much redundant data. But if the shifting step is too large, the frequency components at the window boundary may be missed. Half of the window size is a reasonable choice for the shifting step.

3. For each snapshot, convert the signal from the time domain to the frequency domain by a Fourier Transform (approximated by a FFT).
4. For each frequency, calculate the correlation matrix *S* from the received signals of both channels.
5. For each frequency, find the phase and the maximal power.
6. Move to the next snapshot, and repeat steps 3 to 5 until the snapshots are all exhausted.
7. Generate a table with frequency, phase and maximal power. Plot it in a 2-D plane with power and angle relationship.

3.5 Experimental Result Analysis

Several typical scenarios are analyzed with the algorithm AOA as listed below. The results show that background noise, vibration and particle signals all have distinctive characters in the diagram of power-phase. Particle signals can be recognized by this method.

Scenario 1: Background Noise as shown in the Figure 3.5-1

As stated before, background noise in both channels are closely correlated as the result of a common carrier signal drifting. Due to the different nature of each sensor, in this example the upper signal is much noisier than the lower one. Furthermore the average voltage gain of each channel is different, but both signals are in coherence.

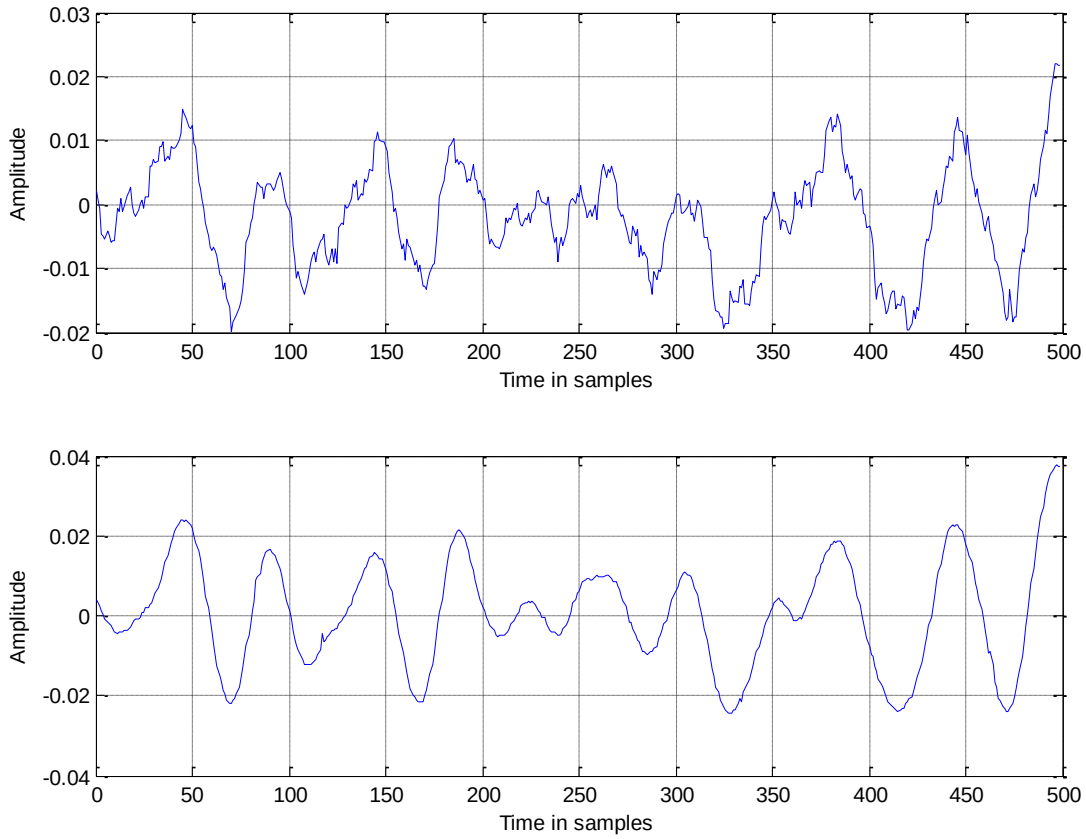

Figure 3.5-1 The background noise in both channels (23)

The following Figure 3.5-2 shows the relationship among power, phase and frequency generated by the AOA algorithm.

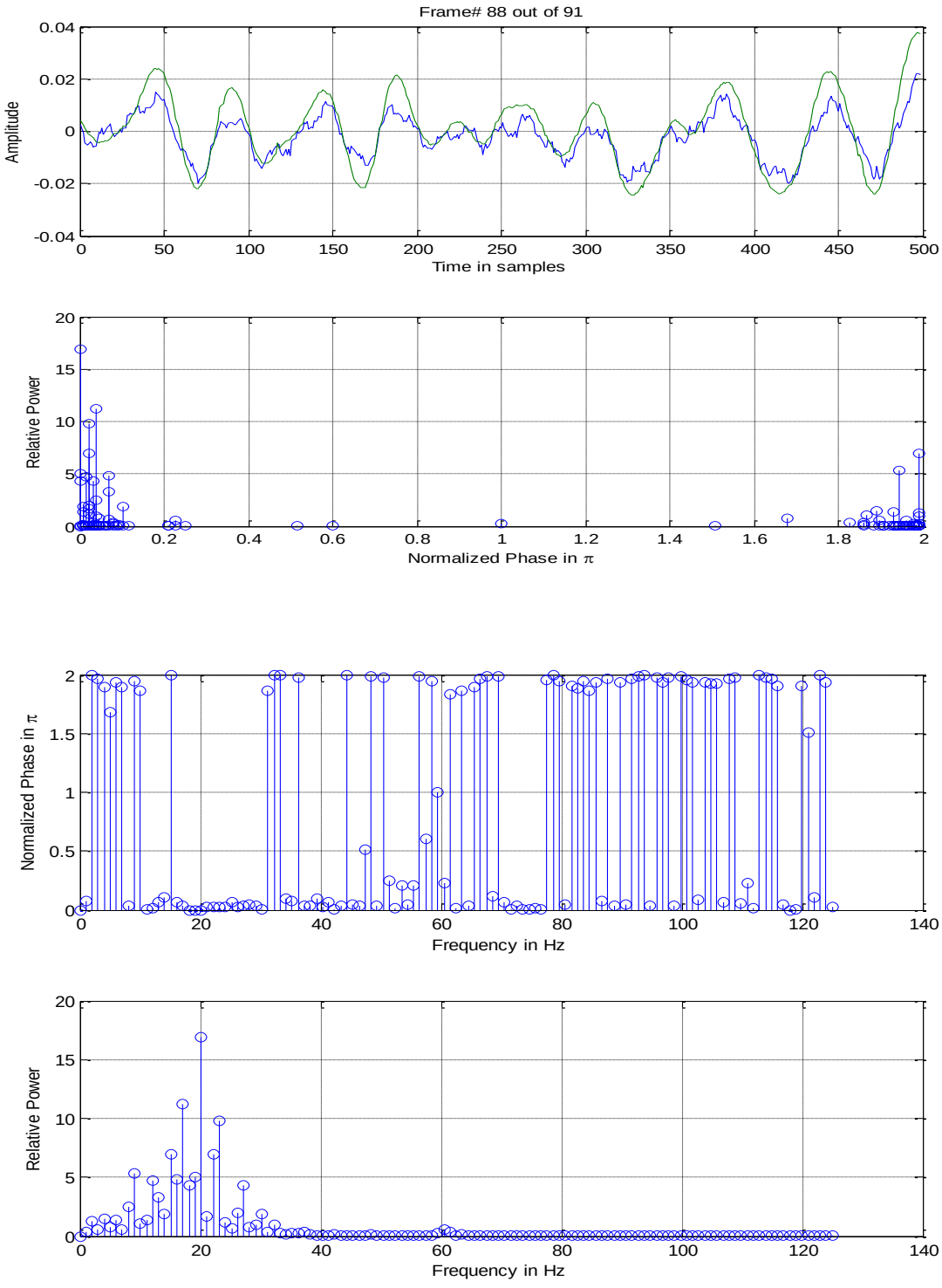

Figure 3.5-2 Power, frequency and phase relationship (24)

Some observations for this scenario:

1. The background noise has small energy in the time domain; the average voltage amplitude is about 0.02V
2. Most energy is concentrated around the phase 0 or 2π in the second picture of Figure 3.5-2. It means that the two channel signals are basically coherent.
3. The highest energy is at 20Hz, the fundamental frequency.

In summary, the characteristic of the background noise is that the frequency components with large power are distributed around 0 or 2π phase.

Scenario 2: The particle signal

Figure 3.5-3 shows the result of the AOA algorithm for a particle signal. The particle trace can be captured by the AOA diagram. From the figure, the following can be observed:

1. In the second picture, the energy stems are no longer concentrated around the phase zero or 2π, but distributed at all angles.

2. In the fourth picture, the area from 0 to 20 Hz is the energy concentration zone.

3. In the third picture, there is a linear phase between 5Hz to 18Hz, occupying 4π phase.

The group delay time can be calculated from this as:

$$\tau = \frac{\phi}{\omega} = \frac{4\pi}{2\pi \times (18-5)Hz} = 0.154s \qquad (3\text{-}3\text{-}17)$$

4. From the first picture, the particle signal delay time between the two channels is estimated as 150 ms = 0.150s, which is quite close to the result from 3-3-17.

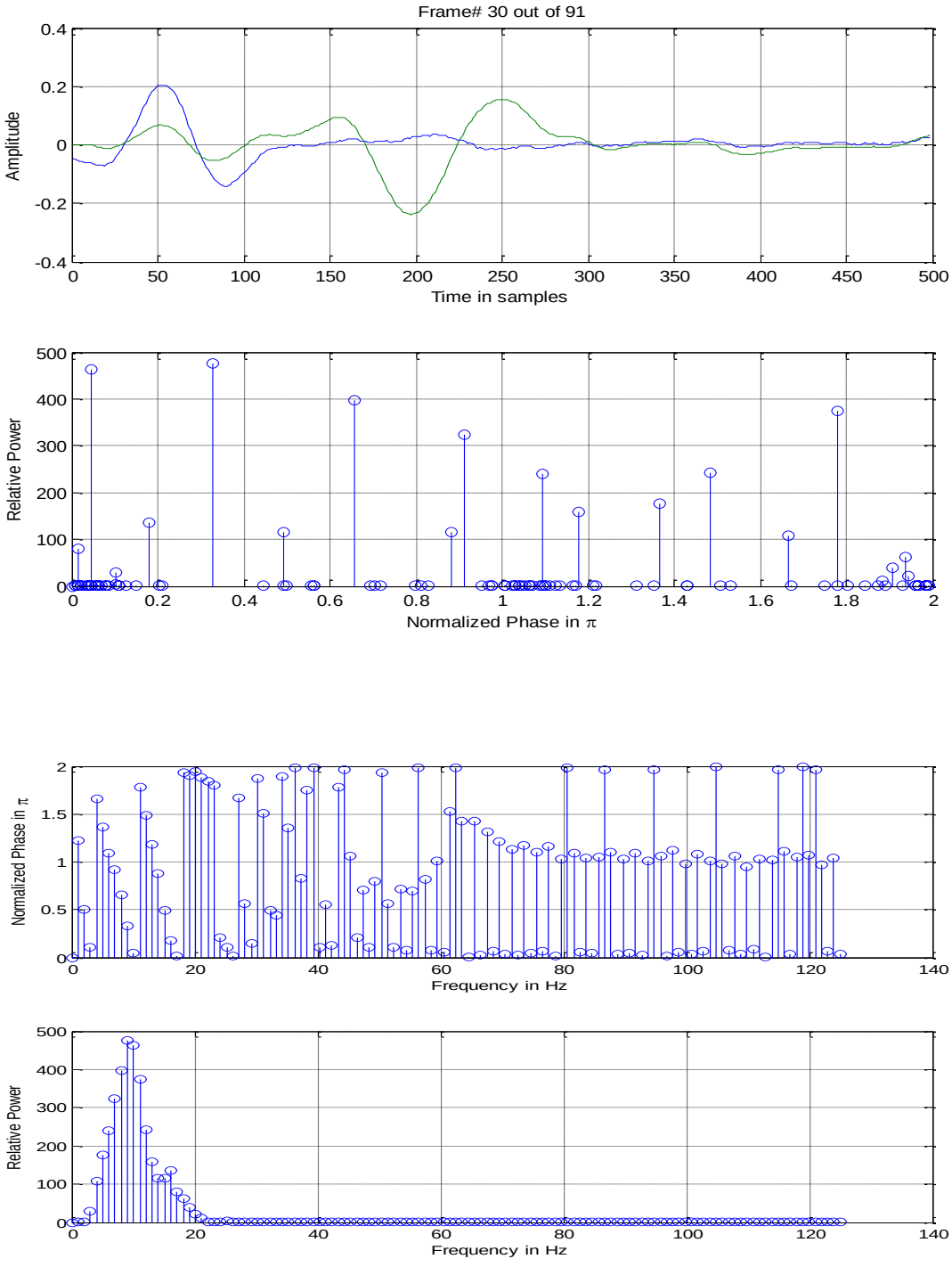

Figure 3.5-3 Power, Frequency and Phase relationship of a particle signal (25)

Scenario 3: The vibration signal

The vibration signal observed here, as shown in the first picture of Figure 3.5-4, is roughly periodic and coherent between channels, similar to the background noise signal. However its strength is much higher, over 10 times that of the background noise. The AOA results show that the phase is around zero or 2π.

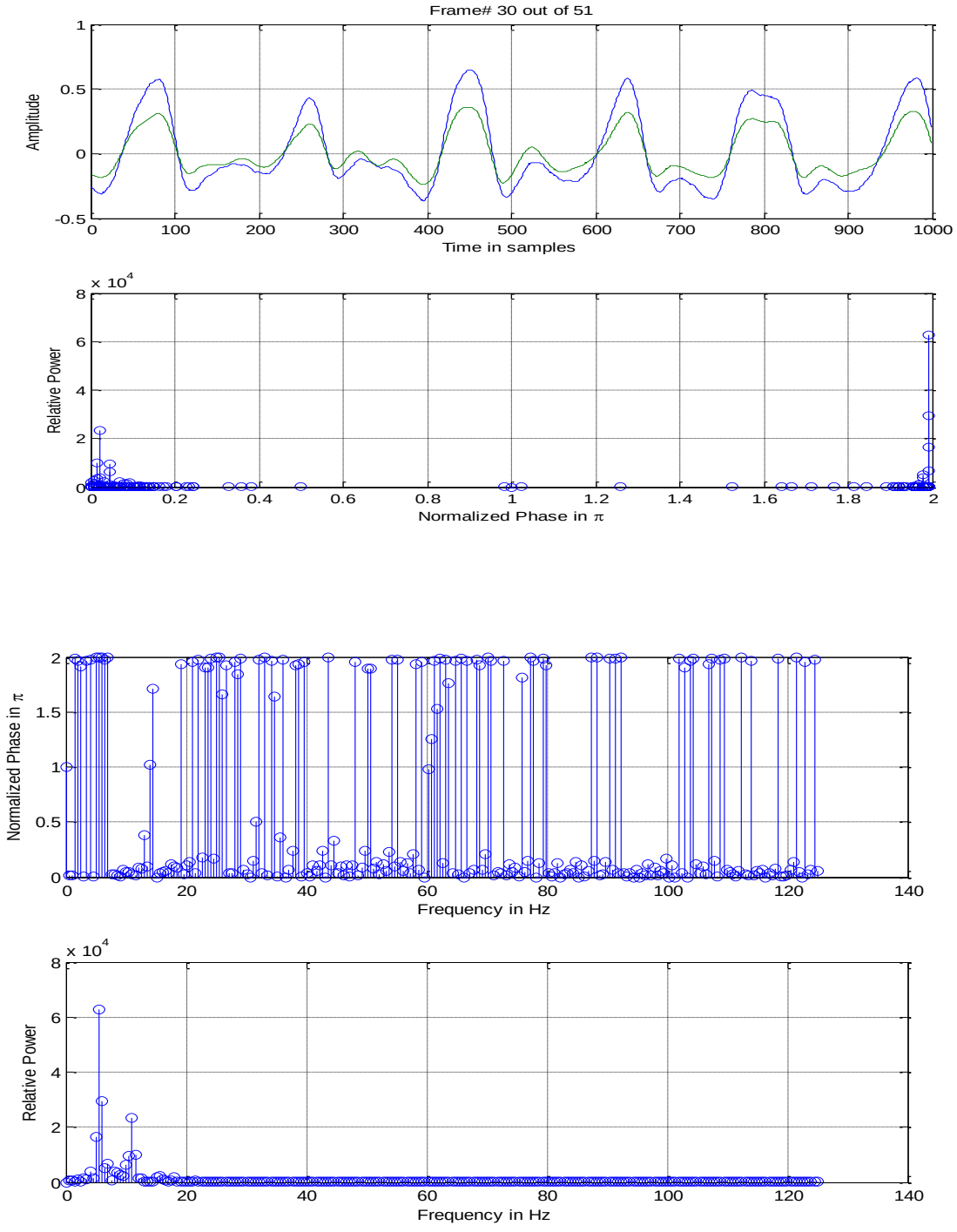

Figure 3.5-4 Power, Frequency and Phase relationship of a vibration signal (26)

Scenario 4: The mixed vibration and particle signals

As shown in Figure 3.5-5, when the vibration and particle signals are mixed, the phase is no longer around 0 (or 2π), but it is distributed everywhere. The characters of the signal in Figure 3.5-5 are analyzed as follows:

1. In the fourth picture of the figure, the region between 0 and 20 Hz contains most of the energy. The energy in other areas is almost zero.

2. From 2 to 8 Hz, the phase is around 0. There exists a linear phase from 8 to 20 Hz. The delay is obtained by:

$$\tau = \frac{\phi}{\omega} = \frac{(2-1)\pi}{2\pi \times (20-8)Hz} = 0.042s \qquad (3\text{-}3\text{-}17)$$

However the original signal in the first picture shows that the delay is about 0.080s. There is thus a large error in the case of a mixture of particle and vibration signals. To address this, other methods are developed in the next chapters.

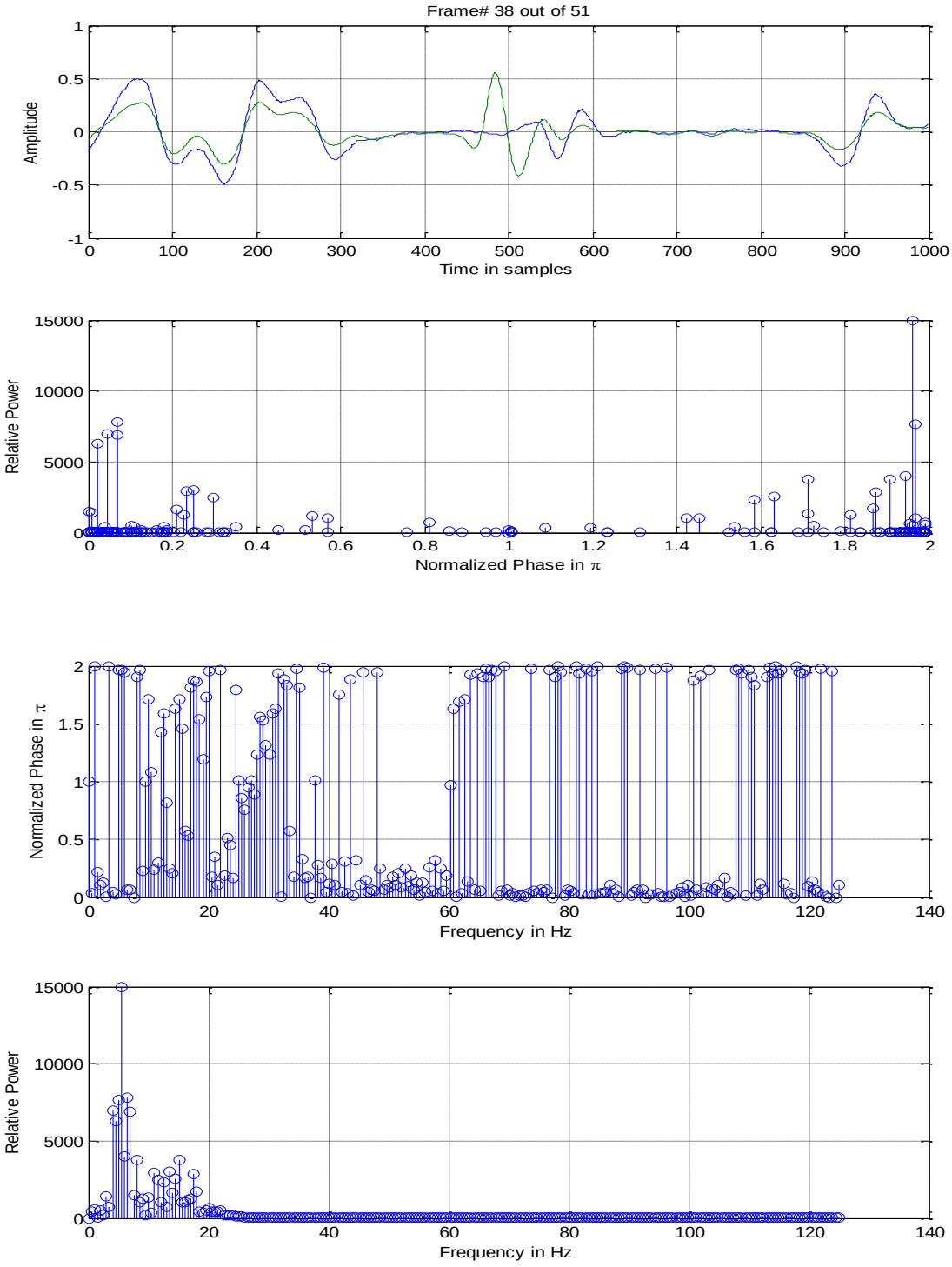

Figure 3.5-5 Power, frequency and phase relationship of mixed vibration and particle signals (27)

3.6 Conclusion

A single signal from one sensor is not sufficient for phase comparisons. Multiple signals from multiple sensors are required to compare the phases for different frequency components. An AOA algorithm has been developed to measure the phase and the power for different frequency components. The obtained phase information can be used to distinguish a particle signal from a vibration signal and background noise. However a difficult case for the AOA algorithm to deal with is when a particle signal is simultaneously present with a vibration signal of similar amplitude. Therefore, alternative methods need to be developed in the next chapters.

Chapter 4 TDOA Algorithm

4.1 Introduction

In the previous chapter, the algorithm AOA was proposed as an effective method in measuring the phase difference between two channel signals. However, it suffers from inaccuracy in measuring the time delay of the particle signals when it is interfered by vibration signals. Even though measuring phase difference can indicate that a particle exists, time difference (time delay) measurement, on the other hand, is important to estimate how long it takes for a particle to pass through the two sensor units. The time difference of arrival (TDOA) [50] algorithm can be used for this purpose.

4.2 Cross Correlation

When a particle passes two sensor units, a time delay is brought about between the induced particle signals. When a vibration comes, the interfering signals between the two sensors are mostly coherent and without a time delay. This process can be modeled as:

$$x_1(t) = s(t) + s_I(t) + n_1 \quad (4\text{-}2\text{-}1)$$

$$x_2(t) = As(t - D) + Bs_I(t) + n_2 \quad (4\text{-}2\text{-}2)$$

where $s(t)$ is the particle signal, $s_I(t)$ is the interference signal, and n_1 and n_2 are Gaussian noises. The interference signal $s_I(t)$ in both channels are supposed to be in phase and without delay, while the particle signal in channel 2 has a relative delay *D*. The gain ratio of the circuits between the two channels is *A* for the particle component and *B* for the vibration component.

The cross correlation of $x_1(t)$ and $x_2(t)$ is defined as:

$$R_{x_1x_2}(\tau) = \int_{-\infty}^{\infty} x_1(t)x_2(t + \tau)dt \quad (4\text{-}2\text{-}3)$$

Substituting equations 4-2-1 and 4-2-2 into equation 4-2-3 leads to:

$$R_{x_1x_2}(\tau) = \int_{-\infty}^{\infty} (s(t) + s_I(t) + n_1)(As(t + \tau - D) + Bs_I(t + \tau) + n_2)dt \quad (4\text{-}2\text{-}4)$$

Suppose that the Gaussian noises are not correlated with each other, neither with the particle signal, nor with the vibration interference signal. The cross correlation will be simplified as:

$$R_{x_1x_2}(\tau) = \int_{-\infty}^{\infty} \big(s(t) + s_I(t)\big)(As(t + \tau - D) + Bs_I(t + \tau))dt \quad (4\text{-}2\text{-}5)$$

The auto-correlation is defined as:

$$R_s(\tau) = \int_{-\infty}^{\infty} s(t)s(t + \tau)dt \quad (4\text{-}2\text{-}6)$$

Further assuming that the particle signal and the vibration interference signal are not correlated, then equation 4-2-5 can be re-written as:

$$R_{x_1x_2}(\tau) = AR_s(\tau - D) + BR_{s_I}(\tau) \quad (4\text{-}2\text{-}7)$$

Let's consider the following situations:

Scenario 1: The particle signal is dominant; the interference signal is very small, i.e., $s(t) \gg s_I(t)$. Then expression 4-2-7 will be simplified:

$$R_{x_1x_2}(\tau) = AR_s(\tau - D) \quad (4\text{-}2\text{-}8)$$

According to the property of autocorrelation that for any delay τ, the continuous autocorrelation function reaches its highest peak at the origin [51]

$$R_s(0) \geq |R_s(\tau)| \quad (4\text{-}2\text{-}9)$$

then $|R_{x_1x_2}(\tau)|$ in equation 4-2-8 reaches maximum when $\tau - D = 0, \text{i.e.}\ \tau = D$. This is critical to finding the delay time of the particle signals.

Scenario 2: The interference signal is dominant; the particle signal is small.
In this case expression 4-2-7 will be simplified as:

$$R_{x_1x_2}(\tau) = BR_{s_I}(\tau) \quad (4\text{-}2\text{-}10)$$

In the cross correlation diagram $BR_{s_I}(\tau)$, many side lobes exist beside the main lobe $R_{s_I}(0)$, and since these sidelobes are often greater than the smaller particle correlation signal $AR_s(\tau - D)$, it makes the detection of the peak in $AR_s(\tau - D)$ often impossible in such cases. When this happens, the TDOA of the particle signal cannot be measured.

Scenario 3: No signal is dominant. The lobes of both signals $AR_s(\tau - D)$ and $BR_{s_I}(\tau)$ are mixed together in the cross correlation diagram. The measurement of the TDOA of the particle signal is sometimes possible in such cases, but it can be noisy and it is not always easy to detect.

4.3 Uni-directional TDOA Measurement.

4.3.1 Snapshot Window

The discussion of the last section suggests that it would be better to measure a particle TDOA when the particle signal is dominant. Such a condition can be created by segmenting the input signal, i.e., taking a small snapshot window and shifting the window forward over an interval of appropriate lags.

The advantage of taking a small snapshot window over taking the whole signal window is that the power ratio of the particle signal to the interfering signal can be increased. When the power ratio of the particle signal to the interfering signal in a snapshot window is higher, the particle TDOA measurement is more accurate.

Usually, the snapshot window length is selected when it can cover a single particle signal.

4.3.2 Cross Correlation and Convolution

A cross correlation can be viewed as a convolution. Their relationship can be illustrated as follows. The cross correlation of two signals x and y is:

$$R_{xy}(\tau) = \int_{-\infty}^{\infty} x(t)y(t+\tau)dt = \int_{-\infty}^{\infty} x(t-\tau)y(t)dt \quad (4\text{-}3\text{-}1)$$

Letting $x_1(t) = x(-t)$, we obtain

$$R_{xy}(\tau) = y(\tau) * x_1(\tau) = \int_{-\infty}^{\infty} y(t)x_1(\tau - t)dt \quad (4\text{-}3\text{-}2)$$

where "$*$" means a convolution operation.

This indicates that the cross correlation is the convolution of two signals: one is the delayed signal $y(t)$, the other is the reversed reference signal $x(-t)$. The detailed proof is given below.

Proof:

$$\text{Let } x_1(t) = x(-t) \quad (4\text{-}3\text{-}3)$$

$$x_1(\tau - t) = x\big(-(\tau - t)\big) = x(t - \tau) \quad (4\text{-}3\text{-}4)$$

From 4-3-1

$$R_{xy}(\tau) = \int_{-\infty}^{\infty} x(t-\tau)y(t)dt \quad (4\text{-}3\text{-}5)$$

Substituting equation 4-3-4 into equation 4-3-5, we obtain

$$R_{xy}(\tau) = \int_{-\infty}^{\infty} x_1(\tau - t)y(t)dt \quad (4\text{-}3\text{-}6)$$

which is identical to equation 4-3-2.

Therefore, the cross correlation of two signals can be found by reversing the reference signal and then convoluting it with the delayed signal.

4.3.3 Two Blocks Cross-Correlation

In order to find the TDOA of the particle signals, it is necessary to set a reference channel. Usually, the first channel is set as the reference channel. The other channel is called the delayed channel. In the reference channel, we set a snapshot window, called the reference window. In the delayed channel, we set a delayed window whose size is the snapshot window size plus the maximal TDOA, where the maximal TDOA is the largest time delay of the particle signal. This is illustrated in the following figure.

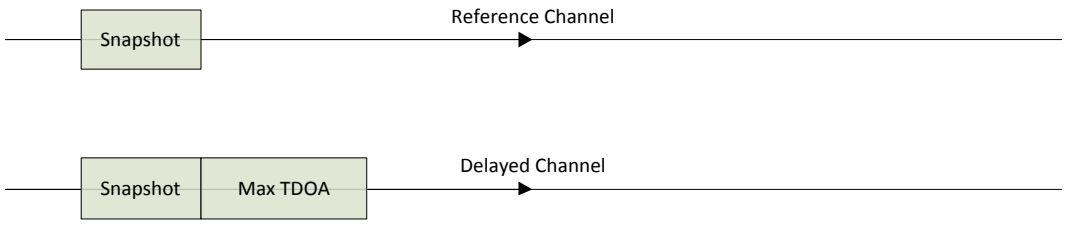

Figure 4.3-1 TDOA Window Selection (28)

Suppose that the snapshot window size is t_s, and the maximum TDOA is t_d, then the delayed window size is $t_s + t_d = t_{sd}$. After the cross correlation of the two windows, the window size of the cross correlation result will be:

$$t_{cr} = t_s + t_{sd} - 1 = 2t_s + t_d - 1 \quad (4\text{-}3\text{-}6)$$

This is because the cross correlation is some kind of convolution except that the reference window is reversed. The algorithms of the cross correlation of the two window signals are stated as follows.

4.3.3.1 The biased algorithm:

1. Initialize the cross correlation window of size t_{cr}.

2. In the delayed window, set a moving window inside the delayed window which has the same size as the reference window.
3. Calculate the cross correlation for the equal-sized windows, the moving window and the reference window.
4. Save the larger result in the cross correlation window.
5. Shift the moving window at a small step (usually it is half of the window size).
6. Repeat 3 to 5 until the window reaches the end of the delayed window.
7. After finishing the internal loop, move the reference window at a step of half the window size.
8. Repeat steps 2-7, until the delayed window reaches the end of the delayed channel.

The reason why the algorithm is called "biased algorithm" is because of the properties of the convolution. Suppose that two blocks have the same size *t*. The size of the convolution result for the two blocks is 2*t* -1. But at each side, *t*-1 values were produced by a non-full size multiplication, i.e. the number of multiplies required to produce those *t*-1 values on each side was less than *t*. So the quantity of the values produced by full size multiplication is:

$$FullSizeMul = 2t - 1 - (t - 1) \times 2 = 1 \quad (4\text{-}3\text{-}7)$$

Similarly, when two blocks are not of equal size, we set the smaller block as the reference block. Suppose its size is *t*, and the size of the larger block, i.e., the delayed block is *s* (*s*>*t*). Then the number of values in the resulting cross-correlation function which are the result of full size (size *t*) multiplications is:

$$FullSizeMul = s + t - 1 - (t - 1) \times 2 = s - t + 1 \quad (4\text{-}3\text{-}8)$$

Example:

Suppose that the reference window size is *t*, the delayed window size is *s* = 8*t* (i.e., that the snapshot window size = *t* and MaxTDOA = 7*t*). Further assume that the step size is *t*/2. The number of steps (window shifts) for the biased algorithm is:

$$steps = floor\left(\frac{8t - t}{\frac{t}{2}}\right) + 1 = 15 \quad (4\text{-}3\text{-}9)$$

and the number of unbiased full size multiplications will be $s - t + 1 = 8t - t + 1 = 7t + 1$.

In order for the correlation function to be "unbiased", all the values in the correlation function should be computed from the same amount of multiplications (for example all from full size multiplications). Detecting a peak not centered around zero can sometimes be an issue in biased correlation functions, because of the linear attenuation (slope) introduced in the function values toward the edges, resulting from the variable number of multiplies used in the computation of the different values. Although the biased method can still lead to satisfactory results in some cases, an alternative is to develop an unbiased correlation version, as below.

4.3.3.2 The unbiased algorithm

The unbiased algorithm involves the following steps:

1. Initialize the cross correlation window. The window size is less than or equal to t_{cr}, which can be determined by the relationship: $t_{cr} - (t_s - 1) \times 2 = 2t_s + t_d - 1 - 2 \times (t_s - 1) = t_d + 1$.
2. Calculate the cross correlations for both the reference window and the delayed window (note: the two windows are not equal-sized).
3. The cross correlation is obtained by reversing the reference window and convolving it with the delayed window. The size of the convolution result is $2t_s + t_d - 1$. To match the cross correlation window, $t_s - 1$ data points will have to be deleted from both sides.
4. Save the larger results in the cross correlation window.
5. Shift the reference window at a small step; usually it is half of the window size.
6. Repeat steps 2 to 5 until the delayed window reaches the end of the delayed channel.

The advantage of the unbiased algorithm is that each cross correlation result comes from a full size multiplication (thus no slope toward the edges), while in the biased algorithm the cross correlation results at both sides ($t_s - 1$ data on each side) gradually attenuate to zero.

4.4 Bi-directional Cross Correlation

The uni-directional cross-correlation takes one channel as the reference channel, and the other as the delayed channel. The algorithm applies only if the particle signal in the reference channel is leading the signal in delayed channel. This is applicable if we know in advance which channel or sensor is upstream and which channel is downstream in practical industrial applications. An alternative is to develop a version of the algorithm which is insensitive to the order (upstream versus downstream) of the two channels or sensors.

The solution is to develop a bi-directional algorithm to measure positive and negative TDOAs of the particle signal. A positive TDOA means that the particle signal at the second channel is delayed, relative to the signal at the reference (first) channel; while a negative TDOA means the opposite situation.

The algorithm is still based on the previous unbiased uni-directional algorithm, but the window structure is different. The following figure shows the window structure for the bi-directional unbiased algorithm:

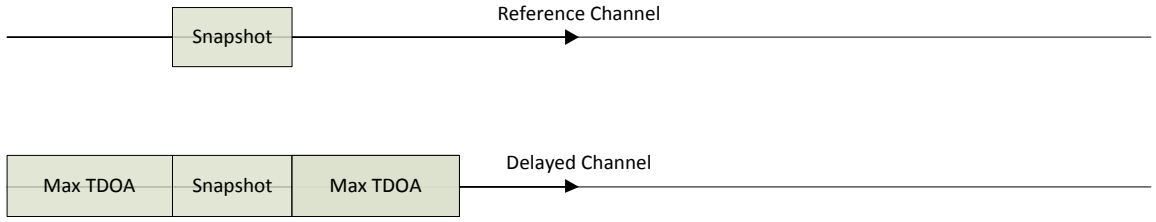

Figure 4.4-1 Window structure for bi-directional algorithm (29)

In such a structure, the beginning of the reference window moves from start 0 to Max TDOA point; the delayed window adds another Max TDOA window at the beginning. The reference window size is still t_s, but the delayed window size is $t_s + 2t_d$.

The cross correlation is between the reference window and the delayed window. The window size of the convolution of both windows is:

$$Convolution\ Win\ Size = t_s + t_s + 2t_d - 1 = 2t_s + 2t_d - 1 \quad (4\text{-}3\text{-}10)$$

The cross correlation window is saved only for values resulting from full size multiplications. Therefore $t_s - 1$ data points will be deleted from both sides. The length of the cross correlation window is

$$Cross\ Corr\ Win\ Size = 2t_s + 2t_d - 1 - 2(t_s - 1) = 2t_d + 1 \quad (4\text{-}3\text{-}10)$$

Thus the algorithm measures the TDOA of the particle in the delayed channel from $-t_d$ to $+t_d$, including 0.

The algorithm is as follows:

1. Initialize the cross correlation window. The window size is $2t_d + 1$.
2. Set the reference window and the delayed window structure as shown in Figure 4.4-1.

3. Calculate the cross correlation for both the reference and delayed windows.
4. The cross correlation is obtained by reversing the reference window and then convolving with the delayed window.
5. Save the larger result in the cross correlation window.
6. Shift the reference window at a small step; usually it is half of the window size.
7. Repeat steps 2 to 6 until the delayed window reaches the last considered value.

4.5 Experimental Results

4.5.1 Particle Signal and Background Noise

This experiment is based on the data mixture of one particle signal and background noise.
The original signal is plotted in Figure 4.5-1. The estimated time delay between the two channel particle signals is approximately 1100 samples, where 1 sample = 0.2ms.

We set the maximal TDOA of the particle as 2000 samples, where 1 sample = 0.2ms. Therefore, the particle signal delay is no more than 0.4s. The snapshot window size is 1000 samples and the window shifts forward at a step of 500 samples. The cross correlation result based on the biased algorithm is shown in Figure 4.5-2. By measuring the highest peak position, at the 1080th sample, the particle TDOA is found to be 1080 samples (maximum peak in the figure).

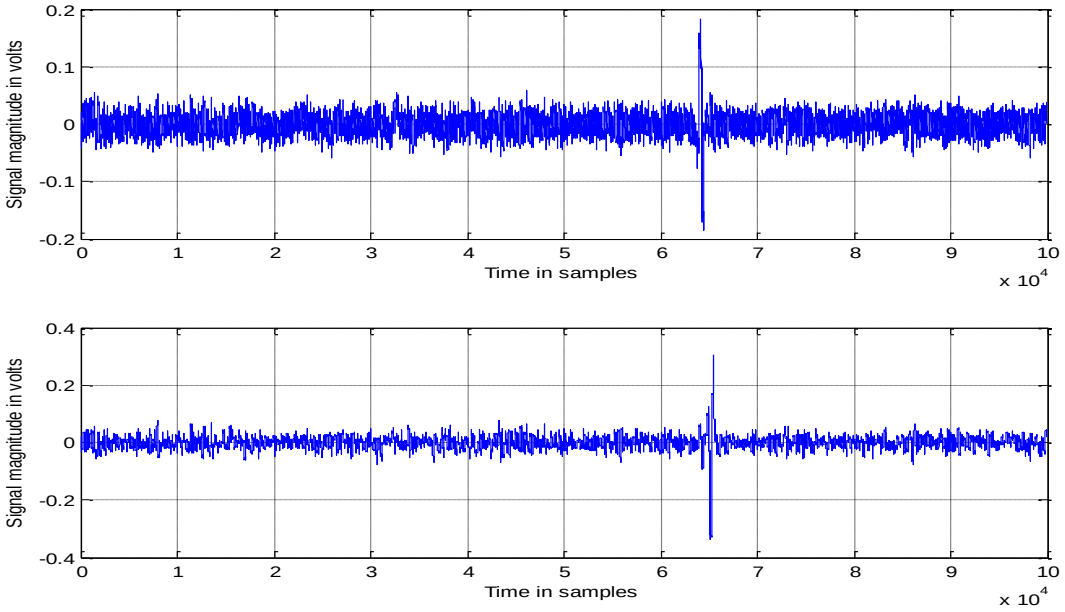

Figure 4.5-1 Particle signal with background noise, time waveforms for channel 1 and channel 2 (30)

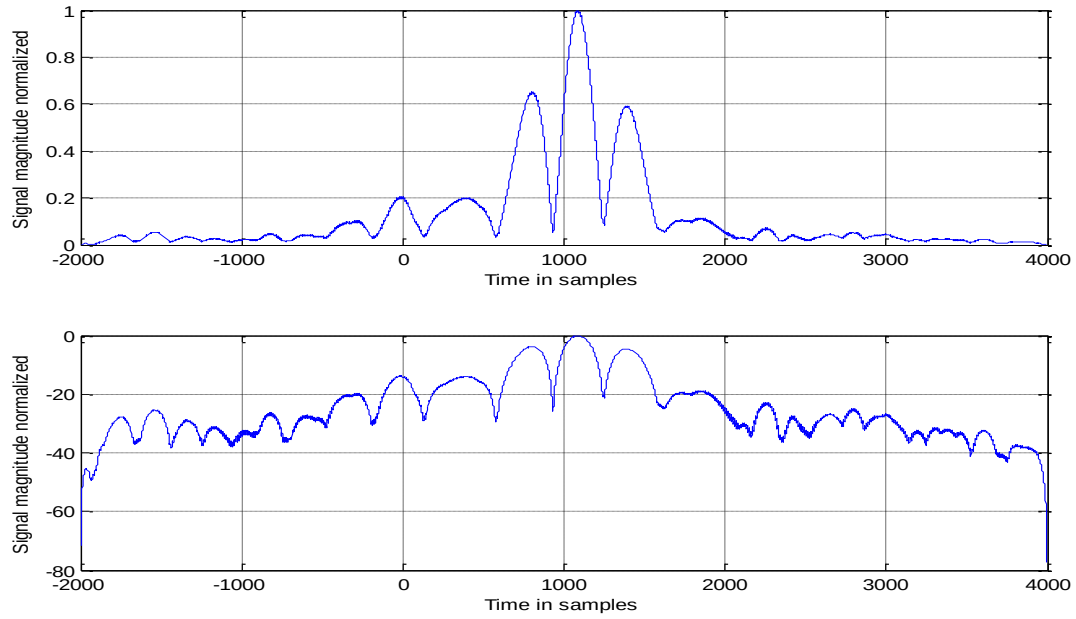

Figure 4.5-2 TDOA measurement with the uni-directional biased algorithm (linear scale and dB scale) (31)

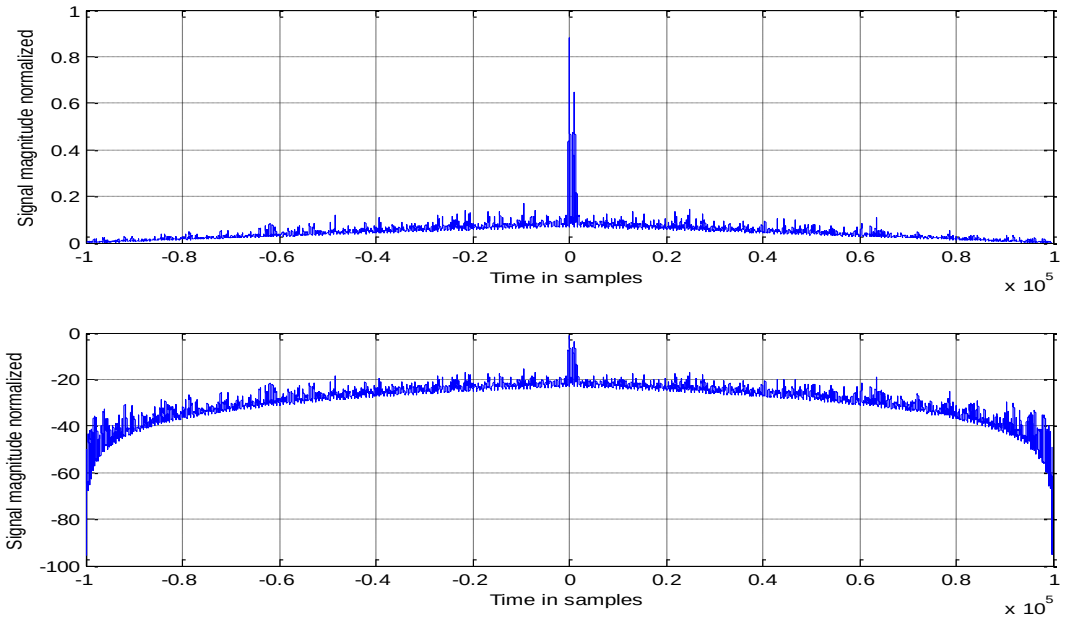

Figure 4.5-3 Cross correlation computed from the whole signal (linear scale and dB scale) (32)

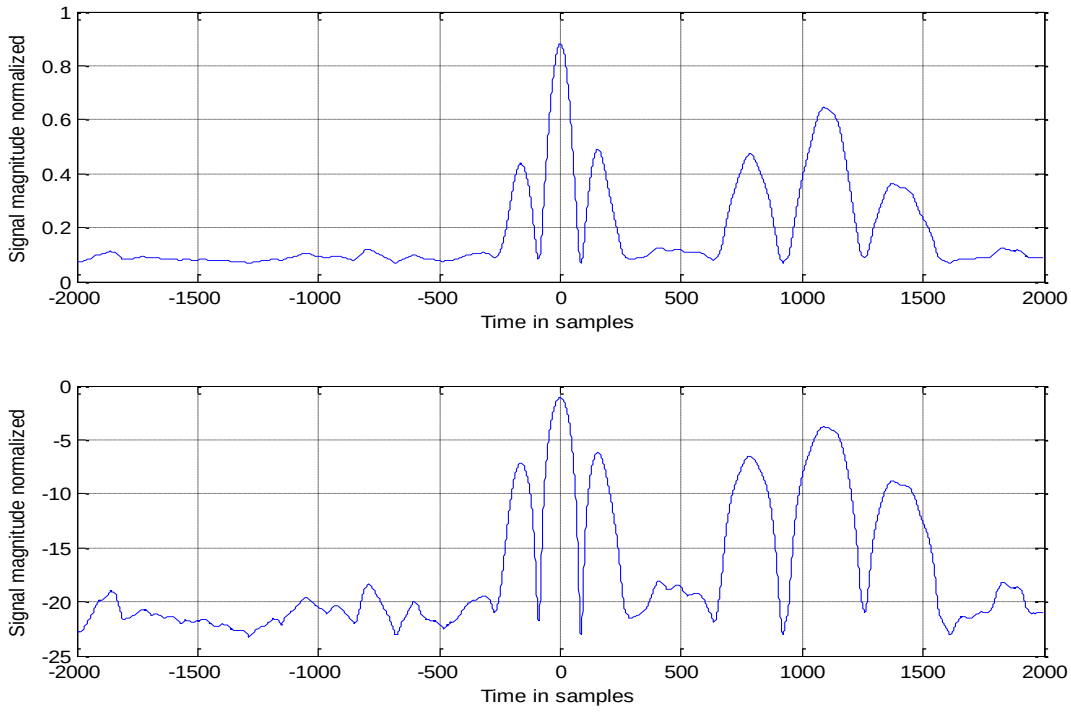

Figure 4.5-4 Zoomed cross correlation function computed from the whole signal (linear scale and dB scale) (33)

If the cross correlation is computed from the whole signal, the particle TDOA is found to be 1093 samples, as shown in Figures 4.5-3 and 4.5-4. In the zoomed Figure 4.5-4, the highest peak indicates the background signal with TDOA = 0. The second peak indicates the particle signal with TDOA = 1093. It means that the average strength of the particle signal is lower than that of the background noise in the view of the whole signal. This is because the particle signal is a transient signal, thus its total energy is small. However, in a snapshot window of 1000 samples, the particle signal power is dominant. This reveals the advantage of data segmentation (Figure 4.5-2 over 4.5-4).

The particle signal cross correlation result obtained by the uni-directional unbiased algorithm is shown in Figure 4.5-5. The measured TDOA from the time of the highest peak is 1087 samples. In the unbiased measurement, there is no attenuation of the sides, as each value is computed with the same amount of sample multiplications.

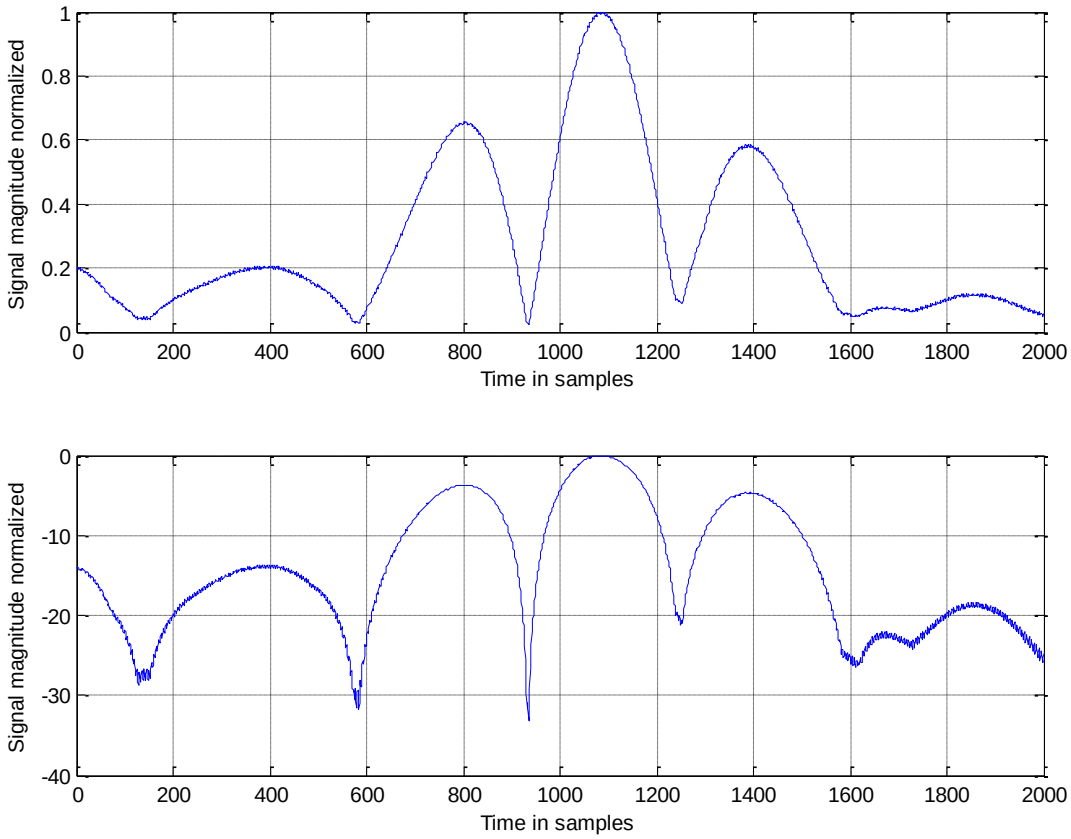

Figure 4.5-5 Cross correlation with the unbiased uni-directional algorithm (linear scale and dB scale) (34)

The last method to be shown is the bi-directional unbiased algorithm. As there is only one particle signal on the positive side in this case, the algorithm does not show any advantage. The cross correlation result of the algorithm is displayed in Figure 4.5-6. The measurement of the TDOA is the same as that of the uni-directional unbiased algorithm, i.e.,1087 samples.

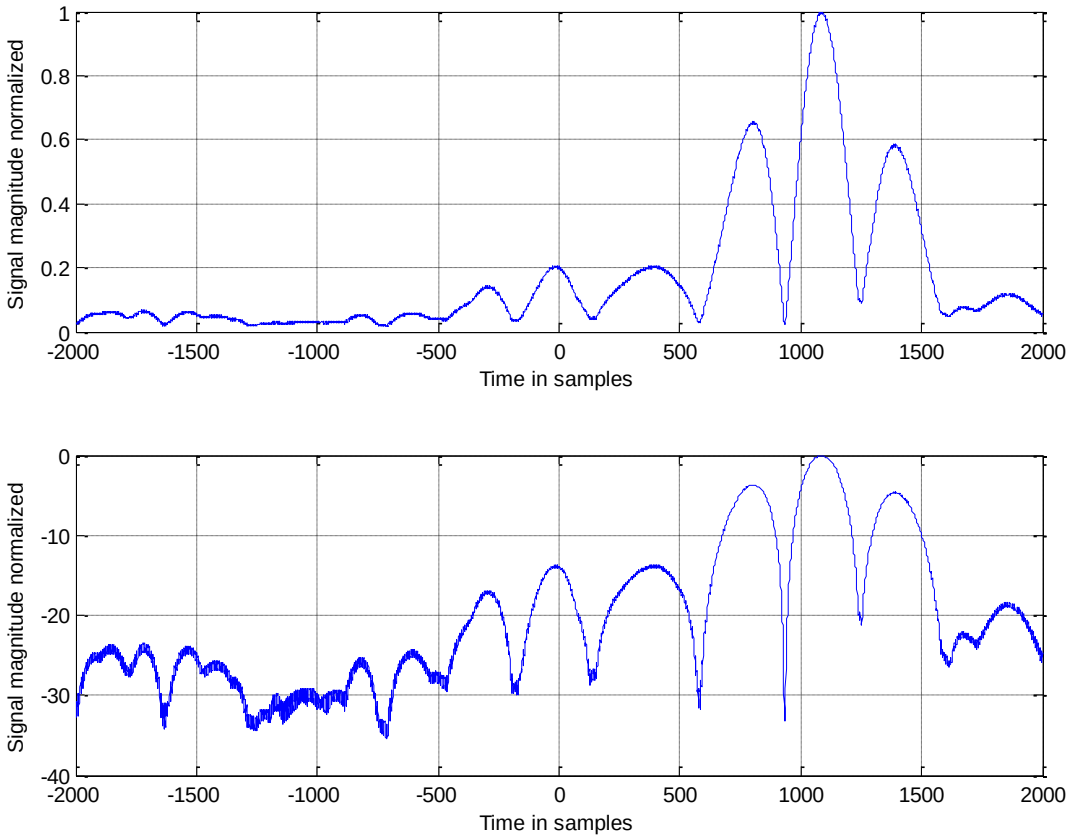

Figure 4.5-6 Cross correlation with unbiased bi-directional algorithm (35)

However, if the delay of the particle signal is on the negative side, the bi-directional unbiased algorithm can capture it, while the uni-directional unbiased algorithm cannot. In this sense, the bi-directional unbiased algorithm is more flexible. An example of such signals using the bi-directional unbiased algorithm is shown in Figures 4.5-7 and 4.5-8. The measured TDOA of the particle is -653 samples, where minus means that the particle signal in channel 2 is leading.

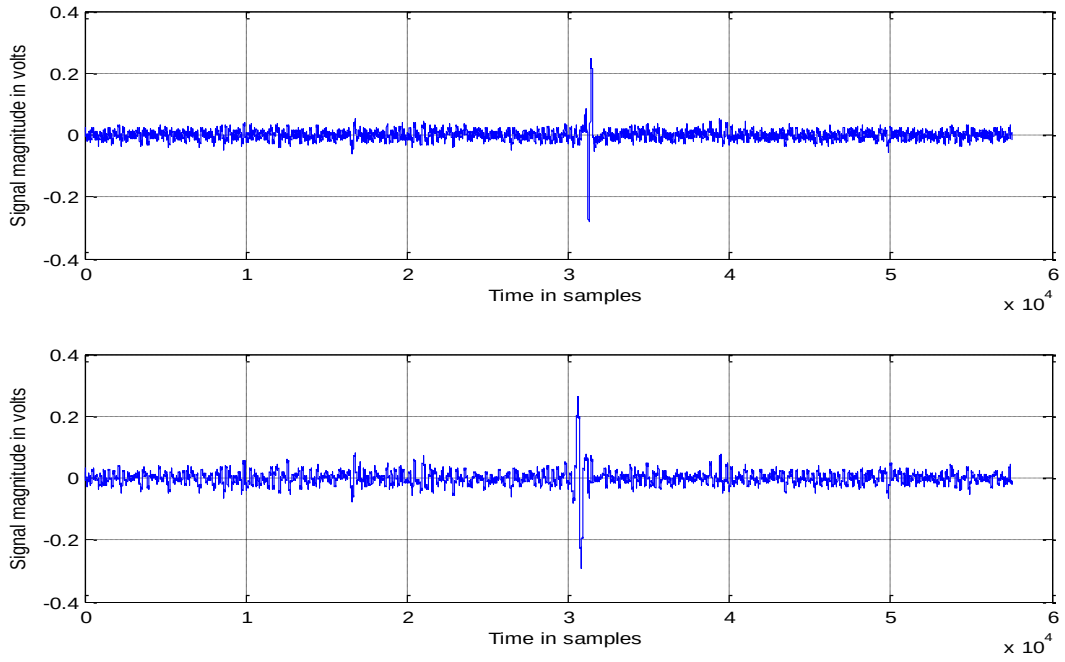

Figure 4.5-7 Case with particle signal in Ch2 leading that of Ch1 (36)

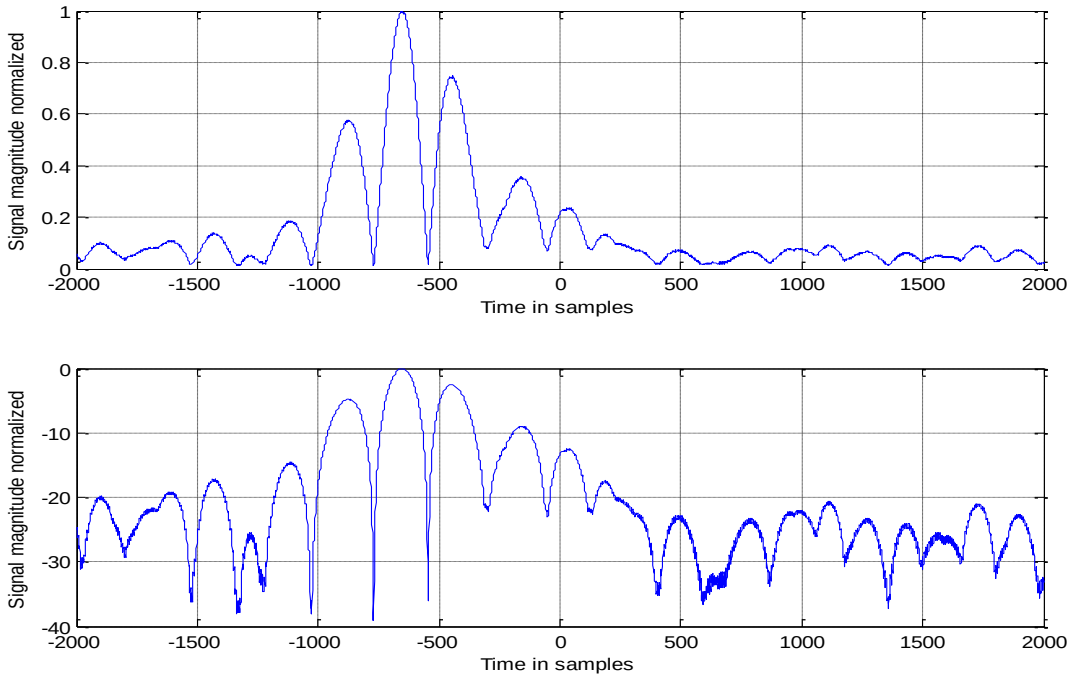

Figure 4.5-8 Cross correlation result by the bi-directional unbiased algorithm (linear scale and dB scale). (37)

4.5.2 Particle Signal and Vibration Interference

When the vibration signal becomes strong and comparable to (or larger than) the particle signal, the vibration signal side lobes will severely interfere with the particle signal peak in the cross correlation diagram. In this case, it is often impossible to distinguish the particle peak and the vibration side lobe peak. The TDOA measurement becomes unstable and inaccurate. It is therefore not recommended to measure the TDOA directly from the original signals under such situations, as further illustrated in the following figures.

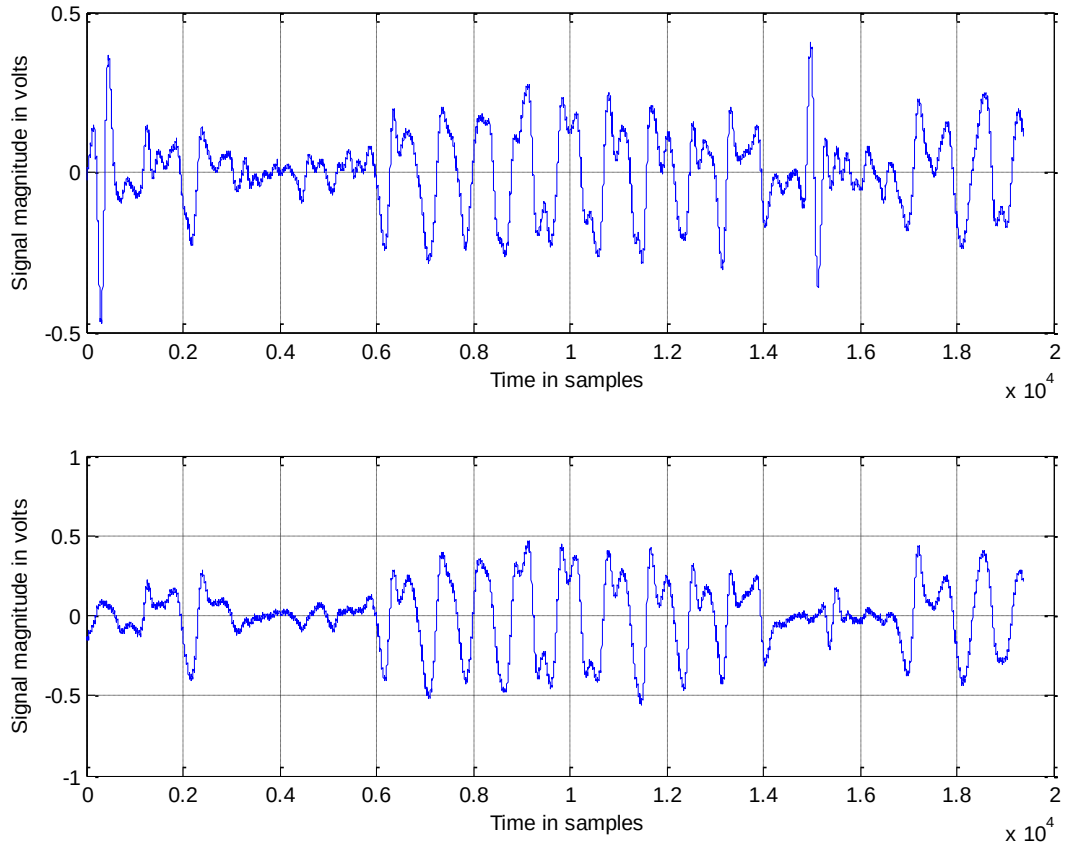

Figure 4.5-7 Vibration signal and particle signal mixed (38)

In Figure 4.5-7, a particle signal is embedded in the sequence of vibration signals. The time delay of the particle signal between the two channels is estimated as 542 samples. Figure 4.5-8 is

the cross correlation with the uni-directional biased algorithm. From the figure, the measured TDOA is 949 samples (the second highest peak). The vibration main lobe is at TDOA = 0 samples, but its side lobes are distributed on both sides of the main lobe. The side lobes interleave the particle peak and make the measurement ambiguous.

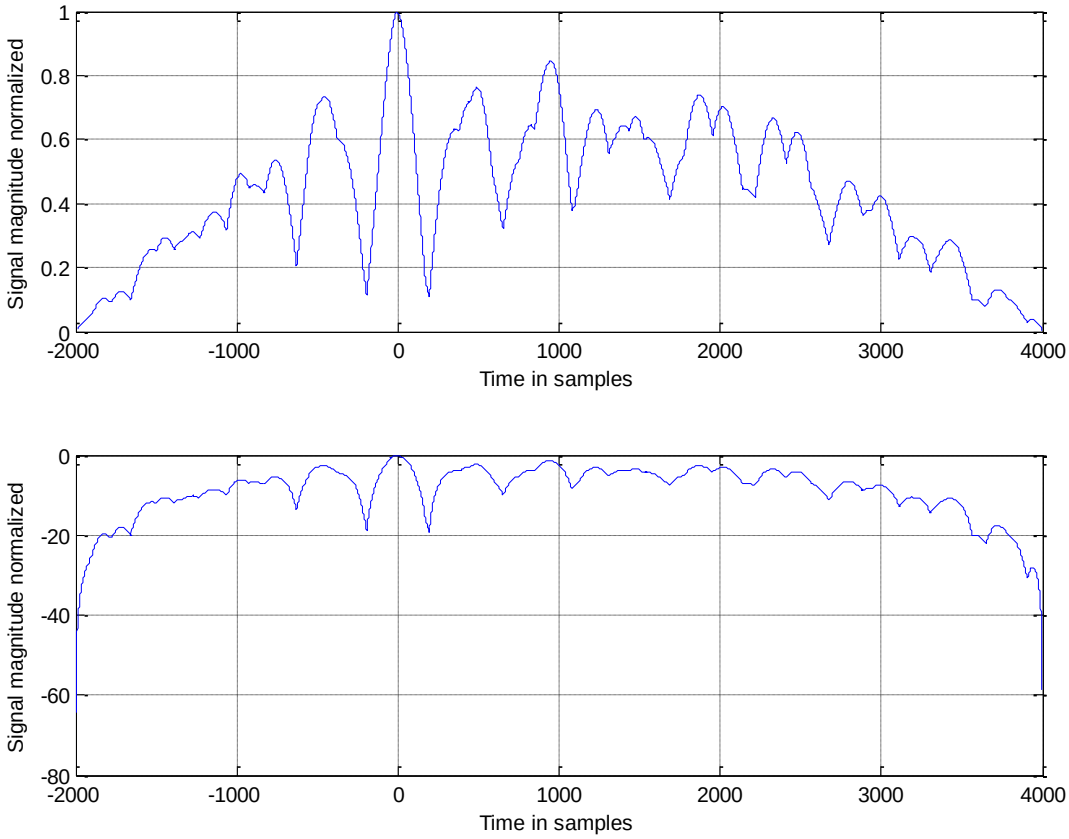

Figure 4.5-8 Cross correlation in uni-directional biased algorithm (linear scale and dB scale) (39)

This illustrates that for signals where the vibration signal level is of the same order or greater that the particle signal level, the TDOA measurement method can't be applied directly on the original signals. A solution to this problem will be presented in the next chapter.

4.6 Conclusion

In this section, a TDOA detection algorithm was introduced to measure the time difference (time delay) of the particle signals in two channels and to detect the particle existence. For example, in the case considered, if the signal time delay is in the range of 100 to 2000 samples, we can conclude that a particle is detected; otherwise, the associated signal will not be considered as a particle signature. Alternatively, the level of the TDOA peak in the correlation function evaluated by the different algorithms presented could also be used (with a threshold) to detect particle existence. However, the TDOA algorithm requires a dominant particle signal power for accurate measurement. This means that the vibration signal should be attenuated before TDOA measurement. A technique to filter out the vibration signal will be discussed in the next chapter.

Chapter 5 Phase Angle Selective Beamforming and AOA Filtering

5.1 Introduction

In order to more accurately capture a particle signal, it is necessary to filter out the background noise signal and the vibration signal, and hence to improve the signal to noise and interference ratio (SNIR). As a vibration or a background noise signal has a different phase character from a particle signal, it is possible to design algorithms to selectively filter out the unwanted vibration signals. In this chapter, a beamforming method, called the Phase Angle Selective Beamforming (PASB method), and a phase filtering method, called AOA filtering method, are proposed. The PASB method is based on Uniform Linear Array (ULA) beamforming, beamforming steering, and Least Mean-Square (LMS) pattern synthesis technology [52]. The AOA filtering method is based on the AOA detection algorithm introduced in Chapter 3. Finally, these two methods are compared in the respect of the accuracy of the particle existing, and the improvement of the SNR.

Beamforming [53] has been studied in the areas of wireless communication, sonar and radar systems for a long time. The purpose of the technology is to enhance the target signal received by an antenna in some direction. Hence it is also called a spatial filter. As the phase of the received signal at each sensor of an antenna array is different, it is possible to design a beam pattern to enhance the signal in one direction, while attenuating the signal in other directions. This idea can be borrowed for the ODM anti-vibration system design in this thesis.

5.2 Single Frequency Beamforming System

5.2.1 Uniform Linear Array (ULA)

A simple beamforming system is the uniform linear array sensor as shown below:

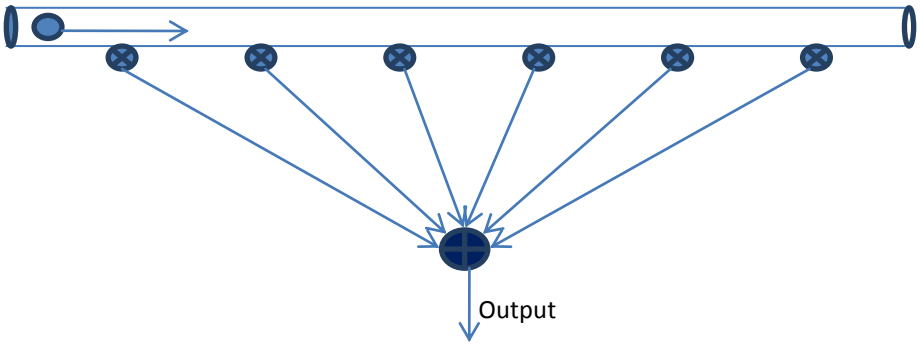

Figure 5.2-1 Uniform linear array (ULA) Sensor (40)

When a particle passes through an array sensor tube, assuming free field propagation it will stimulate a linear phase delay signal at each sensor element. Suppose that every sensor element is identical and that the particle only stimulates a single frequency (a broadband case will be discussed later), then the received signal of each element will be:

$$x_i(t) = ae^{j(\omega t+\phi_i)} \qquad i = 1, \dots, N \tag{5-2-1}$$

where *N* is the element size of the sensor array.

As each element receives the same frequency, $e^{j\omega t}$ can be dropped, and we can leave only the complex number, $e^{j\phi_i}$, the phasor. If the first element is selected as the reference point and we set $\phi_1 = 0, \phi_2 = \phi, \dots ,$ then $\phi_i = (i-1)\phi,$ where ϕ is the phase delay between two neighbor elements.

Therefore the total signal output of the sum of all elements will be:

$$y_{out} = \sum_{i=1}^{N} ae^{j(i-1)\phi} = \frac{sin\left(\frac{N\phi}{2}\right)}{sin\left(\frac{\phi}{2}\right)} a \tag{5-2-2}$$

Let ϕ scan from $-\pi$ to π, the beam pattern of y_{out} is then as shown in Figures 5.2-2 and 5.2-3.

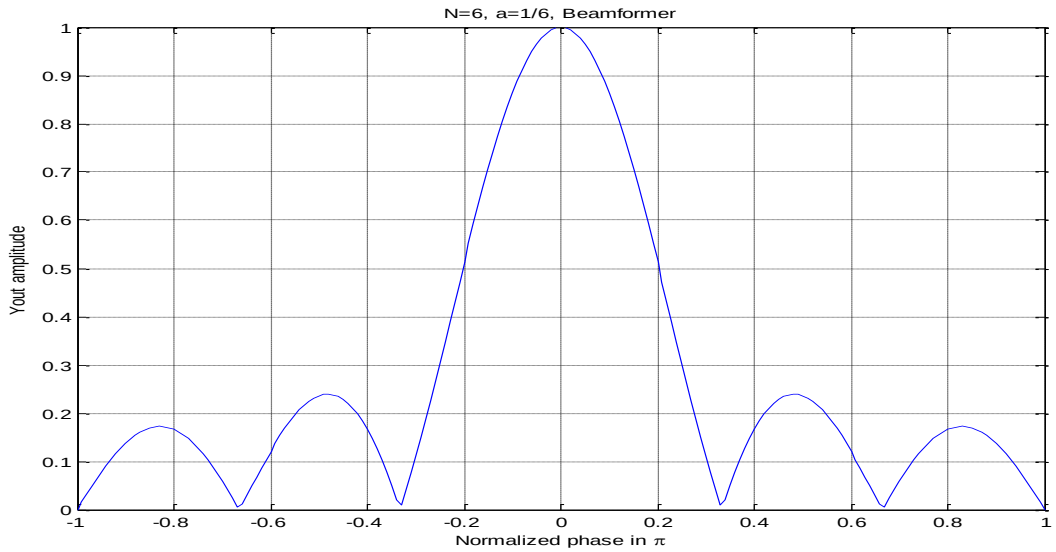

Figure 5.2-2 *N*=6, *a*= 1/6 ULA Beam Pattern (41)

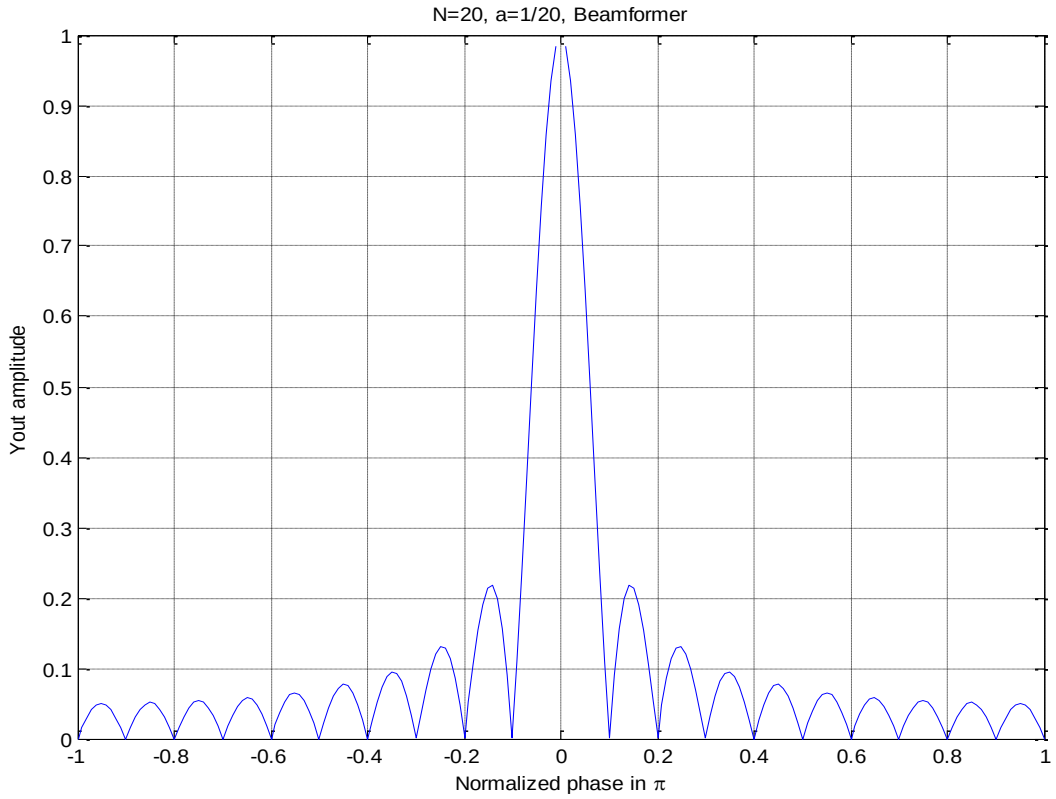

Figure 5.2-3 *N*=20, *a*= 1/20 ULA Beam Pattern (42)

From the figures 5.2-2 and 5.2-3, we can draw the following conclusions:

1. The main lobe level is normalized to 1, and the first side lobe level is about 0.22 (-13dB), regardless of the element size *N*.
2. The element size *N* does not affect the first side lobe level, but it does affect the main lobe beamwidth. When *N* =6, the beamwidth = 0.4; when *N* = 20, the beamwidth = 1.4. This indicates that when *N* is larger, the main lobe beamwidth becomes narrower.
3. The ideal beam pattern is a pattern with a small side lobe and a narrow main lobe beam. But ULA beamforming cannot reach it. ULA does narrow the beam width with *N* increasing, but it cannot decrease the side lobe level. To improve the side lobe level, non-uniform weighting will be adopted (as opposed to simply summing the sensor signals).
4. Furthermore, the main lobe direction of ULA is at zero, which is not always the ideal direction. In chapter 3, the vibration phase is at zero and the particle phase is distributed between 0 and 2π. Hence the beamformer needs to put nulls at the zero direction to filter out the vibration signal, and steer the main lobe direction towards the direction which is far away from the zero direction, such as $\pi/2$.
5. There is no strict criterion for a particle direction unless it does not overlap with a vibration direction. In some of our recent experimental setups, vibrations have in some cases appeared with a π phase difference (opposite polarity). Thus selecting the particle direction at $\pi/2$ is safer to cover for 0 and π possible phase differences for the vibrations.

As discussed above, our desired beam pattern is that the main lobe is at the direction $\pi/2$ with small side lobes. A simple ULA cannot reach it. The only way to achieve this is to change the element weights. The following will introduce the technique of the weighting selection to improve the beam pattern.

5.2.2 Steering the Beam Pattern.

If each element signal is delayed by a phase relative to the first element and they are then summed together, the new pattern is steered at the phase. This method is called Delay and Sum

(DS) model. Based on this idea, the element weighting is not a constant $\boldsymbol{a}$, but $a \times e^{-j(i-1)\phi_0}, i = 1, \ldots N$, where ϕ_0 is the steering phase.

Formula 5-2-2 is rewritten as:

$$y_{out} = \sum_{i=1}^{N} a e^{j(i-1)(\phi-\phi_0)} = \frac{sin\left(\frac{N(\phi-\phi_0)}{2}\right)}{sin\left(\frac{(\phi-\phi_0)}{2}\right)} a \qquad (5\text{-}2\text{-}3)$$

The steering pattern is plotted in Figure 5.2-4. Comparing the pattern with that in Figure 5.2-3, the main lobe is steered at the phase π/2. Therefore, it is possible to obtain a desired beam pattern by changing the element weighting. More details about this method will be discussed in the following sections.

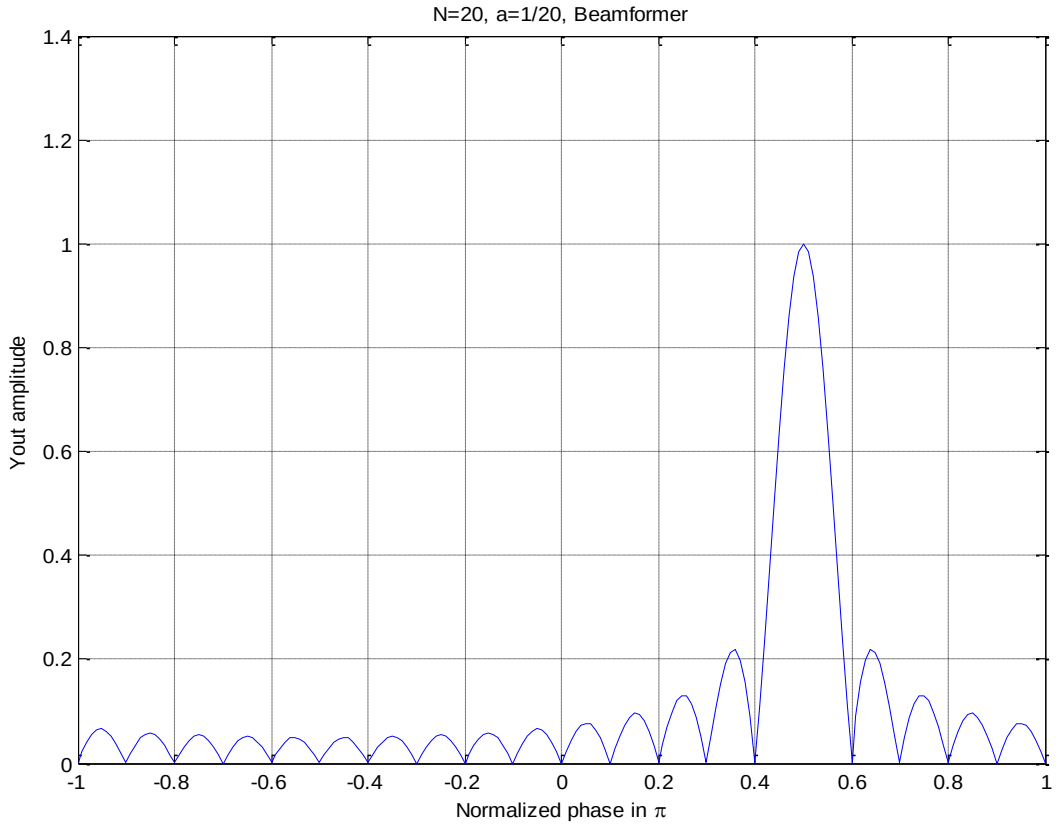

Figure 5.2-4 *N*=20, *a*= 1/20 Delay and Sum Beam Pattern (43)

5.2.3 Side Lobe Level

In the ULA design, increasing the number of elements can decrease the beamwidth of the main lobe but it cannot lower the level of the side lobes. Non-uniform coefficients may help to achieve to purpose of smaller side lobes, at the expense of slightly large mainlobes. There are several types of weighting schemes with different effects on the side lobes, each with its own merits and shortcomings.

1. Rectangular window weighting

The weighting coefficients are all set to one, which will not change the ULA coefficients.

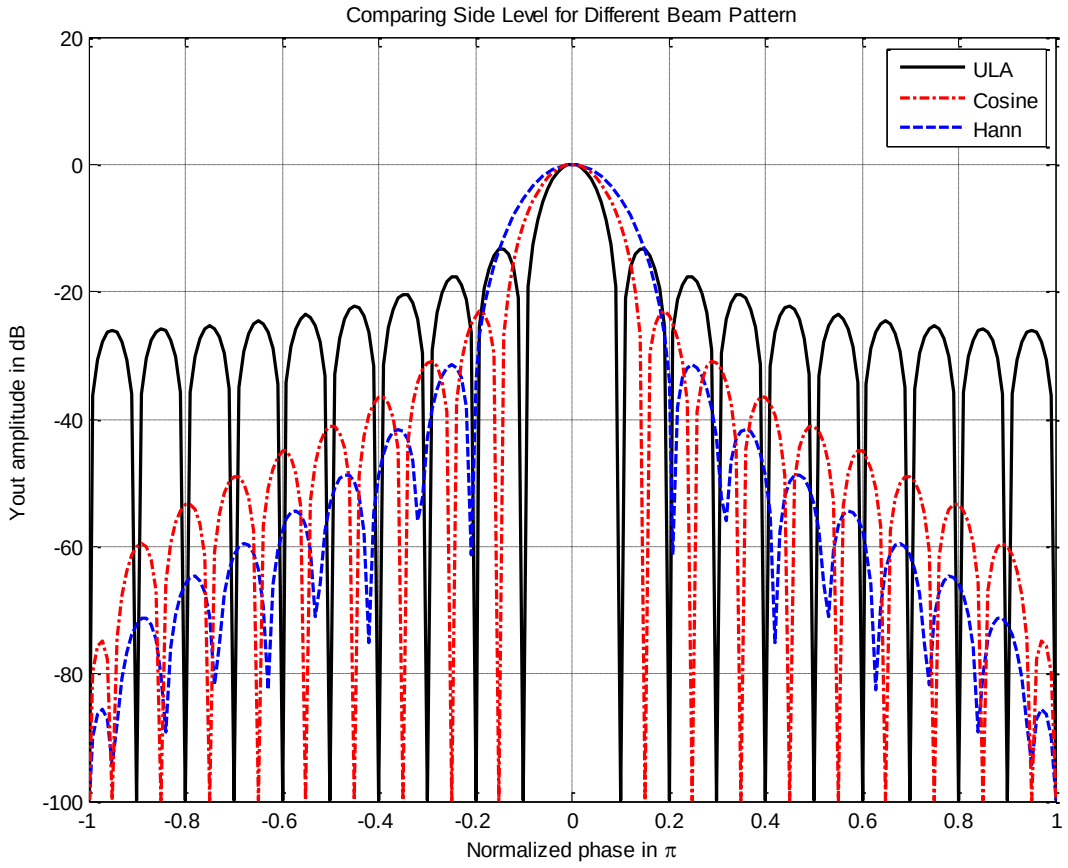

Figure 5.2-5 *N*=20, ULA, Cosine, Hanning Beam Pattern (44)

2. Raised cosine weighting

The following is the Matlab code for specifying the raised cosine weighting coefficients:

```
p = 0; N=20; Pos = -(N-1)/2:1:(N-1)/2;      %constant
c = p/N + (1-p)*sin(pi/(2*N));
W = c*(p + (1-p)*cos(pi/N*Pos));  %weighting coefficients
```

3. Hanning Window

The following is the Matlab code for specifying the Hanning (or von Hann) weighting coefficients:

```
w = hann(N);          %Matlab hanning window function.
```

Comparing the above three types of weighting, we observe the following from Figure 5.2-5:

1. The main lobe beamwidth and side lobe level are inversely proportional for a certain element array. When the side lobe level is lower, its main lobe beamwidth will become larger. In the Figure 5.2-5, the Hanning pattern's side lobe level is the lowest, but the beamwidth of the main lobe is the largest.
2. It is impossible to find a beam pattern with the lowest side lobe level and at the same time the narrowest main lobe beamwidth for a certain element size. The low side lobe level is at the expense of the main lobe beamwidth.
3. Increasing the element size will decrease the beamwidth, without affecting that much the side levels. For example, the main lobe beamwidth for N=20 is 0.4 π; for N=40, it is 0.2 π (Figure 5.2-6).
4. However, increasing the number of elements will lead to higher hardware cost and will require more computational power.

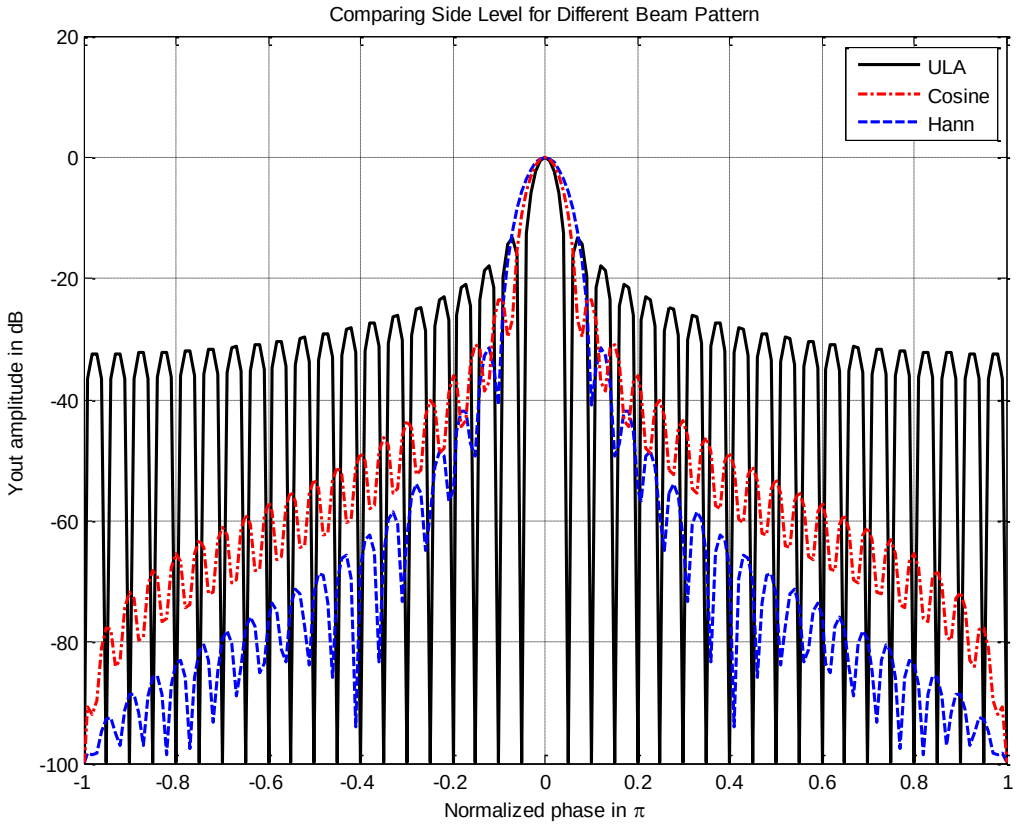

Figure 5.2-6 N = 40, ULA, Cosine, Hanning Beam Pattern (45)

5.2.4 Base Beamforming

As the Hanning window has the lowest side lobe, it is selected as the space filter window for our experiments later on. By steering it at π/2, when the element size is 40, the beamforming result is plotted in Figure 5.2-7. This beam pattern is intended to amplify the phase between 0.4 to 0.6 π, and to attenuate the phase at other directions. As Figure 3.5-4 showed, the vibration signal for almost all frequencies are at around 0 degree phase shift, and they will be attenuated by 70 dB with this pattern. This pattern can be used to filter out vibration signals. But it can also be improved by using the "Null Steering and LMS Pattern" method described next.

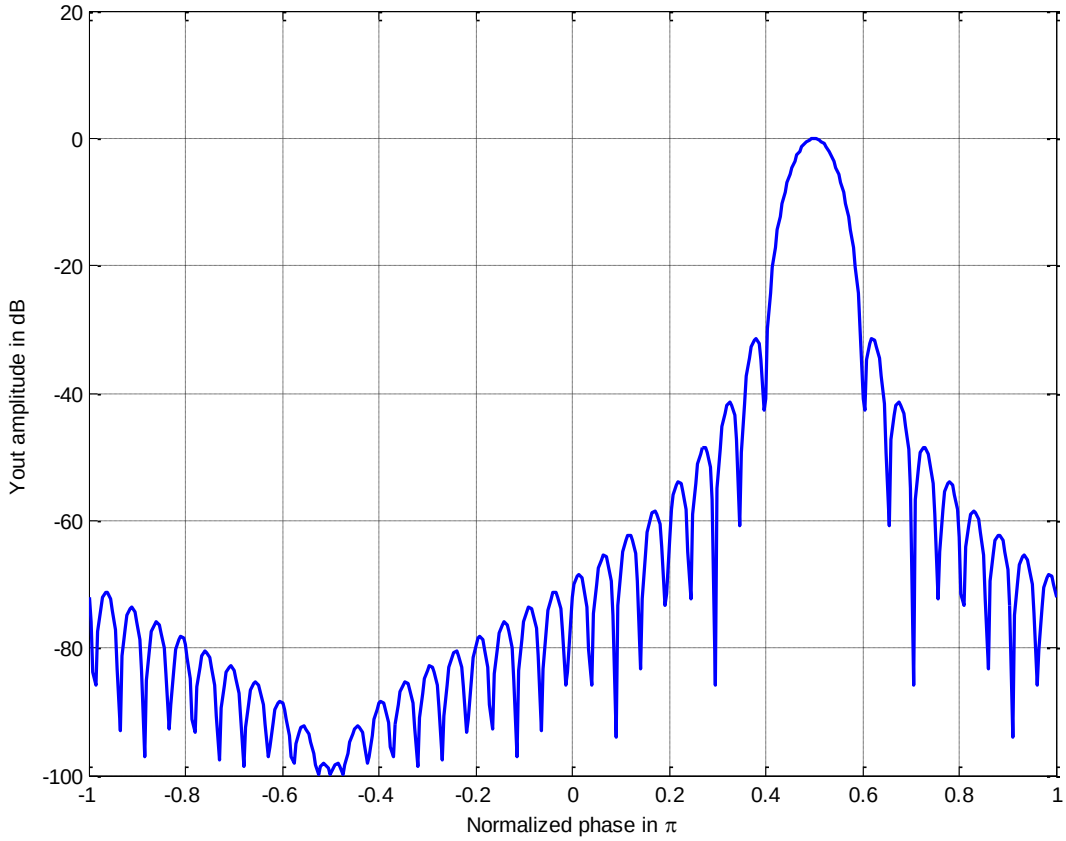

Figure 5.2-7 N = 40, Hanning beam steering at 0.5π (46)

5.2.5 Null Steering and LMS Pattern

As stated before, the vibration signal is from around the zero direction. In order to improve the beam pattern performance, it is necessary to lower the level or gain from the zero direction. At present, the level is about -70dB.

This problem can be stated as: Find an approximate pattern which has least mean square (LMS) error to the base pattern, subject to the following null constraints.

Let $\phi_{\mathrm{i}} = 0, 0.05, 0.95, 1$ (i = 1,2,3,4) null points, (in units of π). The base pattern is

$$F_b(\boldsymbol{\phi}) = \boldsymbol{w}_b^{+}\, \boldsymbol{v}(\boldsymbol{\phi}) \qquad (5\text{-}2\text{-}4)$$

where $\boldsymbol{w}_b$ is the base pattern element weight, $\boldsymbol{v}(\boldsymbol{\phi})$ is the manifold vector given by:

$$\boldsymbol{v}(\boldsymbol{\phi}) = \left[1, e^{j\phi}, e^{j2\phi}, \dots e^{jN\phi}\right]^T \quad (5\text{-}2\text{-}5)$$

The estimated pattern will be

$$F_s(\boldsymbol{\phi}) = \boldsymbol{w}_s^+ \boldsymbol{v}(\boldsymbol{\phi}) \quad (5\text{-}2\text{-}6)$$

The LMS of the two patterns will be

$$\mathcal{E} = \int_{-\pi}^{\pi} |F_s(\boldsymbol{\phi}) - F_b(\boldsymbol{\phi})|^2 d\boldsymbol{\phi} = |\boldsymbol{w}_s^+ - \boldsymbol{w}_b^+|^2 \quad (5\text{-}2\text{-}7)$$

under the constraint condition

$$\boldsymbol{w}_s^+ \boldsymbol{v}(\boldsymbol{\phi_i}) = \boldsymbol{0}, \qquad i = 1,2 \dots k \quad (5\text{-}2\text{-}8)$$

Define

$$\boldsymbol{C} = [\boldsymbol{v}(\phi_1), \boldsymbol{v}(\phi_2), \dots, \boldsymbol{v}(\phi_i), \dots, \boldsymbol{v}(\phi_k)] \quad (5\text{-}2\text{-}9)$$

The constraint expression can be modified as:

$$\boldsymbol{w}_s^+ \boldsymbol{C} = \boldsymbol{0} \quad (5\text{-}2\text{-}10)$$

The problem can be described as follows: find $\boldsymbol{w}_s$ to make $\mathcal{E}$ minimal under the condition as described by expression 5-2-10. Using the Lagrange method, it can be deducted (see [22] in details) that

$$\boldsymbol{w}_s = (\boldsymbol{I}_N - \boldsymbol{P})\boldsymbol{w}_b \quad (5\text{-}2\text{-}11)$$

where $\boldsymbol{P} = \boldsymbol{C}(\boldsymbol{C}^+\boldsymbol{C})^{-1}\boldsymbol{C}^+$. In our case, both $\boldsymbol{w}_b$ and $\boldsymbol{C}$ are known. Hence $\boldsymbol{w}_s$ can be found and its corresponding beam pattern is shown in Figure 5.2-8:

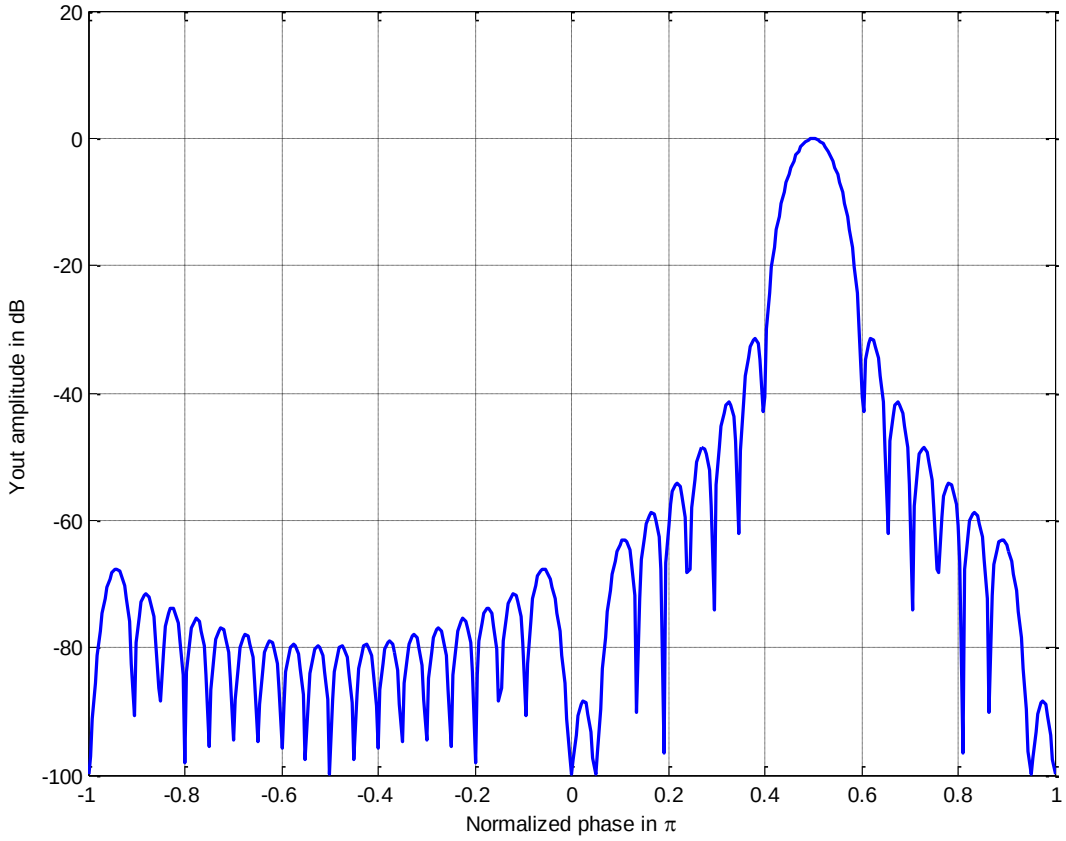

Figure 5.2-8 N = 40, Hanning beam steering at 0.5π with null constraints (47)

Comparing Figures 5.2-7 and 5.2-8, the side lobe levels around 0 and π directions have been decreased from -70dB to -90dB. At the same time, it also boosts the level in other directions, such as the -0.5 π direction. This beamforming behavior is acceptable and it will be verified by filtering vibration signals in the ODM system, as discussed in the following sections

5.3 Broadband and Narrowband Signals

In reality, the received signals in our prototype are not narrowband, but broadband signals with a bandwidth of about 60Hz. As the beamforming theory is mostly based on narrowband processing, it is necessary to convert the received broadband signal into narrowband signals such as separated single frequency signals with an FFT. Each single frequency signal can be filtered out

by the beamforming system. Therefore the broadband problem can be dealt with using the narrowband beamforming method in the FFT domain.

5.4 Virtual Sensor Array

In the ODM prototype, there are only two sensors to form the sensor array. In reality, it is not practical to build a huge element (such as 40) sensor array because it will occupy a large size and require a heavy hardware investment. A simple solution to the problem is the virtual sensor array method.

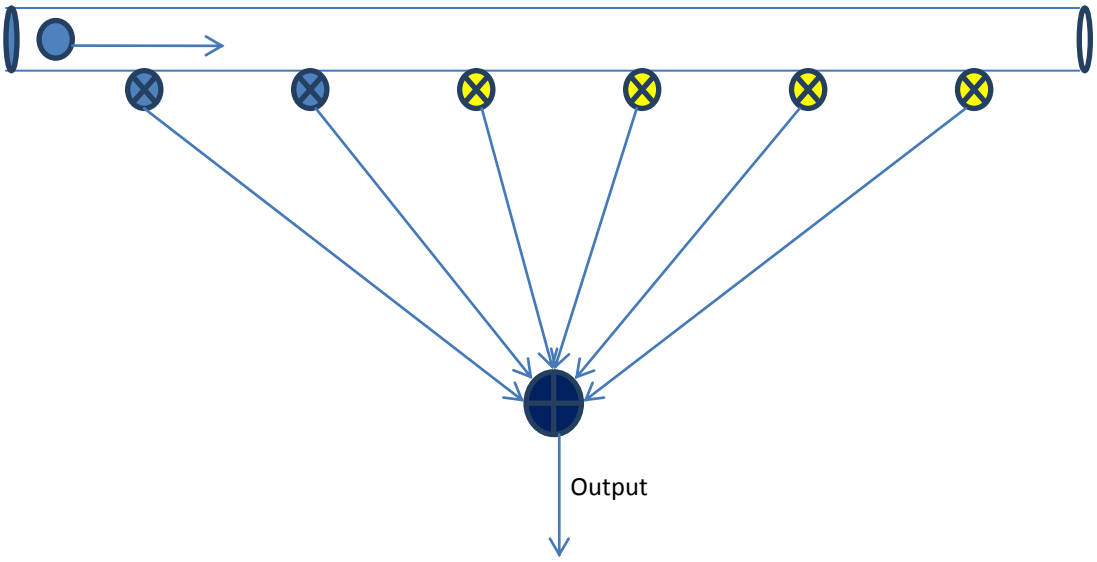

Figure 5.4-1 Virtual Sensor Array Model (48)

Suppose that a virtual 6-element array is created but there are only two real elements actually receiving signals. When a particle passes through the sensor array, it will generate a delayed signal at each element, i.e.,

$$x_1 = x(t), x_2 = x(t-\tau), \dots x_i = x(t-(i-1)\tau)\ i = 1, \dots N$$

where *N* is the array size. Suppose that each element is identical. Then in the frequency domain, the received signal of each element can be expressed as ($i = 1, \dots N$)

$$X_1 = X_1(\omega), X_2 = X_1(\omega)e^{-j\omega\tau}, \dots, X_i = X_1(\omega)e^{-j\omega(i-1)\tau} \quad (5\text{-}4\text{-}1)$$

For a certain frequency ω, let $X_1(\omega) = A_1 e^{j\phi_1}, \phi = -\omega\tau$, then

$$X_1 = A_1 e^{j\phi_1}, X_2 = A_1 e^{j(\phi_1+\phi)}, \dots, X_i = A_1 e^{j(\phi_1+(i-1)\phi)} \quad (5\text{-}4\text{-}2)$$

For a certain frequency ω, $X_1'$and X_2' are detected by the real sensors:

$$X_1' = B_1 e^{j\psi_1}, X_2' = B_2 e^{j\psi_2} \quad (5\text{-}4\text{-}3)$$

where B_1 and B_2 are the amplitudes of the real received signals and ψ_1 and ψ_2 are the signals' phases. B_1 and B_2 will not be equal because the real sensors have non-identical characteristics, and because of the presence of some measurement noise. Let

$$\hat{A}_1 = \frac{\mathrm{B}_1 + \mathrm{B}_2}{2}, \hat{\phi} = \psi_2 - \psi_1, \hat{\phi}_1 = \psi_1 \quad (5\text{-}4\text{-}4)$$

Then $\hat{A}_1, \hat{\phi}_1,$ and $\hat{\phi}$ are respectively the estimates of $A_1, \phi_1,$ and ϕ from the practical measurement.

Using $\hat{A}_1, \hat{\phi}_1,$ and $\hat{\phi}$, $X_1, X_2, \dots, X_N$ can then all be found by substituting these variables into equation 5-4-2. As the space filter weight $\boldsymbol{w}_s$ is available in 5-2-11, then the output is $Y(\omega) = \boldsymbol{w}_s^+ \boldsymbol{X}$. This response $Y(\omega)$ is for some specific frequency. When the outputs of all frequencies in the bandwidth are available, the output in the time domain, *y(t)*, can be calculated by an inverse FFT operation.

5.5 Experimental Results

Here we consider a case where vibration signals are stronger than the particle signals (hereafter, this case is called Example 1). Figure 5.5-1 shows the dual-channel original signals at the sampling frequency of 1 KHz. Figure 5.5-3 shows the results after applying the PASB method.

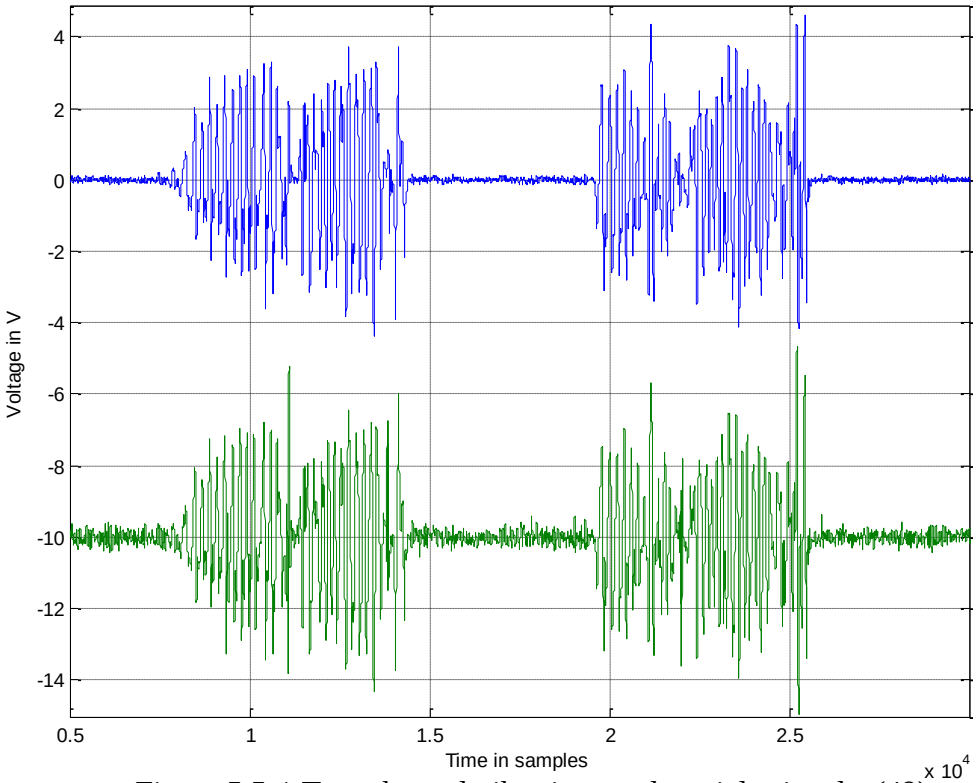

Figure 5.5-1 Two channel vibrations and particle signals. (49)

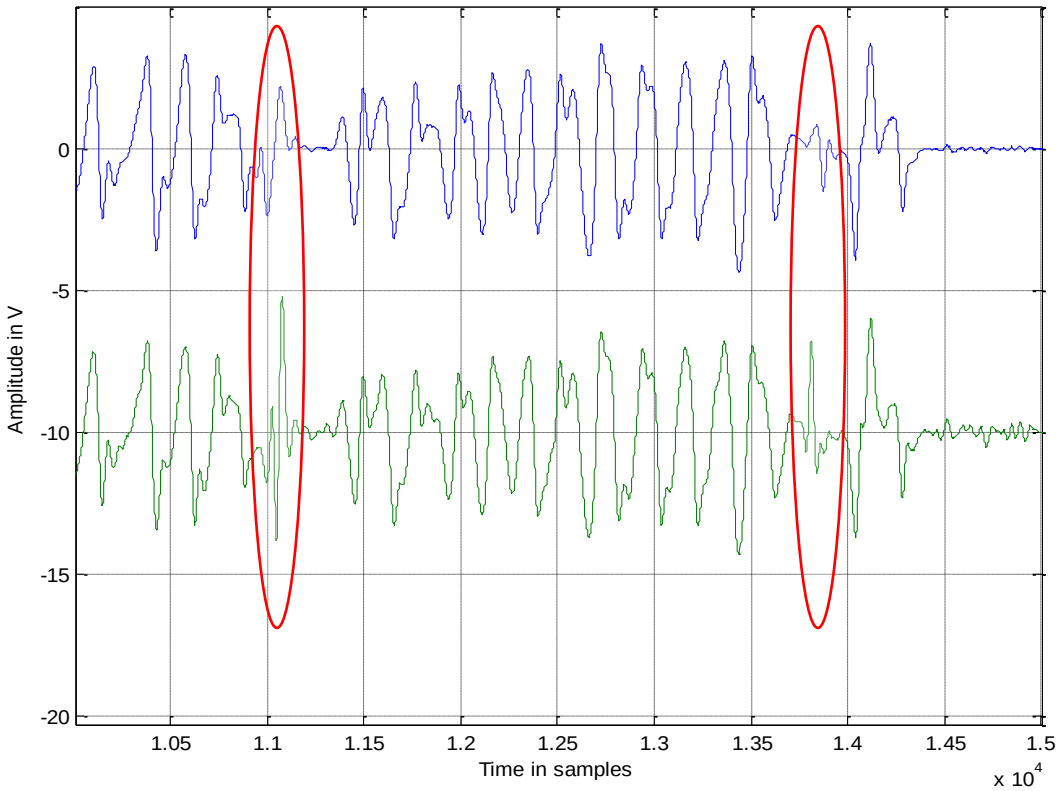

Figure 5.5-2 Details of the particle signals in the vibration signal sequence. (50)

1. As shown in Figure 5.5-1, it is very difficult to distinguish a particle signal when it is interfered by vibration signals. But there are still some different characters between them: the vibration signals are almost exactly in phase, but the particle signals in both channels have a phase delay. The particle signals are shown in red circles in Figure 5.5-2.

2. The Signal to Noise and Interference Ratio (SNIR) before PASB processing can be roughly estimated by the method below.

   I. Measure the highest particle signal amplitude (peak to peak) for channel 1 and channel 2 in Figure 5.5-2.

$$\mathrm{AmpOfParPP_{ch1}} = 4.0, \quad \mathrm{AmpOfParPP_{ch2}} = 8.2$$

   II. Measure the highest vibration signal amplitude (peak to peak) for channel 1 and channel 2 in Figure 5.5-2.

$$\mathrm{AmpOfVibPP_{ch1}} = 8.0, \quad \mathrm{AmpOfVibPP_{ch2}} = 8.0$$

   III. Calculate SNIR for both channels.

$$\mathrm{SNIR_{ch1}} = \frac{\mathrm{AmpOfParPP_{ch1}}}{\mathrm{AmpOfVibPP_{ch1}}} = \frac{4.0}{8.0} = 0.50 = -6.0\mathrm{dB} \qquad (5\text{-}5\text{-}1)$$

$$\mathrm{SNIR_{ch2}} = \frac{\mathrm{AmpOfParPP_{ch2}}}{\mathrm{AmpOfVibPP_{ch2}}} = \frac{8.2}{8.0} = 1.03 = 0.21\mathrm{dB} \qquad (5\text{-}5\text{-}2)$$

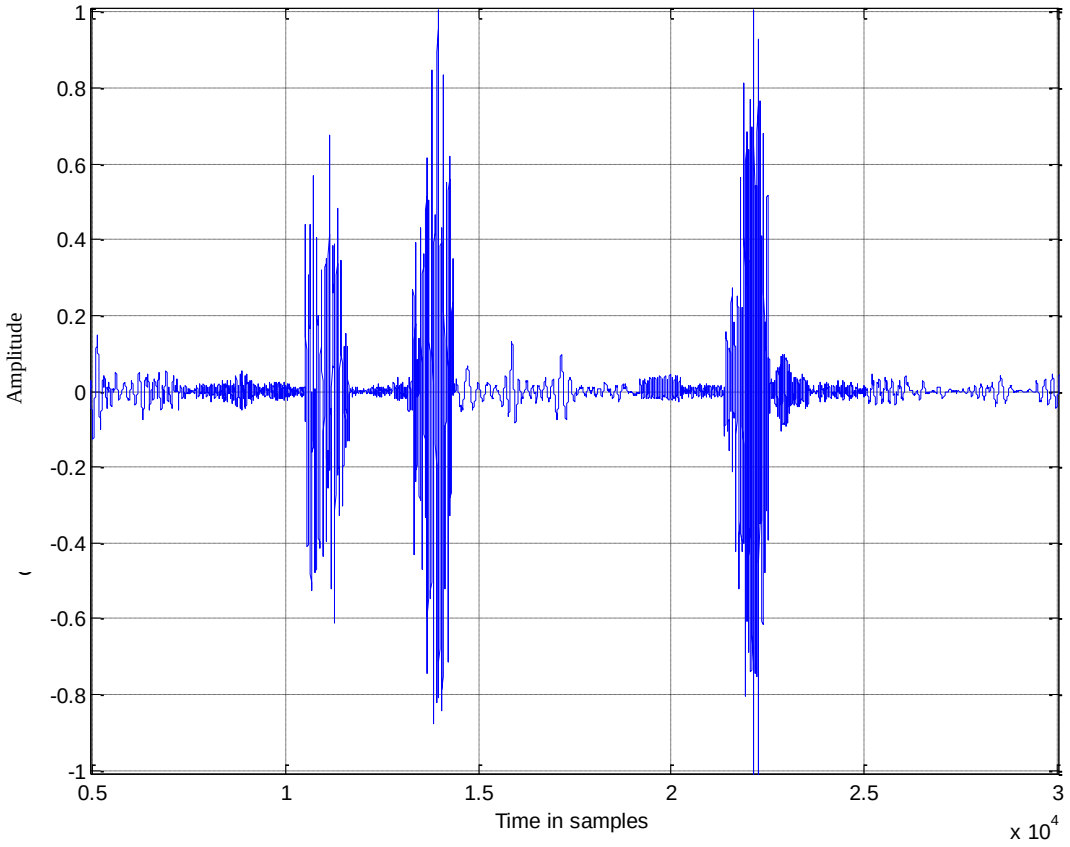

Figure 5.5-3 Particle signals after PASB filtering. (51)

3. After PASB, the particle signals are shown in the form of a pulse period of high frequency with relatively large amplitude. Figure 5.5-3 shows 3 detected particle signals from the original signals in Figure 5.5-1.

4. The SNIR after PASB processing can be roughly estimated as the same method as in item #2.

    I. Measure the highest particle signal amplitude (peak to peak) in Figure 5.5-3.

$$\mathrm{AmpOfPar}_{\mathrm{pp}} = 2.0$$

    II. Measure the highest vibration signal amplitude (peak to peak) in Figure 5.5-3.

$$\mathrm{AmpOfVib}_{\mathrm{pp}} = 0.30$$

III. Calculate SNIR after PASB filtering.

$$\mathrm{SNIR}_{\mathrm{after}} = \frac{\mathrm{AmpOfPar}_{\mathrm{pp}}}{\mathrm{AmpOfVib}_{\mathrm{pp}}} = \frac{2.0}{0.30} = 6.7 = 13.6\mathrm{dB} \quad (5\text{-}5\text{-}3)$$

5. The SNIR gain (or difference in dB) can then be estimated for the PASB method:

$$\mathrm{SNIR}_{\mathrm{before}} = \frac{\mathrm{SNIRdB}_{\mathrm{ch1}} + \mathrm{SNIRdB}_{\mathrm{ch2}}}{2} = \frac{-6.0\mathrm{dB} + 0.21\mathrm{dB}}{2} = -3.0\mathrm{dB} \quad (5\text{-}5\text{-}4)$$

$$\mathrm{SNIR}_{\mathrm{gain}} = \mathrm{SNIR}_{\mathrm{after}} - \mathrm{SNIR}_{\mathrm{before}} = 13.6 - 3.0 = 16.6\mathrm{dB} \quad (5\text{-}5\text{-}5)$$

6. In spite of the rough measurement of the signal amplitude, the SNIR gain reflects the ability of the PASB method to filter out vibrations.

Now we consider another case where vibration signals are comparable to particle signals on average (referred to as Example 2). Figure 5.5-4 is the original signal (with a zoomed version showing the first four particles in Figure 5.5-5). Figure 5.5-6 is the signal after PASB filtering. This time, the PASB method effectively captures 6 particle signals from the vibration signals. As the first part of the vibration signal between time $0.5 - 1 \times 10^4 \mathrm{T_s}$ does not contain a particle signal, it is attenuated by the PASB filter.

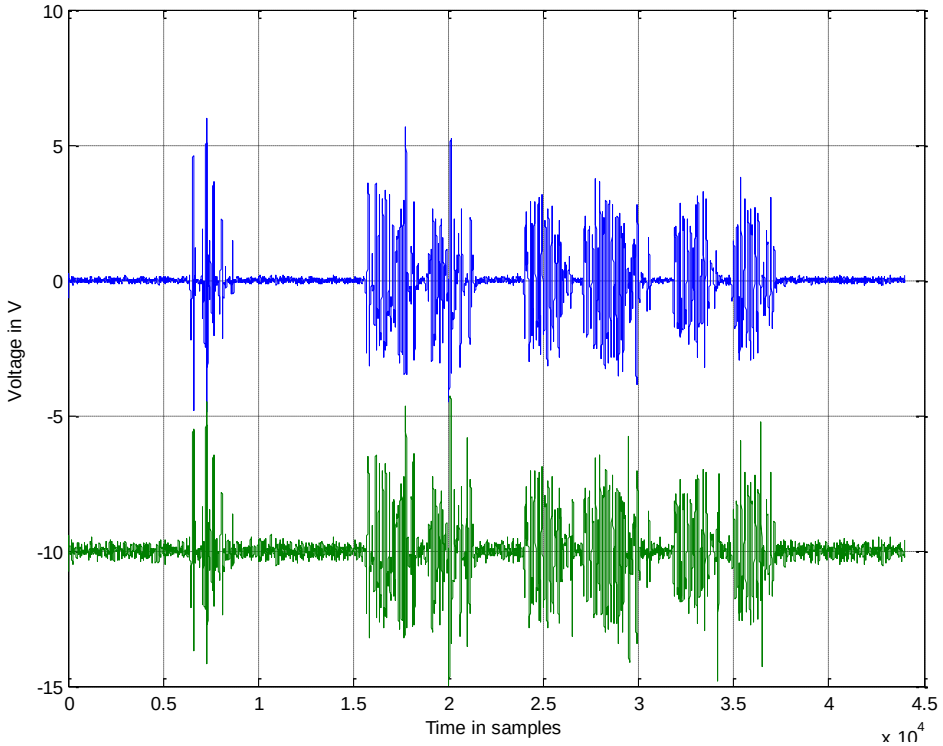

Figure 5.5-4 Particle signals before PASB filtering. (52)

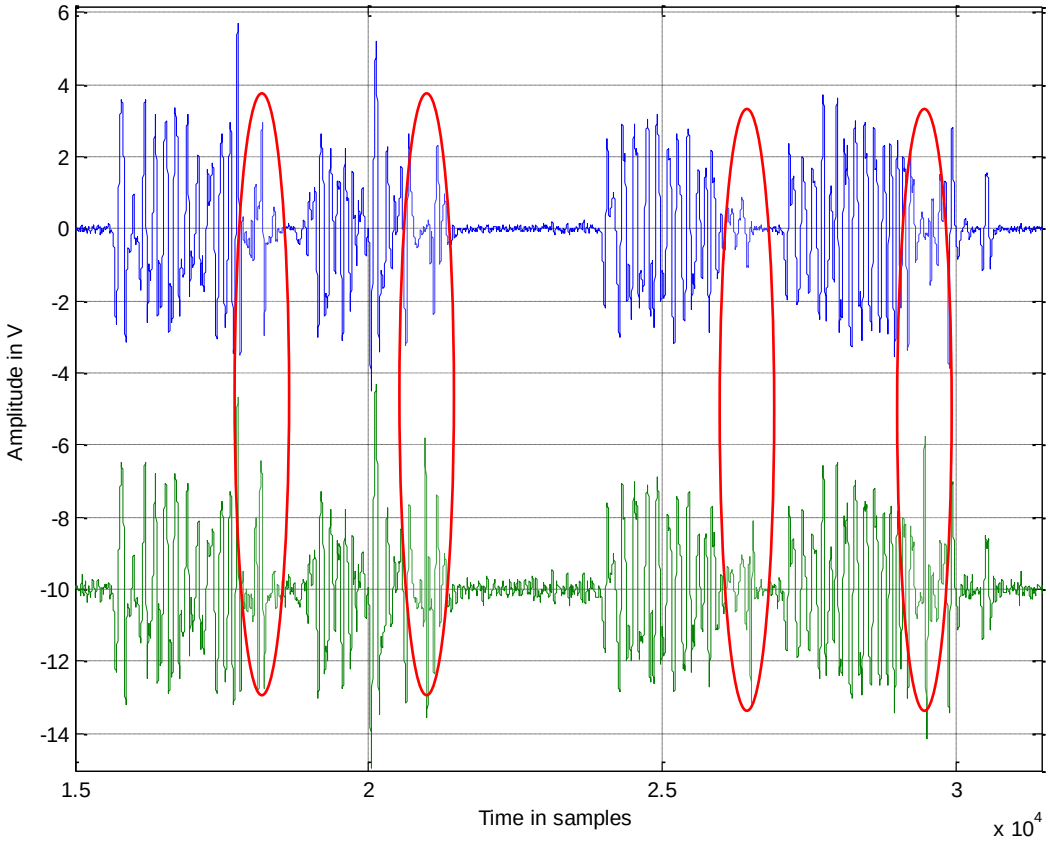

Figure 5.5-5 Details of the particle signals for the first four particles (53)

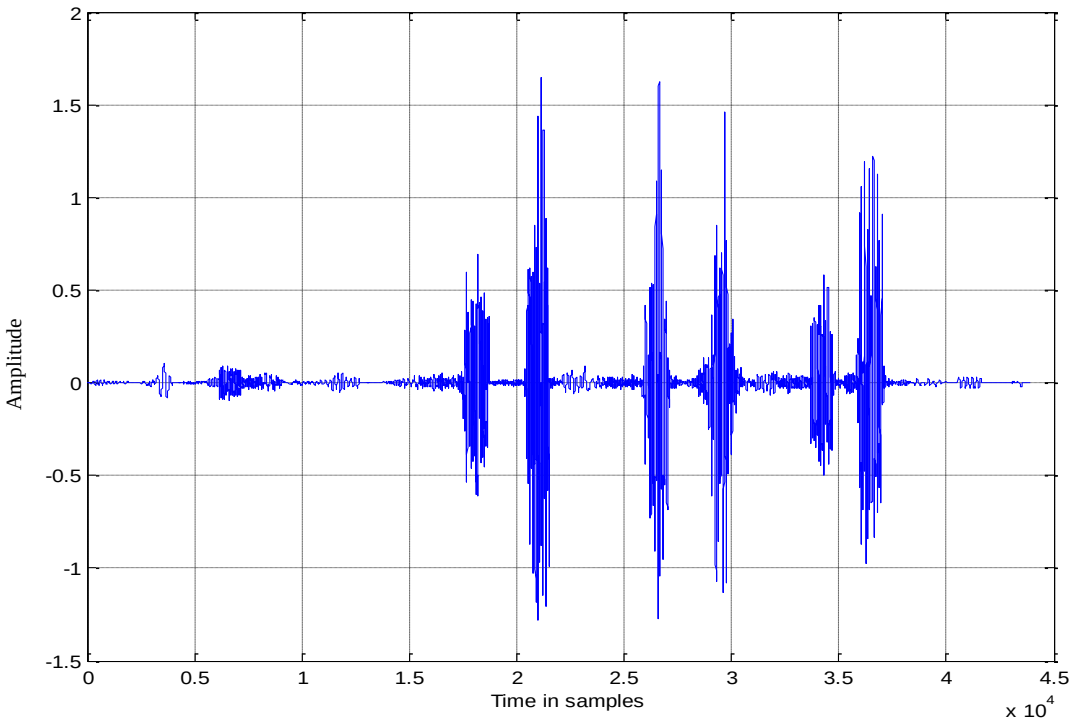

Figure 5.5-6 Particle signals after PASB filtering (54)

We now estimate the SNIR gain for Example 2. The Signal to Noise and Interference Ratios before PASB filtering are

$$\mathrm{SNIR}_{\mathrm{ch1}} = \frac{4.5}{9.0} = 0.50, \qquad \mathrm{SNIR}_{\mathrm{ch1}}^{\mathrm{dB}} = -6.0\mathrm{dB}$$

$$\mathrm{SNIR}_{\mathrm{ch2}} = \frac{8.0}{12.0} = 0.66, \qquad \mathrm{SNIR}_{\mathrm{ch2}}^{\mathrm{dB}} = -3.5\mathrm{dB}$$

The Signal to Noise and Interference Ratio after PASB filtering is

$$\mathrm{SNIR}_{\mathrm{PASB}} = \frac{2.9}{0.10} = 29, \qquad \mathrm{SNIR}_{\mathrm{PASB}}^{\mathrm{dB}} = 29.2\mathrm{dB}$$

The average SNIR gain is accordingly:

$$\mathrm{Gain}_{\mathrm{SNIR}}^{\mathrm{dB}} = \mathrm{SNIR}_{\mathrm{PASB}}^{\mathrm{dB}} - \frac{\mathrm{SNIR}_{\mathrm{ch1}}^{\mathrm{dB}} + \mathrm{SNIR}_{\mathrm{ch2}}^{\mathrm{dB}}}{2} = 29.2\mathrm{dB} - \frac{-6.0 + (-3.5)}{2}\mathrm{dB} = 34\mathrm{dB}$$

5.6 AOA Filtering

In the AOA algorithm introduced in Chapter 3 for particle detection, the phase pattern reflects the relationship between the total power and the phase. For example, a vibration signal and the corresponding phase pattern are illustrated in Figure 5.6-1.

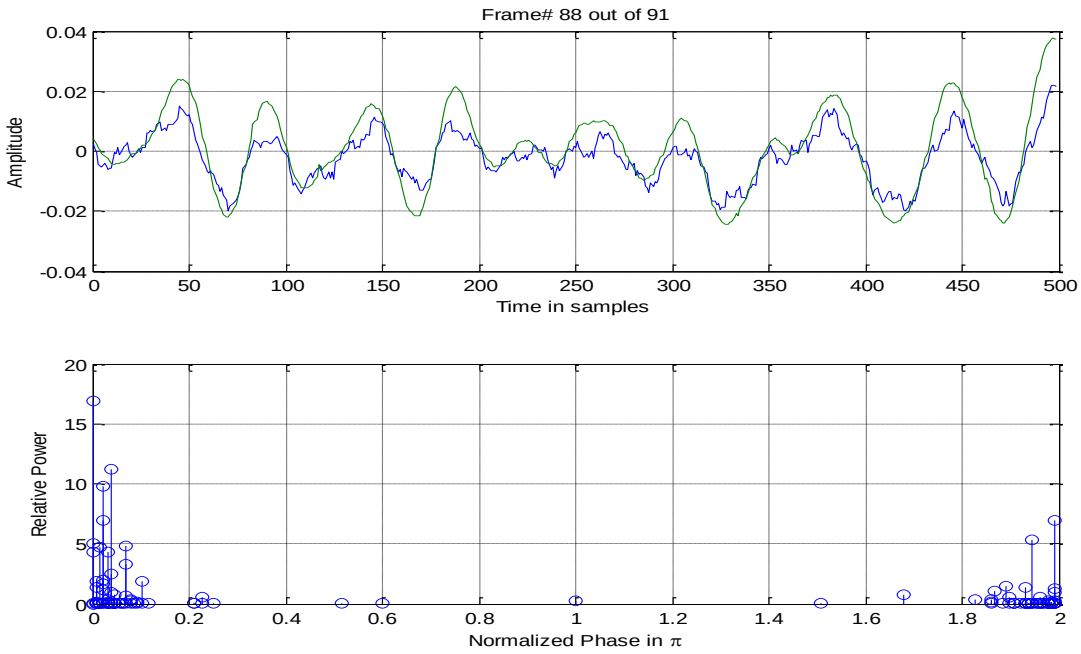

Figure 5.6-1 Vibration signals and the corresponding phase pattern (55)

As a vibration signal has a different phase pattern from a particle signal, it is possible to design a filter to remove the phase components in the phase domain instead of the usual frequency domain. A simply way to achieve this is to select a rectangular phase window, screening out the disqualified phase components. For example, in Figure 5.6-1, most of the vibration components are distributed around 0 or 2 π. In order to filter out the vibration signal, we set the phase filter function as:

$$F(\phi) = \begin{cases} 1 & when\ \phi\ \in (0.2\pi, 1.8\pi) \\ 0 & others \end{cases}$$

where ϕ is the phase difference between the sensor elements.

By using such a filter, most of the vibration signals are filtered out, and the particle signal is preserved.

5.7 Comparison of the Two Methods

The two methods are compared for the case presented below. The original signal contains two particles, and several vibration signal components (Figure 5.7-1).

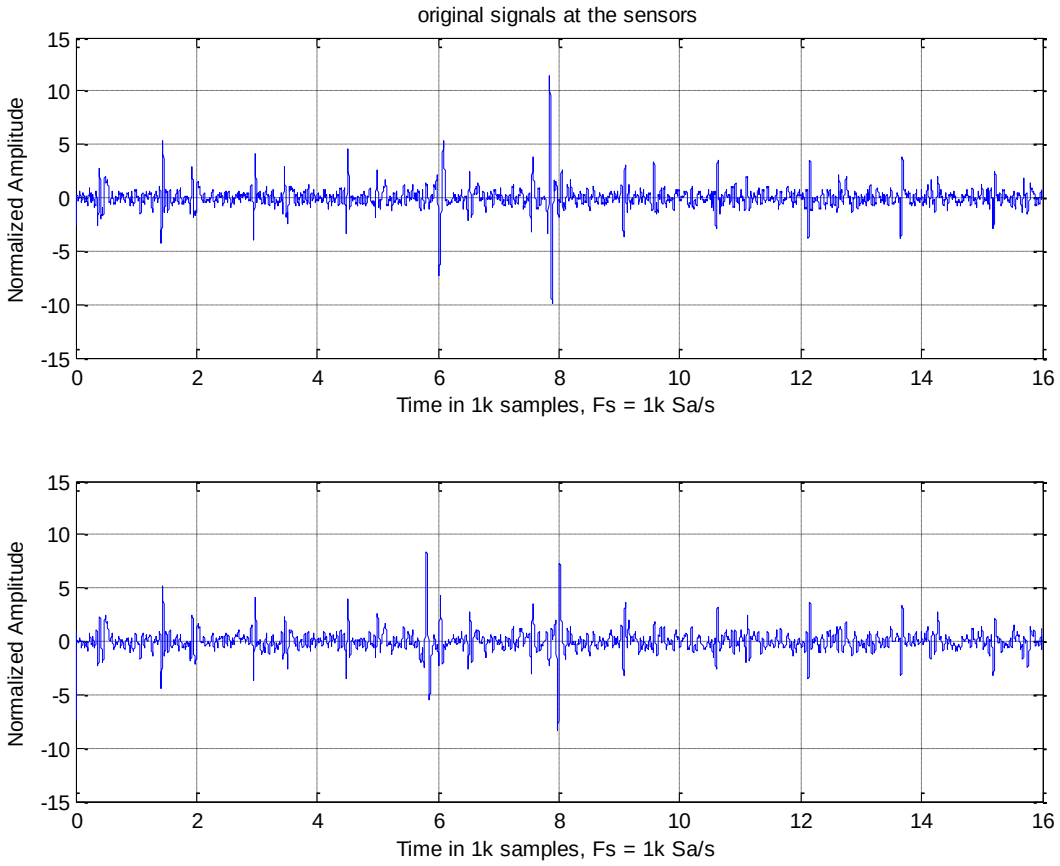

Figure 5.7-1 Original signals in both channels (56)

After the above signal is processed by the AOA filtering method, the result is shown in Figure 5.7-2.

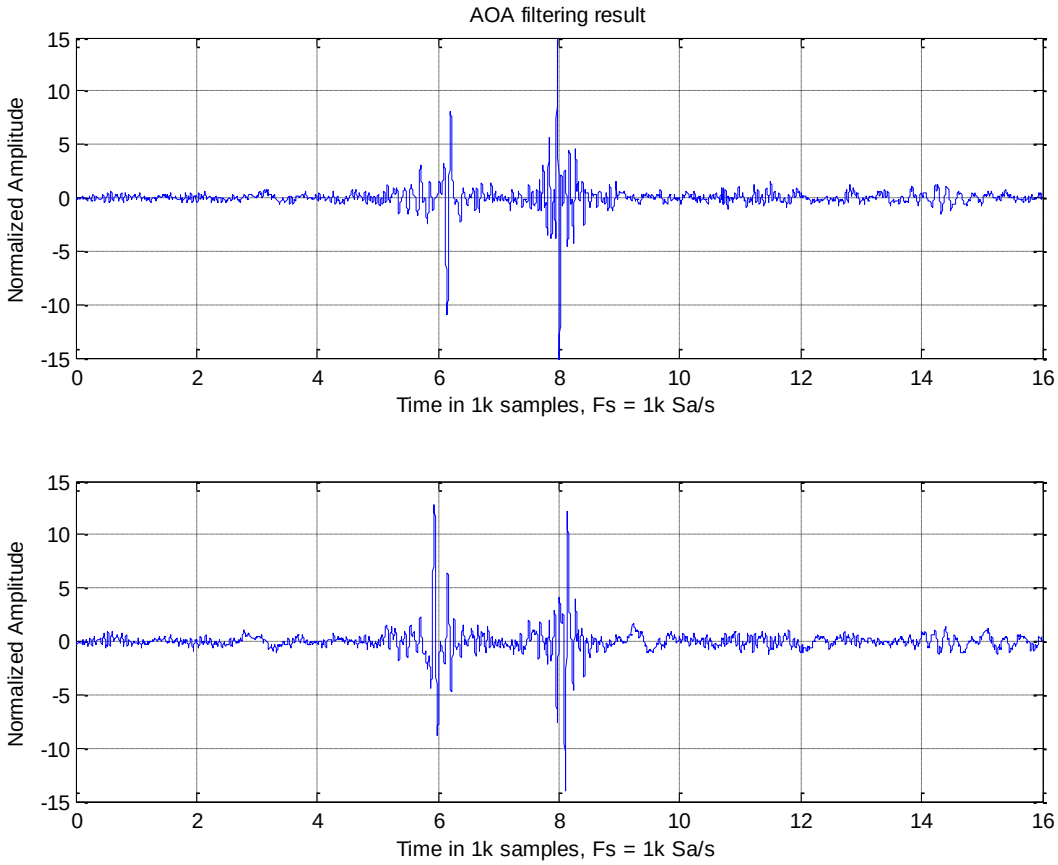

Figure 5.7-2 Outputs of the AOA filtering (57)

This result is a two-channel output, while the PASB method produces a one-channel output. In order to compare them, the two channel signals are multiplied, rectified and low-pass filtered. The final result is a one-channel signal as shown in the second figure of Figure 5.7-3.

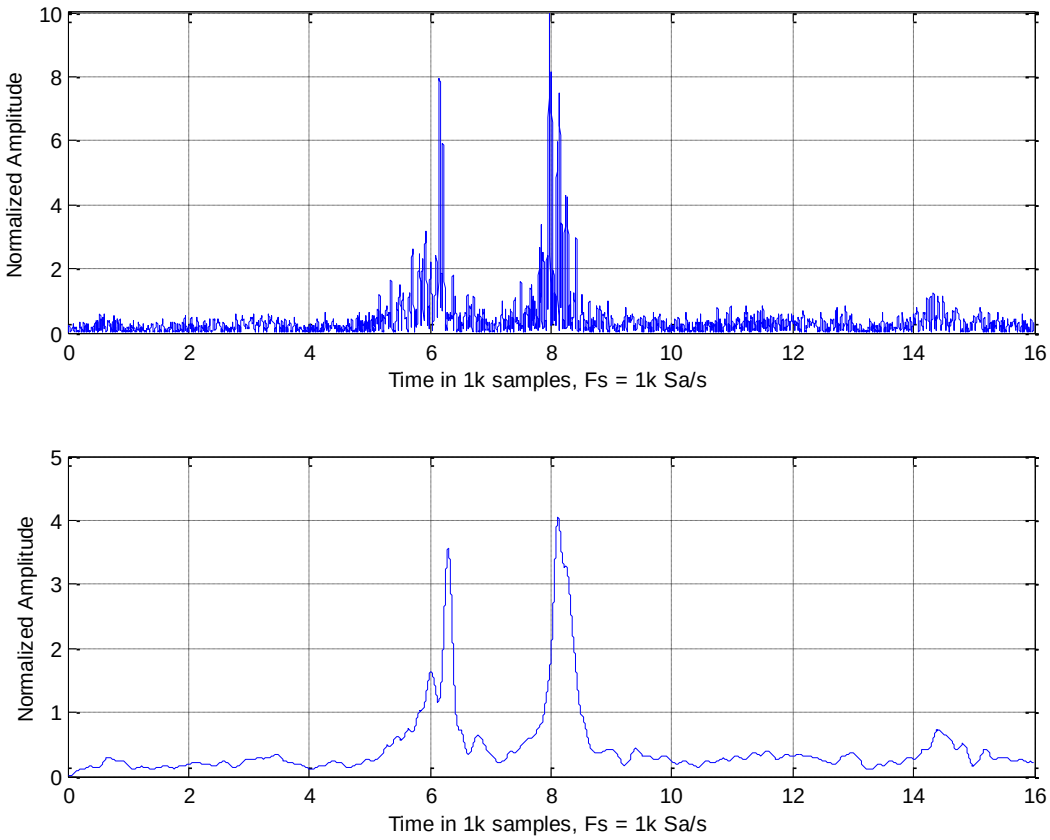

Figure 5.7-3 Particle signals after multiplied, rectified and low-pass filtered process (58)

For the PASB filtering, the output is already one channel. After rectification and low-pass filtering, the PASB final result is shown in the second figure of Figure 5.7-4.

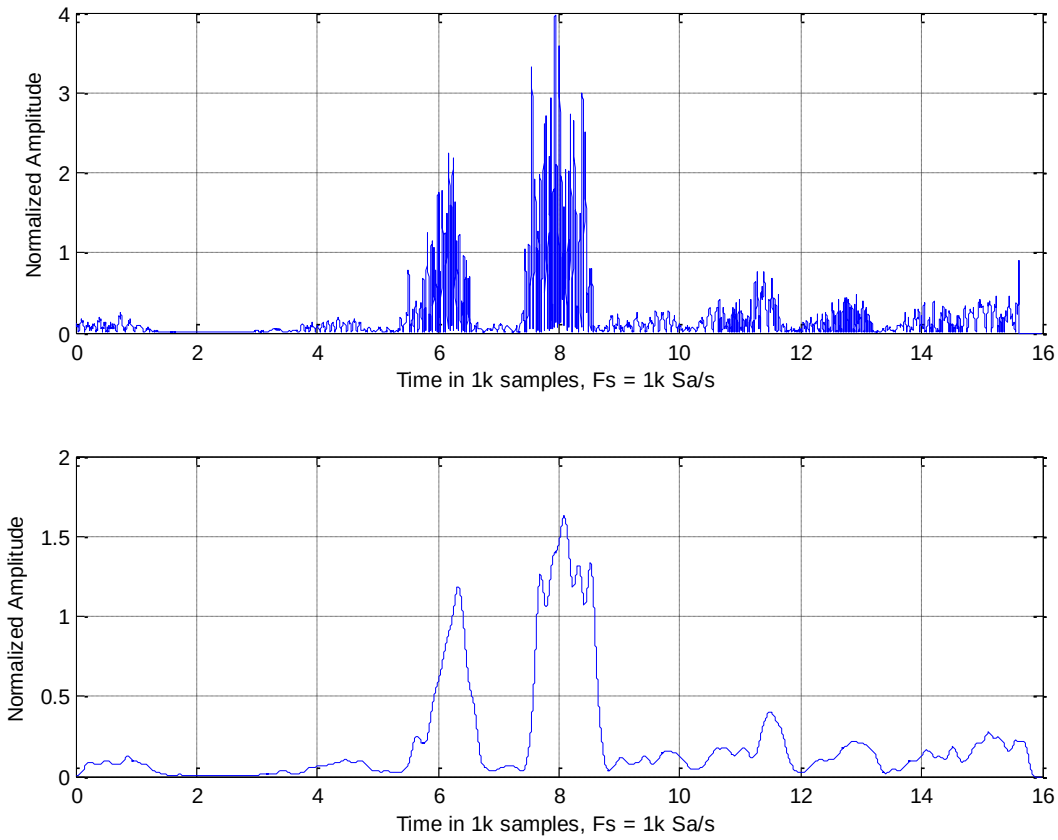

Figure 5.7-4 Particle signals after PASB filtering (59)

The output SNIR obtained with the two methods are:

AOA filtering: SNIR $= \frac{4}{0.8} = 5.$

PASB filtering: SNIR $= \frac{1.6}{0.4} = 4.$

By comparing Figures 5.7-3 and 5.7-4, some similarities and differences can be observed between the two methods.

Similarities:

1. Both the AOA and PASB filtering methods have detected the two particles as large pulses.

2. Both can capture the particles during the period between 6000 and 8000 samples.

3. Both methods indicate that the second particle has more energy than the first one.

Differences:

1. The particle duration time captured by the AOA filtering method is more accurate than that of the PASB.

2. The output SNIR of the AOA filtering is slightly larger than that of the PASB filtering in this scenario.

Those two differences suggest that the AOA filtering method can be as good or even superior to the PASB beamforming method in vibration filtering.

5.8 Conclusion

The PASB beamforming and the AOA filtering method were introduced and adapted in this chapter for the application of ODM. The experimental results show that both methods can effectively capture the particle signals under an environment with vibration interferences. The experiments also demonstrated that both the PASB method and the AOA filtering method can significantly improve the SNIR for all the cases considered. They can therefore help to detect particle signals more accurately. When comparing both methods, the AOA filtering method was slightly superior to the PASB beamforming method, both in accurately capturing the particles duration in time and in filtering the vibration signals.

However, both methods also have their weaknesses. Firstly, they distort the original particle signal. Originally, a particle signal resembles a single-period sinusoidal signal. After PASB or AOA filtering, it often becomes a single longer pulse. Secondly, the resolution on the number of detected particles is degraded from this larger width of the pulses. If two particles are closely passing the sensor, both methods may not be able to distinguish them. Therefore, more refinements to the PASB and AOA-filtering methods may be required before they can directly be used to estimate the type and size of metallic particles sensed by ODM systems. Nevertheless, both methods can definitely help to detect the presence of a particle under a strong vibration interference. Furthermore, both methods can help to estimate the mass of a particle passing the sensor, by measuring the pulse power in the output signal produced by the methods.

Chapter 6 Conclusion

6.1 Summary

In the electromagnetic ODM application, vibration is a problem that interferes with accurate ODM measurements. Much of the previous work on ODM sensors has been done on the cyclic vibration interference. However, the study of random vibration interferences removal has been very limited. This thesis proposes a novel structure and three algorithms to detect particle signals under random vibration interference. The results of the experiments from the prototype show that the particle signals interfered by random vibrations can be detected through the proposed methods, especially the method from Chapter 5 (PASB and AOA filtering).

The ODM sensitivity to vibrations is largely because of the mechanical structure, the amplitude demodulation mode, the high amplifier gain, and the distribution of the electromagnetic field in the ODM system. Based on present MetalScan ODM structure, the sensitivity to vibration can't be reduced. The vibration interference in ODM sensors may happen in random, lasting in variable durations. For example, an automobile riding on a rough road, a vessel boat sailing on an ocean wave, and an airplane flying in storms, will all cause random vibrations. If a sensor is installed on such transportation vehicles, the random vibration problem cannot be avoided. A sensor built with a single coil group such as the MetalScan sensor from GasTop may not be able to handle this issue effectively because it lacks the ability to extract a vibration signal or a particle signal from the sensor output when the vibration signal intensity is comparable to that of a particle signal.

It is reasonable to design a new structure and create a criterion to distinguish a vibration from a particle signal. This thesis adopted a dual-channel structure, and developed three algorithms (AOA, TDOA and PASB) to cope with the problem. The dual-channel structure, instead of the previous single-channel structure, was shown to be effective by making use of beamforming algorithms similar to those used in adaptive antennas in RF communication applications. The

new prototype, with the corresponding developed algorithms, can distinguish a vibration signal and a particle signal by their phase differences or TDOA. This is possible because vibration is a common interference for both channels in the system and it does not cause a phase delay between the sensor signals, whereas a particle introduces a phase delay at the sensor outputs. This observation is the core of the design.

The AOA detection algorithm is designed to distinguish a vibration signal and a particle signal in the frequency domain. The principle of the algorithm is to seek the optimal phase difference for each frequency component of the two channel signals. For a vibration signal, the phases of the two channels for each frequency component are nearly identical. But for a particle signal, the phases of the two channels for each frequency component are mostly non-zero and they are distributed in the range of (0 2π]. According to the described phase character, AOA can capture a particle signal through phase scanning frame by frame.

The TDOA detection algorithm provides a method to measure the time difference of a particle passing through the two sensor elements. The main task of the TDOA algorithm is not to indicate a particle signal, but to validate a particle signal. For the oil flowing in the ODM tube at a given range of speed, the time difference that a particle can produce also fits in some range. The TDOA method can accurately measure the delay that a particle produces. If the measured time is out of the range, then the particle signal is not real. Hence, the TDOA method provides a way to validate a particle signal under weak interference. However, for high interference the TDOA method may not be effective to measure the time difference of a particle signal.

The PASB and AOA filtering algorithms are designed to filter out the vibration signal and to increase the SNIR at the algorithm output. The PASB adopts the beamforming technology, using a specially designed beamformer (beam pattern) to increase the signal strength at some angle of arrival, while attenuating the signal at others. Since the phase difference of a vibration signal is at a zero angle and the phase difference of a particle signal is at a non-zero angle, a special

beamformer is designed to amplify the signals whose angle of arrival is at 0.5 π (assuming without loss of generality that the power of a particle signal focuses on this direction, this could be adjusted in practice based of the typical TDOA of particles in a given setup, the distance between sensors, etc.). The beamformer also attempts to attenuate the zero and π angle signals, corresponding to simultaneous vibration signals received at both sensors (with same or opposite polarity). The AOA filtering algorithm comes from the previously mentioned AOA detection algorithm. In the AOA detection algorithm, a phase pattern is generated on a frame by frame basis and a phase filter is created by setting a screening window to remove the unwanted phase components. In the experimental testing of the PASB and AOA filtering methods, both of them showed the ability to detect the particle signals under vibration interference. When comparing the two methods, the AOA filtering method was found to be slightly superior to the PASB method in the considered experiment.

6.2 Future Work

As mentioned in Chapter 5 both PASB and AOA filtering methods have some drawbacks. When they boost a particle signal, they also distort the signal appearance. Originally a particle signal looks like a full period of sinusoidal signal. After PASB or AOA processing, it results in a longer pulse. Secondly, when two particles closely pass the sensors, the resulting two longer pulses may overlap and become a single pulse, thus making the detection of the individual pulses very difficult. These drawbacks could be improved in future investigation.

Bibliography

1. Bozchalooi, I.S. and M. Liang, *In-line identification of oil debris signals: an adaptive sub-band filtering approach*. Measurement Science and Technology 2010. **21**(1): p. 015104.
2. Bozchalooi, I.S. and M. Liang, *Oil debris signal analysis based on empirical mode decomposition for machinery condition monitoring*, in *American Control Conference* 2009, IEEE. p. 4310-4315.
3. Bozchalooi, I.S. and M. Liang, *Enhancement of the signals collected by oil debris sensors*, in *American Control Conference* 2008, IEEE. p. 2810-2815.
4. Dempsey, P.J., *Investigation of tapered roller bearing damage detection using oil debris analysis*, in *Aerospace Conference* 2006, IEEE.
5. Du, L., *A high throughput inductive pulse sensor for online oil debris monitoring,".* Tribology International, 2011. **44**(2): p. 175 - 179.
6. Messinger, G.S. and F.R. Dube, *Rolling Element-Bearing Failure Detection with ODM On-Line Oil Debris Sensor*, IMR-MCM-CTR-20, Feb. 1995, National Research Council of Canada (NRCC) Technical Report.
7. Allison, M., *Filter debris analysis for aircraft engine and gearbox health management.* Failure Analysis and Prevention, 2008. **8**(2): p. 183 - 187.
8. Edmonds, J., *Detection of precursor wear debris in lubrication systems*, in *Aerospace Conference Proceedings* 2000. p. 73 - 77.
9. Fan, H., *study on oil detection technology based on inductive wear debris sensor*, in *ICEMI '09.9th International Conference on Electric Measurement & Instruments.* 2009, IEEE p. 810-813.
10. Fan, H., *Design and noise control of the portable wear debris concentration detector*, in *Measuring Technology and Mechatronics Automation* 2009, ICMTMA '09. p. 206-209.
11. Freese, E. and J.M. Rostoskey, *In-situ oil analyzer and methods of using same, particularly for continuous on-board analysis of diesel engine lubrication systems*, 1997: U.S. Patent 5604441.
12. Zhe, J., *A micromachined high throughput coulter counter for bioparticle detection and*

counting Micromechanics and Microengineering 2007. **17**: p. 304 - 313.

13. Zhang, J., *Monitoring of lubricant film failure in a ball bearing using ultrasound.* Tribology 2006. **128**: p. 612 - 618.
14. Wu, S. and T. Chow, *Introduction Machine Fault Detection Using SOM-Based RBF Neural Networks.* IEEE Transactions on Industrial Electronics 2004. **51**(1): p. 183.
15. Tucker, J.E., *LASERNET FINES optical wear debris monitor*, in *International Conference on Condition Monitoring*, M.H. Jones, Editor 1999: Swansea, UK. p. 445 - 452.
16. Sarangi, M.A., *Oil Debris Detection Using Capacitance and Ultrasonic Measurements*, Aug. 2007, University of Akron: Master Thesis.
17. Dupuis, R., *Oil debris monitoring for mitigating revenue and cost risks associated with gearbox unreliability*, in *7th World Wind Energy Conference (WWEC)* 2008: Kingston, ON. .
18. Miller, J.L., *In-line oil debris monitor for aircraft engine condition assessment*, in *IEEE Aerospace Conference Proceedings* 2000, IEEE. p. 49 - 56.
19. GasTop_Documentation, *GasTop MetalSCAN Specifications, C001376, Rev. 5*, C. GasTop Ltd, www.gastops.com, Editor 2005.
20. Fan, H., *Study on magnetic characteristic of ferromagnetic wear debris in inductive wear debris sensor.* Tribology, 2009. **29**(5): p. 452 - 457.
21. Flanagan, I.M., *Inductive method for estimating the composition and size of metal particles.* Measurement Science and Technology, 1990. **1**(5): p. 381 - 384.
22. Yin, Y.-h., *Study on the magnetic field homogeneity of wear debris detector.* Tribology, 2001. **21**(3): p. 228 - 231.
23. Yin, Y., *Design of the inductive transducer of wear particle monitoring.* Journal of Transducer Technology, 2003. **22**(7): p. 36 - 38.
24. Hoole, P., *Smart antennas and signal processing for communications, biomedical, and radar systems* 2001, Southampton; Boston: WIT Press. 304.
25. Van_Trees, H.L., *Detection, Estimation, and Modulation Theory* 2001, New York: Wiley.

26. Sander, D., *An optical comparator for particle detection*, in *IEEE on Sensors* 2008. p. 347 - 350.
27. Rheims, J., *Sizing of inhomogeneous particles by a differential laser Doppler anemometer.* Measurement Science and Technology, 1999. **10**(2): p. 68 - 75.
28. Myshkin, N.K. and L.V. Markova, *Wear monitoring based on the analysis of lubricant contamination by optical ferroanalyzer.* Journal of Wear, 2003. **255**(7): p. 1270 - 1275.
29. Tu, Q., *Real-time oil monitoring for hydraulic systems based on photoelectricity method.* Construction Machinery and Equipment, 1999(8): p. 833 - 837.
30. Murali, S., *A microfluidic Coulter counting device for metal wear detection in lubrication oil.* Review of Scientific Instruments 2009. **80**(1): p. 016105 - 016105-3.
31. Lu, X.-j., *Finite element analysis of an electromagnetic device of an on-line ferrograph.* Journal of Tribology, 2004. **24**(2): p. 164 - 167.
32. Muir, D. and B. Howe, *In-line Oil Debris Monitor (ODM) for the Advanced Tactical Fighter Engine* in *Aerospace Atlantic Conference* 1996: SAE Paper 961308.
33. Hong, H., *Rotating Machinery Monitoring: Feature Extraction, Signal Separation, and Fault Severity Evaluation*, in *Mechanical Eng.* Dec. 2007, University of Ottawa: PH. D. Thesis.
34. Kempster, R.W. and D.B. George, *Method and apparatus for detecting particles in a fluid having coils isolated from external vibrations*, Nov. 1993, Minister of National Defence (Ottawa, CA) US Patent# 5,444,367.
35. Industrial_documentation, *Sine-on-random vibration testing*, B. Kjar, Editor 2010: DK-2850 Narum Denmark.
36. Whitlock, R.R., *The path to affordable long term failure warning: the XRF-wear monitor*, 1998, Naval Research Lab, ADA348000: Washington DC.
37. Laghari, M.S., *Wear particle shape and edge detail analysis*, in *The 2nd International Conference on Computer and Automation Engineering (ICCAE)* 2010, IEEE CONFERENCES. p. 122 - 125.
38. Roylance, B.J., *Wear debris and associated wear phenomena-fundamental research and practice.* Engineering Tribology 2000. **214**: p. 79 - 105.

39. Ortiz, D., *Combined lubrication monitor for on-line gearbox health assessment*, in *Aerospace Conference* 2011, IEEE. p. 1- 8.
40. Hong, H. and M. Liang, *A fractional calculus technique for on-line detection of oil debris.* Measurement Science and Technology, 2010. **19**(5): p. 055703.
41. Flanagan, M., *An inductive method for estimating the composition and size of metal particle.* Measurement Science and Technology 1990. **1**: p. 381 - 384.
42. Fan, H., *Experimental study of an on-line monitoring sensor for wear particles in oil.* Tribology, 2010. **30**(4): p. 338 - 343.
43. Fan, H., *Magnetic characteristic of unferromagnetic wear debris in inductive wear debris sensor.* Transducer and Microsystem Technologies, 2010. **29**(2): p. 35 - 41.
44. Kitaljevich, D., *Oil debris monitoring for helicopter drivetrain condition based maintenance* in *American Helicopter Society International Condition Based Maintenance Specialists Meeting*2008. p. 163 - 180.
45. Markova, L.V., *Main trends in developing methods and build-in devices for wear diagnosis of tribosystems.* Journal of Friction and Wear, 1996. **17**(3): p. 365 - 370.
46. Han, L., *The key points of inductive wear debris sensor*, in *Fluid Power and Mechatronics (FPM)* 2011. p. 809 - 815.
47. Lee, H.-B., *Efficient magnetic field calculation method for pancake coil using Biot-Savart law,* in *the 12th Biennial IEEE Conference on Electromagnetic Field Computation* 2006. p. 193.
48. Hoang, N.T., *Optimized analog filter designs with flat responses by semidefinite programming.* IEEE Transactions on Signal Processing 2009. **57**(3): p. 944 - 955.
49. Cong, L., *Hybrid TDOA/AOA mobile user location for wideband CDMA cellular systems.* IEEE Transactions on Wireless Communications 2002. **1**(3): p. 439-447.
50. Bocquet, M., *Using enhanced-TDOA measurement for indoor positioning.* IEEE Transactions on Microwave and Wireless Components Letters 2005. **15**(10): p. 612 - 614.
51. Bodea, C., *Shared autocorrelation property of sequences.* IEEE Transactions on Information Theory, 2011(6): p. 3805-3809.
52. Van_Trees, H.L., *Optimum array processing,* 2002, New York: Wiley-Interscience.

1443.

53. Li, W., *Performance evaluation of digital beamforming strategies for satellite communications.* IEEE Transactions on Aerospace and Electronic Systems, 2004. **40**(1): p. 12 - 26.

Appendix A Matlab Code (for reference)

```
%%%%%%%%%%%%%%%%%%%%%%%%%%%%%%%%%%%%%%%%%%%%%%%%%%%%
%Title:  AOA algorithm
%
%%%%%%%%%%%%%%%%%%%%%%%%%%%%%%%%%%%%%%%%%%%%%%%%%%%%

clc; clear all; close all;

Filename = 'Voltage_004.txt';
%Parameters:
FrameSize = 1000; ShiftStep = FrameSize/2;          %FrameSize is the window
to do fft transfer, ShiftStep is the window move forward step
Fs = 1000 ;                                         %Set 1000Hz is the
standard.
FreqDiv = 4;                                        %It means the pi/4, or
Fs/8, Fs/2 = pi;
PowerMin = 0;                                       %The min power
PowerPert= 0.01;                                    %Min power is the 1% of
the average power.
[LongSeriesData1, LongSeriesData2] = textread(Filename, '%f %f',
'headerlines', 7, 'delimiter', ' ');
% Suppose the sampling frequency is 5k sa/sec, change it to 1k sa/sec;
LongSeriesData1 = resample(LongSeriesData1,1,5);LongSeriesData2 =
resample(LongSeriesData2,1,5);

%Filter DC component, The read one is column vector, change it to row
%vector.
LongSeriesData1 = LongSeriesData1 - mean(LongSeriesData1); LongSeriesData2 =
LongSeriesData2 - mean(LongSeriesData2);
LongSeriesData = [LongSeriesData1, LongSeriesData2]';
NLongSeries = size(LongSeriesData,2);

figure(5)
    plot(0:NLongSeries-1, LongSeriesData); grid on;
    xlabel('Samples in time');ylabel('Voltage in V');

NFrames = floor((NLongSeries - FrameSize)/ShiftStep) +1;

if NFrames ~= ((NLongSeries - FrameSize)/ShiftStep)
    NZeros = NFrames*ShiftStep +FrameSize - NLongSeries;
    LongSeriesData = [LongSeriesData, zeros(2,NZeros)];
end;

NyData_final = length(LongSeriesData);
yData_final = zeros(1,NyData_final);
%With every step, find correlation matrix for every step.

k0 = 1;
```

```
StopFrame = NFrames;                                % NFrames
for k = 1:StopFrame
    Frame_begin = k0+(k-1)*ShiftStep; Frame_end = Frame_begin+FrameSize-1;
    Frame_k = LongSeriesData(:,Frame_begin: Frame_end);
    %The present estimation
    [Sx_freq_k] = Fun_A040_FourierTrans(Frame_k, FreqDiv);
    Sx_est = Sx_freq_k(1:4,:);

    %Find the optimal phase for each frequency
    [PPD] = Fun_B030_PhaseScan(Sx_est);

    %Find
    NPPD = length(PPD);             %The length only stands for pi/FreqDiv
    %NPPD is the same as the length of Sx_est.
    PowerAvg = mean(PPD(1,:));          %Mean power is for statistics
    [PowerMax, Freq_indice] = max(PPD(1,:)); Freq_PMax = ((Freq_indice -
1)/(NPPD-1))*Fs/(2*FreqDiv);
    F = 0: NPPD-1;
    Freq = F/(NPPD-1)*Fs/(2*FreqDiv);
%
    figure(1);
    subplot(2,1,1);
    plot(0:length(Frame_k)-1, Frame_k);grid on;
    title(['Frame# ', num2str(k),' out of ',num2str(NFrames)]);
    xlabel('Time in samples'); ylabel('Amplitude');
    subplot(2,1,2);
    stem(PPD(2,:), PPD(1,:));grid on;
    xlabel('Normalized Phase in \pi');ylabel('Relative Power');
    pause on; pause(1);

%
end;
```

```
%%%%%%%%%%%%%%%%%%%%%%%%%%%%%%%%%%%%%%%%%%%%%%%%
% Title: TDOA algorithm
%
%%%%%%%%%%%%%%%%%%%%%%%%%%%%%%%%%%%%%%%%%%%%%%%%

clear all; close all; clc;

%Read data from the file
Filename = 'Vibration_Particle_001.txt';
[Ch1, Ch2] = textread(Filename, '%f %f', 'headerlines', 7, 'delimiter', ' ');
%Those data are sampled at 5k Hz, in col vector

% Sampling Frequency
Fs = 5000; Ts = 1/Fs;
DataLen = length(Ch1);
Time = (0:(DataLen-1));

%Figure(1) to show the orignal data
figure(1);
subplot(2,1,1);
plot(Time,Ch1);grid on;
subplot(2,1,2);
plot(Time,Ch2);grid on;

%Define the Window length and TDOA
Win_len = 2000;              %0.4sec, just hold one particle signal
Win_shift = 1000;            %Window advance step
Max_tdoa = 2000;             %0.16sec, in Ts. Ts = 0.2ms
TDOA_len = Max_tdoa + Win_len;

%nb of windows of TDOA
NB_wins_tdoa = floor((TDOA_len - Win_len)/Win_shift) +1 ;%The window movement
won't break through the end limit. it's safe
NB_wins_data = floor((DataLen - Win_len - (Max_tdoa + Win_len))/Win_shift) +1
;   %the whole data windows

%Correlation window length is ch1: Win_len, and ch2: the chopped TDOA_len, =
Win_len + (NB_wins_tdoa-1)*Win_shift
TDOA_actual_len = Win_len + (NB_wins_tdoa - 1)*Win_shift;
Corr_len = 2*Win_len + (NB_wins_tdoa - 1)*Win_shift -1;
Max_yx_corr = zeros(1, Corr_len);

%Suppose Ch2 is lagging behind Ch1, Ch1 is the base.
for  Win_index1 = 1:NB_wins_data
    Ch1_start = 1 + (Win_index1 -1)* Win_shift;
    Ch1_end = Ch1_start + Win_len -1;
    %Ch2 window relatively moves referring on Ch1 window
    for Win_index2 = 1:NB_wins_tdoa
        Ch2_start = Ch1_start + (Win_index2 -1)*Win_shift;
        Ch2_end = Ch2_start + Win_len -1;
        %Filter out DC in each frame
```

```
        Ch1_frame = Ch1(Ch1_start:Ch1_end);Ch1_frame = Ch1_frame -
mean(Ch1_frame);
        Ch2_frame = Ch2(Ch2_start:Ch2_end);Ch2_frame = Ch2_frame -
mean(Ch2_frame);
        %Before FFT, Ch1_frame must padding zeros with length Win_len -1;
        %They are col vector
        Ch1_fft = fft([Ch1_frame; zeros(Win_len-1,1)]);
        Ch2_fft = fft([Ch2_frame; zeros(Win_len-1,1)]);
        %Power Spectrum in frequency
        Ch1_auto = conj(Ch1_fft).*Ch1_fft;
        Ch2_auto = conj(Ch2_fft).*Ch2_fft;
        Ch1Ch2_cross = conj(Ch1_fft).*Ch2_fft;
        %Using GCC, the unit in Ts, not second
        [YX_corr, Lags, R] = GCC('unfiltered', Ch1_auto, Ch2_auto,
Ch1Ch2_cross,1, Win_len);
        YX_corr = abs(fftshift(YX_corr'));
        %Here we only care YX_corr, which window has 2Win_len -1 long.
        %Using overlap+max method to fill the Max_yx_corr window
        Cwin_start = 1 + (Win_index2 - 1)*Win_shift ;
        Cwin_end = Cwin_start + 2*Win_len -2 ;
        %Why not use add method, because it will attenuate the useful
        %signal with many average. Our method is to capture the max value
        %during a period time.
        Max_yx_corr(Cwin_start:Cwin_end) =
max(Max_yx_corr(Cwin_start:Cwin_end), YX_corr);
    end;
end;

%Normalize the cross correlation
Max_yx_corr = Max_yx_corr/max(Max_yx_corr);
Max_yx_corr_dB = 20*log10(Max_yx_corr);

%Pay attention to time coordinator
%It is from -Win_len+1 to TDOA_actual_len, which is Corr_len - Win_len
Time = -Win_len+1:Corr_len-Win_len;     % in Ts
figure(2);
subplot(2,1,1);
plot(Time, Max_yx_corr); grid on;
subplot(2,1,2);
plot(Time, Max_yx_corr_dB); grid on;
```

```
%%%%%%%%%%%%%%%%%%%%%%%%%%%%%%%%%%%%%%%%%%%%%%%%%%%%
% Title: PASB algorithm
%
%%%%%%%%%%%%%%%%%%%%%%%%%%%%%%%%%%%%%%%%%%%%%%%%%%%%

% In a frame, generate multiple signals for a linear array

clc; clear all; close all;

% [x1, x2] = Data_GenFun();

Filename = 'Voltage_007.txt';  %From file text
[x1, x2] = textread(Filename, '%f %f', 'headerlines', 7, 'delimiter', '
');%col vector
x1 = resample(x1,1,5); x2 = resample(x2,1,5);
DataLen = length(x1);
x1 = x1 - mean(x1); x2 = x2 - mean(x2);
x1 = x1/sqrt(var(x1));x2 = x2/sqrt(var(x2));



samp_freq=1000;
x=x1-mean(x1);
y=x2-mean(x2);

[xp,yp]=FilteroutVibrationByAOA_2(x,y,samp_freq);  % pre-processing, Ritch's
method, for rms estimation of particle signal (can also be used as basis for
TDOA estimation)

signal_length=length(x);

t=(0:1:signal_length-1)/samp_freq;
figure(1);
subplot(2,1,1);
plot(t,x); grid on;
title('original signals at the sensors');
xlabel('Time in 1k samples, Fs = 1k Sa/s');
ylabel('Normalized Amplitude');
axis_copy=axis;
axis([axis_copy(1) axis_copy(2) -15 15])
subplot(2,1,2);
plot(t,y); grid on;
xlabel('Time in 1k samples, Fs = 1k Sa/s');
ylabel('Normalized Amplitude');
axis_copy=axis;
axis([axis_copy(1) axis_copy(2) -15 15])

figure(2)
subplot(2,1,1);
plot(t,xp); grid on;
title('signals at the output of Ritch`s pre-processing');
xlabel('Time in 1k samples, Fs = 1k Sa/s');
ylabel('Normalized Amplitude');
```

```
axis_copy=axis;
axis([axis_copy(1) axis_copy(2) -15 15]);
subplot(2,1,2);
plot(t,yp); grid on;
xlabel('Time in 1k samples, Fs = 1k Sa/s');
ylabel('Normalized Amplitude');
axis_copy=axis;
axis([axis_copy(1) axis_copy(2) -15 15])

figure(3);
zp = sqrt(abs(xp.*yp));
subplot(2,1,1);
plot(t,zp); grid on;
xlabel('Time in 1k samples, Fs = 1k Sa/s');
ylabel('Normalized Amplitude');
axis_copy=axis;
axis([axis_copy(1) axis_copy(2) 0 10]);

subplot(2,1,2);
M = 251; f_cut = 1; Fcut = 2*f_cut/samp_freq;            %Fcut normalized
frequency
b = fir1(M, Fcut);
zp1 = filter(b,1,zp);
plot(t,zp1); grid on;
xlabel('Time in 1k samples, Fs = 1k Sa/s');
ylabel('Normalized Amplitude');
axis_copy=axis;
axis([axis_copy(1) axis_copy(2) 0 5]);



x = [x1, x2];

%Parameters:
FrameSize = 256; ShiftStep = FrameSize/2;          %FrameSize is the window
to do fft transfer, ShiftStep is the window move forward step
Fs = 1000 ; Ts = 1/Fs;  N = 40;     %N array elements; Fs sampling frequency.
nbFFT = 1024;nbFFT_P = nbFFT/2; BW = 50; Duty = BW/Fs;
%Hanning Window for frames
Hann_win = hann(FrameSize);

%LowPass Filter
M = 251; f_cut = 50; Fcut = 2*f_cut/Fs;            %Fcut normalized frequency
b = fir1(M, Fcut); b = b';
B_FFT = fft(b, nbFFT); B_half = B_FFT(1:nbFFT_P);
% x1 = filter(b,1,x1); x2 = filter(b,1,x2);
% x=[x1,x2];

% figure(1)
%     plot(0:DataLen-1, [x(:,1), x(:,2)-10]); grid on;
%     xlabel('Time in samples');ylabel('Voltage in V');
%
```

```
%


nb_frames = floor((DataLen - FrameSize)/ShiftStep)+1;
DataLen_real = FrameSize + (nb_frames-1)*ShiftStep;
y_out_frame = zeros(nbFFT,1);
y_out = zeros(DataLen_real,1);

for k = 1:nb_frames
    fr_start = 1 + (k-1)*ShiftStep;
    fr_end = fr_start + FrameSize -1;
    fr_k = x(fr_start:fr_end,:);
    fr_k = [fr_k(:,1).*Hann_win, fr_k(:,2).*Hann_win];
    fr_k = [fr_k(:,1) - mean(fr_k(:,1)), fr_k(:,2) - mean(fr_k(:,2))];

    % Fourier Transfer
    Fr_k = fft(fr_k, nbFFT);
    Fr_abs = abs(Fr_k); Fr_phase = [angle(Fr_k(:,1)),angle(Fr_k(:,2))];
    Fr_Pwr = Fr_abs(:,1).^2 + Fr_abs(:,2).^2; Fr_Amp = sqrt(Fr_Pwr/N);
%     Amplitude = sqrt(Fr_Pwr(1:100)) %For Test.
    %Phase Extention
    Phase_step = Fr_phase(:,2)- Fr_phase(:,1) ;
    Phase_array = zeros(size(Fr_k,1),N); Phase_array(:,1:2) = Fr_phase;
    for l = 3:N
        Phase_array(:,l) = Phase_array(:,1)+(l-1)*Phase_step;
    end;

    %Extension data
    CPLX_array = zeros(size(Phase_array));
    for l = 1:N;
        CPLX_array(:,l) = Fr_Amp.* exp(j*Phase_array(:,l));
    end;
    %Transfer back to time domain
%     S_ext = real(ifft(CPLX_array));

    %For each frame, design an AOA beam former detection
    %Display the angle figure for each frame.
%   AngleDisplay_fun(CPLX_array(1:FrameSize/2, :), k, nb_frames);
%     BeamFormer_fun(CPLX_array(1:FrameSize/2, :), k, nb_frames);
%     BeamFormer_fun_1(CPLX_array(1:FrameSize/2, :), k, nb_frames);
%     [FPP]=BeamFormer_fun_2(CPLX_array(1:nbFFT*Duty, :), BW); %<=100Hz pass
to.
    %Note: Just pass the positive frequencies to subroutine
    %Frequency: from 0 to pi-step, half of the nbFFT.
    [FPP]=BeamFormer_fun_5(CPLX_array(1:floor(nbFFT*Duty), :), BW);
    Ext_P = FPP(end, 4); FPP_end = size(FPP,1);


    %Construct the frequency value
    Y_out_half = ones(nbFFT_P,1); Y_out_half(1:FPP_end) = FPP(:,4);
    Y_out_half(FPP_end +1 :end)= Y_out_half(FPP_end +1 :end)*Ext_P;
    Y_out_half = Y_out_half.* B_half;
```

```
    Y_out_full = [Y_out_half; 0; conj(flipud(Y_out_half(2:end)))];
    y_out_frame = fftshift(ifft(Y_out_full));
    y_start = fr_start; y_end = y_start + nbFFT -1;
    if y_end > DataLen_real
        y_end = DataLen_real;
    end;
    frame_len = y_end - y_start +1;
    y_out(y_start:y_end) = y_out(y_start:y_end) + y_out_frame(1:frame_len);

end;
%Delay y_out nbFFT_P
Delay = floor((nbFFT-FrameSize)/2);
y_out = [y_out(Delay+1:end); zeros(Delay,1)]; %Delay

figure(4);
len = length(y_out);t=(0:1:len-1)/samp_freq;
plot(t, y_out); grid on;
xlabel('Time in 1k samples, Fs = 1k Sa/s');
ylabel('Normalized Amplitude');

% figure(10);
% y5_out = abs(y_out);y5_out = y5_out - mean(y5_out);
% y_fft =abs(fftshift(fft(y5_out)));
% w_step = 2/length(y_fft); w = -1:w_step:1-w_step;
% plot(w, y_fft); grid on;

figure(5);
y1_out = abs(y_out);
subplot(2,1,1);
plot(t, y1_out); grid on;
xlabel('Time in 1k samples, Fs = 1k Sa/s');
ylabel('Normalized Amplitude');

subplot(2,1,2);
% y1_out = y1_out-mean(y1_out);
M = 251; f_cut = 1; Fcut = 2*f_cut/Fs;            %Fcut normalized frequency
b = fir1(M, Fcut);
y2_out = filter(b,1,y1_out);
plot(t, y2_out); grid on;
xlabel('Time in 1k samples, Fs = 1k Sa/s');
ylabel('Normalized Amplitude');
```

```
%%%%%%%%%%%%%%%%%%%%%%%%%%%%%%%%%%%%%%%%%%%%%%%%
% Title: Function BeamFormer_fun_5
%
%%%%%%%%%%%%%%%%%%%%%%%%%%%%%%%%%%%%%%%%%%%%%%%%

function [FPP] = BeamFormer_fun_5(x,BW)        %x is Frequency x N matrix
 N = size(x, 2); Freq_size = size(x, 1);
%Manifold vector
K = -1:0.01:1; v = K'; D = [-(N-1)/2:1:(N-1)/2]; v = exp(j*pi*v*D);
Nv = size(v,1);
%v is MxN matrix
% BeamFormer W
Pos = D';

% p = 0;                %constant
% c = p/N + (1-p)*sin(pi/(2*N));
% W = c*(p + (1-p)*cos(pi/N*Pos));            %Nx1 col vector;
W = hann(N);

k0 = -0.55; k1 = 0.55;
vk0 = exp(j*pi*Pos*(k0)); vk1 = exp(j*pi*Pos*(k1));
W_d = W.*(vk0+vk1);                          %N x 1 col vector;

k_0 = [-0.95 -0.05 0 0.05 1 0.95 ]; k_1 = [-0.95 -0.05 0 0.05 1 0.95];
C0 = exp(j*pi*Pos*k_0); C1 = (j*pi)*(diag(Pos)*exp(j*pi*Pos*k_1));
C = [C0 C1];                    %C: Nx M;  M<=N-1;

e = 1e-6;
P1 = C'*C;                      %P1: M x M matrix
P1 = P1 + eye(size(P1))*e;
P2 = inv(P1);
P_c = C*P2*C';

W1 = (eye(N)-P_c')*W_d;


FPP = zeros(Freq_size,4);
for k = 1: Freq_size
    %Find Phase Difference
    Xf = x(k, :).';
    S = Xf* Xf';

    P_s = zeros(Nv,1);
    for m = 1:Nv
        v_s = v(m,:);
        P_s(m) = real(v_s*S*v_s');
    end;
    [Power,Phase_ind] = max(P_s);

    %Find y out for each frequency
    Yf = abs(W_d'*Xf);
```

```
    FPP(k,:) = [(k-1)/Freq_size*BW, sqrt(Power/N), K(Phase_ind), Yf];
end;
```